2016-03-01

Improvements to the Two-Point In Situ Method for Measurement of the Room Constant and Sound Power in Semi-Reverberant Rooms

Zachary R. Jensen
Brigham Young University - Provo

Improvements to the Two-Point In Situ Method for Measurement of the Room Constant and Sound Power in Semi-Reverberant Rooms

Zachary R. Jensen

A thesis submitted to the faculty of
Brigham Young University
in partial fulfillment of the requirements for the degree of

Master of Science

Timothy W. Leishman, Chair
Scott D. Sommerfeldt
Jonathan D. Blotter

Department of Physics and Astronomy

Brigham Young University

March 2016

ABSTRACT

Improvements to the Two-Point In Situ Method for Measurement of the
Room Constant and Sound Power in
Semi-Reverberant Rooms

Zachary R. Jensen
Department of Physics and Astronomy, BYU
Master of Science

The two-point in situ method is a technique for measuring the room constant of a semi-reverberant room and the sound power of a source in that room simultaneously using two measurement positions. Using a reference directivity source, where the directivity factor along any given axis of the source has been measured, one is able to use the Hopkins-Stryker equation to measure both the room constant and the sound power level of another source rather simply. Using both numerical and experimental data, it was found that by using generalized energy density (GED) as a measurement quantity, the results were more accurate than those using squared pressure. The results also improved when one measurement position was near the source and the other measurement position was far from the source. This resulted in strong contributions of both the direct and reverberant fields in each of the measurement positions. Another improvement to the two-point method was the use of a local, spatial average around the measurement position. The assumptions in the Hopkins-Stryker equation rely on this average and it was found that a small local spatial average improved the measurements. However, this improvement was greater for squared pressure than for GED. Several source sound power levels and room constants were measured to show that these measurements are improved by using the suggested techniques.

Keywords: sound power, room constant, generalized energy density, semi-reverberant enclosure

ACKNOWLEDGEMENTS

I would like to acknowledge my appreciation to my advisor, Dr. Tim Leishman, for all of his help and guidance on this project. I am also grateful for the help of my committee, Dr. Scott Sommerfeldt and Dr. Jon Blotter. I also owe my gratitude to the professors in the acoustics research group at BYU for their support, lessons, and mentoring. A special thank you is owed to the student members of the acoustics research group, both past and present, especially Danny Marquez, Travis Hoyt, and Reese Rasband. I appreciate my office mate and good friend, Josh Bodon, for his support and knowledge. Most importantly, I want to thank my wife for her constant love and support.

Table of Contents

List of Figures

List of Tables

Chapter 1

Introduction

Anyone who has enjoyed a musical performance or given an oral presentation has been affected by the absorption of sound in the room. In addition, the sound power of a source is a metric often used in quantifying global sound radiation, developing regulations for machinery, and predicting the effects of noise. Both the room constant (which quantifies sound absorption in a room) and the sound power are often used in acoustical calculations and measurements. This thesis describes a refined method of measuring both the room constants of semi-reverberant rooms and the sound power of sources in a practical, efficient, and accurate way. It also introduces clarifications and improvements to previous approaches to the problem. The method may allow professionals to more easily meet the requirements of complex standards, which currently require ideal rooms such as anechoic and reverberation chambers.

1.1 Previous Work

The steady-state sound field in a semi-reverberant room can be described by the energy balance equation.[1] It can be broken into two components: the direct field and the reverberant

field. The direct field is dominant near the sound source and is typically described by spherical spreading. The reverberant field is that reflected from surfaces in the room. The time and spatially averaged energy density about a point $(r, \theta_0, \phi_0) = (x, y, z)$ in a room is the summation of the direct and reverberant energy density at that point. The governing equation will be referred to as the Hopkins-Stryker equation[2] and is given by

$$\langle w_T(r, \theta_0, \phi_0) \rangle_{t,s} = \frac{\langle \Pi \rangle_t}{c} \left[\frac{\gamma(\theta_0, \phi_0)}{4\pi r^2} + \frac{4}{R} \right], \tag{1.1}$$

where $\langle w_T \rangle_{t,s}$ is the time and local spatially averaged total energy density (TED), $\langle \Pi \rangle_t$ is the time-averaged source sound power, γ is the far-field directivity factor of the source at angles (θ_0, ϕ_0), r is the distance from the acoustic center of the source, c is the speed of sound, and R is the room constant. Here θ_0 represents the polar angle defined by $\theta_0 = \arccos\left(\frac{z}{r}\right)$ and ϕ_0 represents the azimuthal angle defined by $\phi_0 = \arctan\left(\frac{y}{x}\right)$. The TED is the sum of the potential energy density (PED) and kinetic energy density (KED). The first term in the square brackets in Eq. (1.1) is proportional to the direct energy density and the second term is proportional to the reverberant energy density. This equation is the basis for the two-point method that will be described in this thesis.

There are several ways of measuring either the room constant or the sound power of a source utilizing the principles of direct and reverberant fields represented by the Hopkins-Stryker equation.[3] Standards such as ISO 3741 create guidelines for a sound power measurement to assure that the sound field is predominantly reverberant, with negligible direct sound contribution.[4] The sound power of a source may then be measured using only the principles of diffuse or nearly diffuse fields and neglecting the direct field. ISO 3741 requires a nearly ideal reverberation chamber and uses at least six randomly placed microphones (within constraints)

rather than local spatial averaging. The surface area of the room and reverberation times must also be known to solve for the sound power. Other standards such as ISO 3745 are used in a free-field environment such as an anechoic chamber where the reverberant field energy is negligible, leaving only the direct field for the measurement of sound power.[5]

Most practical rooms are neither anechoic nor reverberant enough to neglect the reverberant or direct energy. For these semi-reverberant fields, other methods must be used to measure the room constant and the sound power of the source. These methods rely fundamentally on the Hopkins-Stryker equation with its relationship to the source sound power, directivity factor, and room constant.

The room constant can be estimated directly from the surface area of the boundaries and their average absorption coefficient.[6] For a majority of rooms, both values can be difficult if not impossible to determine accurately. A classroom, for example, may have several desks, bookshelves, and other fixtures that affect surface area and sound absorption of the room. The difficulty of calculating the correct surface area and absorption for a room inherently makes this method inaccurate and impractical to implement. There is a possibility of measuring the absorption in a room using the measured reverberation time. However, this method is similarly limited by the necessity of calculating the correct surface area and volume of a room. It is also impractical in rooms where many averages are required or a quick measurement is essential.

Other methods have been developed to measure or estimate the *in situ* room constant from measurements in the room. The walk away (WA) method, as described by Moreland, involves taking several pressure measurements near the source and several at increasing distances from the source, all along the same axis.[7] The direct field is then estimated from the measurements near the source and the reverberant field is estimated from the measurements

farther from the source. The room constant can be calculated from the difference between these two estimates. Ianniello found the WA method to be similar in accuracy to calculating the room constant using absorption values measured from reverberation time.[8] However, for accurate results, several measurement points (many more than two) and averages were necessary, making this method cumbersome in practice.

The reference sound power (RSP) method described by Wells involves measuring the sound pressure level (SPL) at specified distances in a free-field environment and then moving the source to the room under test and measuring the SPL at the same specified distances.[9] Again, the difference in SPL is used to calculate the room constant. It may be difficult to find a suitable free-field environment for this measurement. It also assumes that the sound power of the source does not change with a change in environment (and the source position in the room), which may not be accurate.[10]

The two-surface method uses the Hopkins-Stryker equation to measure sound power in semi-reverberant rooms by averaging measurements of two hypothetical surfaces that enclose the source at different distances.[10,11] The measurements can also be used to assess the room constant. However, Moreland showed that the resulting room constant is easily affected by measurement inaccuracies.[7] An accurate evaluation may also require a high resolution of measurements on the surface for sufficient accuracy, possibly making the method impractical.

The loss due to distance (LDD) method uses the difference in SPL at two distances from the source, r and $2r$, to calculate the room constant.[12] Findings are similar to the WA method in that many averages and measurement points must be used to determine accurate results. In this method, the directivity factor of the source is only roughly assumed to be 1, 2, 4, or 8, depending upon its position relative to a reflecting surface.

All of the methods described above use squared pressure, which is proportional to PED to measure sound power or the room constant. However, the original Hopkins-Stryker equation was developed using a local spatial average of the TED. The benefit of using TED is that it is more spatially uniform than PED.[13,23] More recently, Xu et al. have shown that generalized energy density (GED), a "weighted" total energy density, has an even lower spatial variance than TED.[14]

Marquez explored a two-point in situ method, which utilizes the enhanced spatial uniformity of the GED to measure the room constant and sound power of a source.[15] This is similar to the LDD method in that it utilizes two measurements along a line at increasing distance from the source. However, a reference directivity source is used, meaning that the directivity factor in a specified direction $\gamma_{ref}(\theta_0, \phi_0)$ is known in advance and is not estimated. The room constant and sound power can then be solved directly from two equations. The method will be described further in Ch. 2.

Using the two-point method, Marquez measured the sound power of a loudspeaker with reasonable accuracy in a few different rooms. However, the room constant results were erratic when compared with expectations. This discrepancy inspired the further research into the two-point method explained in this thesis.

1.2 Motivation for Research

Knowledge of the room constant is essential for the measurement of sound power using the two-point method. Its value can also be used to calculate other room acoustics parameters such as average absorption coefficient, reverberation time, and critical distance. These parameters are invaluable to those interested in noise control and sound system design. An in situ measurement

of the room constant could potentially reduce the time and effort necessary for work in these areas and its validation.

A practical, efficient, and accurate method of measuring the sound power level of a source in a semi-reverberant room would likewise be very useful to anyone involved in designing or evaluating products within noise constraints. An engineer could simply (and with reasonable accuracy) measure the sound power of a source in any room. This would greatly reduce time, effort, and cost when compared to measuring the sound power according to current ISO standards.

A few shortfalls of previous methods will be addressed in this research. One assumption used to derive the Hopkins-Stryker equation, Eq. (1.1), is that a local spatial average of the measurement is taken, which is described by Pierce as "an average over a volume with dimensions substantially larger than a representative acoustic wavelength but substantially smaller than those of the room as a whole."[1] Beranek also mentions moving a microphone "backward and forward" to obtain a sufficient spatial average.[16] However, all of the methods described earlier utilize a point measurement, rather than a spatial average. While this may be simpler, it does not meet the assumed spatial averaging requirements. The local spatial average is explored in this research as a method of increasing the accuracy of the two-point method.

From experimental results, Marquez observed that the best results from the two-point method were achieved when one measurement point was between the source and the critical distance (more direct field energy), and one measurement point was beyond the critical distance (more reverberant field energy).[16] It is advantageous for the engineer to know what the best positions (relative to the source) are for the microphones in the two-point method and if certain points should be avoided. This thesis explores this matter further.

The weighting factor for the GED used by Marquez was $\beta = 0.25$, which produces the most spatially uniform value of GED in a diffuse field.[13] However, for microphone positions closer to the source than the critical distance, the field is predominantly direct, not diffuse. The question is then, what is the optimal value for β? Is there another value besides $\beta = 0.25$ that leads to a more accurate two-point measurement?

Marquez tested the two-point method using three different sources that might be considered nearly ideal in that they were all loudspeakers with well-behaved broadband radiation. As a natural continuation of this research, three less-ideal sources were tested in this work to see if the two-point method would still be effective. These sources, (a blender, a handheld vacuum, and a belt sander) were considered less-ideal because the positions of their acoustic centers were less clear and their radiation patterns and spectra were considered to be less uniform.

1.3 Objectives

The primary objective of the research was to develop careful guidelines for using the two-point method to improve its results. This was accomplished through the following steps:

1. Exploring the benefits of local spatial averages for improved room constant and sound power measurements.
2. Determining the optimal weighting factor for GED as a measurement quantity in the two-point method.
3. Determining the optimal measurement positions relative to the source when using the two-point method.
4. Measuring the sound power of less-ideal sources using the two-point method.

The objective of this thesis is to present the results of the research through theoretical, numerical, and experimental details that demonstrate practical improvements to the two-point method for measurement of the room constant and sound power.

1.4 Plan of Development

The thesis will be organized as follows. First, Chapter 2 will outline and clarify the theoretical development of the two-point in situ method, as well as a near-field correction to the method. Chapter 3 will describe several numerically modeled rooms used to explore the two-point method and develop guidelines for measurements. Chapter 4 describes the results of several experiments wherein the room constant and sound power are measured using the two-point method. Many other pertinent developments are presented in the appendices.

Chapter 2

Theory

2.1 The Hopkins-Stryker Equation

The time-averaged TED at a point in space is the sum of PED and KED components:

$$\langle w_T \rangle_t = \langle w_P \rangle_t + \langle w_K \rangle_t. \tag{2.1}$$

The time-averaged PED is defined as

$$\langle w_P \rangle_t = \frac{\langle p^2 \rangle_t}{2\rho_0 c^2}, \tag{2.2}$$

where $\langle p^2 \rangle_t$ is the time-averaged squared pressure and ρ_0 is the density of the ambient air. The KED is defined as

$$\langle w_K \rangle_t = \frac{\rho_0}{2} \langle |\boldsymbol{u}|^2 \rangle_t, \tag{2.3}$$

where $|\boldsymbol{u}|$ is the vector magnitude of the particle velocity.

Because Eq. (1.1) has been difficult to implement in the past due to the difficulties in measuring TED, certain assumptions have been made to simplify the equation. By assuring the measurement is in the direct far field of the source (Beranek suggests at least 1/3 of a wavelength

from the source)[16] and that the reverberant field is diffuse, one can assume that the time and locally spatially averaged PED $\langle w_P \rangle_{t,s}$ is equal to the time and local spatially averaged KED $\langle w_K \rangle_{t,s}$.[1] The TED can then be written as

$$\langle w_T \rangle_{t,s} = 2\langle w_P \rangle_{t,s} = 2\langle w_K \rangle_{t,s} = \frac{\langle p^2 \rangle_{t,s}}{\rho_0 c^2} \tag{2.4}$$

and Eq. (1.1) may be written in terms of squared pressure:

$$\langle p^2 \rangle_{t,s} = \langle \Pi \rangle_t \rho_0 c \left[\frac{\gamma(\theta_0, \phi_0)}{4\pi r^2} + \frac{4}{R} \right]. \tag{2.5}$$

This equation illustrates the usefulness of the Hopkins-Stryker equation in that one might predict the average sound pressure at a position in a room by knowing the room constant, the source sound power, and its directivity factor. Conversely, one may also measure the sound power of a source by knowing the directivity factor, the room constant, and by measuring the average sound pressure in a room.

When using GED rather than PED, the final equation is slightly different. The GED is calculated as

$$\langle w_{G,\beta} \rangle_t = \beta \langle w_P \rangle_t + (1 - \beta) \langle w_K \rangle_t \,, \tag{2.6}$$

where $\langle w_{G,\beta} \rangle_t$ represents the time-averaged GED and β is the weighting factor. For a truly diffuse field, a weighting factor of $\beta = 0.25$ is optimal for minimum spatial variance.[14,15] The more familiar PED, KED, and TED follow from other β values:

$$\langle w_{G,1} \rangle_t = \langle w_P \rangle_t; \;\; \beta = 1 \tag{2.7a}$$

$$\langle w_{G,0} \rangle_t = \langle w_K \rangle_t; \;\; \beta = 0 \tag{2.7b}$$

$$\langle w_{G,1/2} \rangle_t = \frac{\langle w_T \rangle_t}{2}; \; \beta = \frac{1}{2} \tag{2.7c}$$

Using the simplifying assumption that $\langle w_P \rangle_{t,s} = \langle w_K \rangle_{t,s}$ as described earlier, Eq. (2.6) reduces to $\langle w_{G,\beta} \rangle_{t,s} = \langle w_P \rangle_{t,s} = \langle w_K \rangle_{t,s} = \langle w_T \rangle_{t,s}/2$ for any β. Equation (1.1) may then be expressed in terms of GED as

$$\langle w_{G,\beta} \rangle_{t,s} = \frac{\langle \Pi \rangle_t}{2c} \left[\frac{\gamma(\theta_0, \phi_0)}{4\pi r^2} + \frac{4}{R} \right]. \tag{2.8}$$

Equation (2.8) is the Hopkins-Stryker equation for GED, with the direct and reverberant energy densities

$$\langle w_{G,\beta,D} \rangle_{t,s} = \frac{\langle \Pi \rangle_t}{2c} \frac{\gamma(\theta_0, \phi_0)}{4\pi r^2} \tag{2.9}$$

and

$$\langle w_{G,\beta,R} \rangle_{t,s} = \frac{\langle \Pi \rangle_t}{2c} \frac{4}{R}. \tag{2.10}$$

The critical distance is defined as the distance from the source where the direct [Eq. (2.9)] and reverberant [Eq. (2.10)] field contributions are equal, i.e.,

$$r_c = \sqrt{\frac{\gamma(\theta_0, \phi_0) R}{16\pi}}. \tag{2.11}$$

The general concepts of the Hopkins-Stryker equation and its direct and reverberant-field energy density are illustrated graphically in Fig. 2.1. In this example, the room has a volume of 210 m^3, a surface area of 214 m^2, a room constant of 112 m^2, and a monopole radiating with a sound power of 1 mW. The composite and direct energy density levels are shown relative to the reverberant level as

$$L = 10 \log\left(\langle w_{G,\beta} \rangle_{t,s} / \langle w_{G,\beta,R} \rangle_{t,s} \right) \tag{2.12}$$

and

$$L_D = 10 \log\left(\langle w_{G,\beta,D} \rangle_{t,s} / \langle w_{G,\beta,R} \rangle_{t,s} \right), \tag{2.13}$$

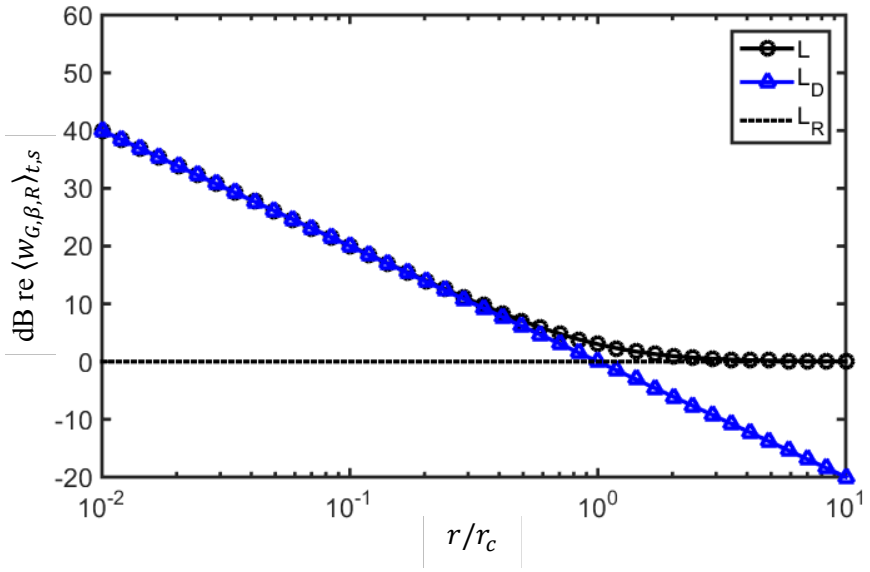

Fig 2.1. The composite-field level L of a monopole by the Hopkins-Stryker equation, the direct-field level L_D, and the reverberant-field level L_R. All levels are relative to $\langle w_{G,\beta,R}\rangle_{t,s}$, which is assumed to be constant over distance. In this example, the room volume is 210 m^3, the surface area is 214 m^2, and the room constant is 112 m^2.

respectively. The reverberant field energy density level is also plotted (L_R), but since it is calculated relative to itself, the value is consistently zero.

The Hopkins-Stryker equation inherently assumes direct far-field and diffuse reverberant-field conditions. The diffuse reverberant field requires that its local spatially averaged energy density be the same at any point. In other words, as the distance from the source increases, the composite locally spatially averaged energy density converges to a constant value, regardless of position in the room. These assumptions can be compromised in actual rooms due to nonuniformly distributed absorption, scattering surfaces, and irregular room geometries.

Room shape and size are well-known factors in the diffuse-field assumption. For example, in a hallway, the directions of plane waves converging on a point are not randomly distributed, but are biased in the direction leading down the hallway (away from the source). Rooms with high absorption, especially nonuniform absorption, also detract from the diffuse-

field criteria. On the other hand, the majority of rooms discussed in this thesis are "Sabine-like," in that they have reasonable aspect ratios where one dimension is not much larger than another.[7] While this constraint does limit application to some rooms, the sound field in many typical rooms may be approximated by the Hopkins-Stryker equation, especially for the types mentioned in this thesis, such as offices, labs, storage rooms, and classrooms.

In certain rooms, a reduction in the reverberant field may be observed as one moves away from the source.[36] This decay has been noticed particularly in large rooms, rooms with high absorption, or rooms with irregular aspect ratios as mentioned previously.[36-39] Several different corrections for this nonuniformity have been developed. Some methods require a measurement of the reverberant-field decay, while others are analytical or empirical. Hodgson provides a summary of some of these methods for large rooms.[39] While it is beyond the scope of this thesis, further research into which correction works best with the two-point method would be beneficial.

2.2 Near-Field Correction

The Hopkins-Stryker equation relies on the assumption that all measurements are made in the direct far field where wavefronts are locally planar and the PED and KED are equal. However, the two energy densities diverge in the near field, even for a monopole source. The KED becomes much larger than the PED and thus the TED becomes larger than twice the PED. The PED of a monopole is given by Pierce as[1]

$$\langle w_P \rangle_t = \frac{\langle I_r \rangle_t}{2c}, \tag{2.14}$$

where $\langle I_r \rangle_t$ is the time-averaged radial intensity. The KED is

$$\langle w_K \rangle_t = \frac{\langle I_r \rangle_t}{2c}\left[1 + \frac{1}{(kr)^2}\right]. \tag{2.15}$$

The TED is then the sum of Eq. (2.14) and (2.15),

$$\langle w_T \rangle_t = \frac{\langle I_r \rangle_t}{2c}\left[2 + \frac{1}{(kr)^2}\right]. \tag{2.16}$$

For a monopole, the Hopkins-Stryker equation can be readily corrected for the near-field effects. The time-averaged intensity is written in terms of its sound power and directivity factor $\gamma(\theta_0, \phi_0) = 1$ as[1]

$$\langle I_r \rangle_t = \langle \Pi \rangle_t \left(\frac{1}{4\pi r^2}\right). \tag{2.17}$$

When substituted into Eq. (2.16), this resembles the direct-field term of the Hopkins-Stryker equation for an omnidirectional source, but with an extra correction term:

$$\langle w_T \rangle_t = \langle \Pi \rangle_t \left(\frac{1}{4\pi r^2 c}\right)\left[1 + \frac{1}{2(kr)^2}\right]. \tag{2.18}$$

In Fig. 2.2, the associated direct-field level relative to the reverberant energy density is overlaid with the levels previously shown in Fig. 2.1. In this case, $\beta = 0.5$ for GED.

In the direct far-field region (beyond about 10% of the critical distance in this example), the corrected and uncorrected levels converge, and the Hopkins-Stryker equation gives the correct composite field value. However, in the near field, the Hopkins-Stryker equation should follow the direct TED field but does not.

For a monopole, the Hopkins-Stryker equation can then be modified to include a near-field correction using Eqs. (2.6)-(2.14) in terms of GED, giving

$$\langle w_{G,\beta,N} \rangle_{t,s} = \frac{\langle \Pi \rangle_t}{2c}\left(\frac{1}{4\pi r^2}\left\{\beta + (1-\beta)\left[1 + \frac{1}{(kr)^2}\right]\right\} + \frac{4}{R}\right). \tag{2.19}$$

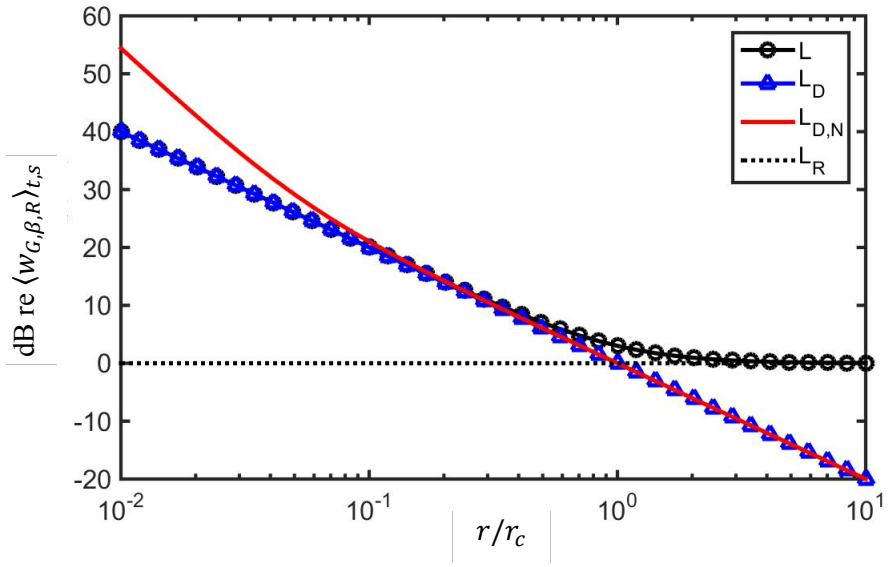

Fig 2.2. The near-field-corrected direct field level $L_{D,N}$ of a monopole overlaid with the levels previously shown in Fig. 2.1 All levels are relative to $\langle w_{G,\beta,R}\rangle_{t,s}$, which is assumed to be constant over distance. In this example, the room volume is 210 m^3, the surface area is 214 m^2, and the room constant is 112 m^2.

A similar, corrected, composite level relative to the reverberant-field level is then

$$L_N = 10\log\left(\langle w_{G,\beta,N}\rangle_{t,s}/\langle w_{G,\beta,R}\rangle_{t,s}\right). \tag{2.20}$$

As shown in Fig. 2.3, this corrected Hopkins-Stryker equation successfully converges to the direct-field GED for a given value of $\beta = 1/2$ when $r < r_c$. While $\beta = 1/2$ was used as an example, it should be noted that Eq. (2.19) will work for any value of β. The benefit of GED is that the value of β may be varied depending upon the application. The optimal value of β for the Hopkins-Stryker equation will be discussed more in Ch. 3, but Eq. (2.19) clearly shows that its near-field term should be adjusted for the value chosen.

When using the two-point method, the positions of the two measurements relative to the source become important, as will also be discussed in Ch. 3. It will be shown that the optimal placement is to have one measurement in the predominantly direct field of the source and the other in the predominantly reverberant field, as suggested by Marquez.[15] Under certain

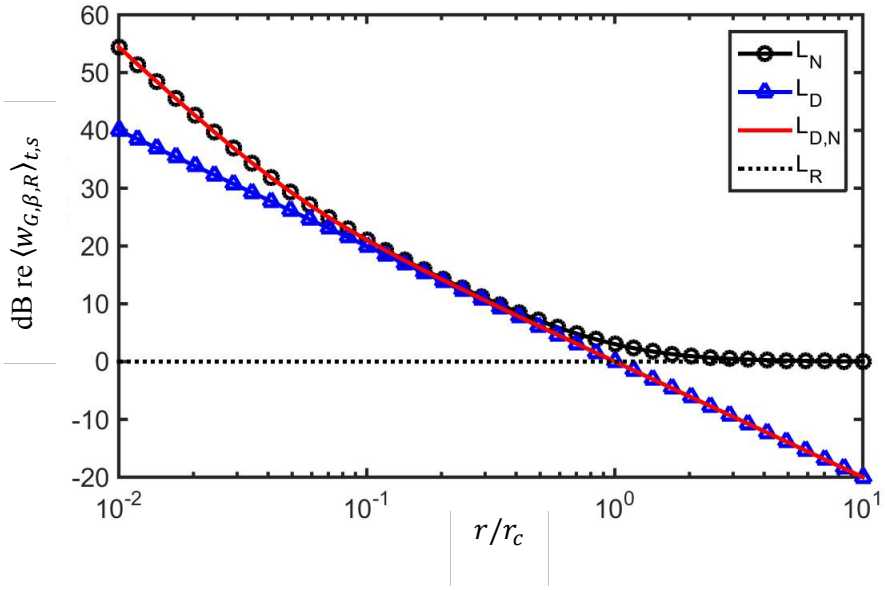

Fig. 2.3. The PED and TED are shown for the same conditions as described for Fig. 2.1. The results of the corrected Hopkins-Stryker equation follow the TED in the near-field as expected.

measurement conditions (especially at low frequencies), the direct far field may be too close to the critical distance or even beyond it, making a measurement in the direct near field necessary to avoid two measurements in the predominantly reverberant field. Equation (2.19) is meant to address the effects of a predominantly direct near-field measurement.

Although most actual sources do not radiate as monopoles, one might use Eq. (2.19) as a starting point for measurements near a source that are not in the direct far field. In principle, the directivity factor for an actual source would be substituted into Eq. (2.19) to make it a more useful equation. Furthermore, a directivity factor $\gamma(k, r, \theta_0, \phi_0)$ that is a function of frequency, distance, and angle would be known. The direct near-field PED and KED for practical sources are inherently functions of frequency, distance, angle, and β. The difference between PED and KED would be known to develop a near-field correction $K(k, r, \beta)$. This would allow one to write the modified Hopkins-Stryker equation in the form

$$\langle w_{G,\beta}\rangle_{t,s} = \frac{\langle \Pi\rangle_t}{2c}\left(\gamma(k,r,\theta_0,\phi_0)K(k,r,\beta) + \frac{4}{R}\right). \tag{2.21}$$

Because the exact natures of $\gamma(r,\theta_0,\phi_0)$ and $K(k,r,\beta)$ are source dependent, they are not well defined. Long gives an example for measurements near a very large source (such as a wall) where r in Eq. (2.8) is replaced with $r + \sqrt{S\gamma/4\pi}$.[36] One could imagine another near-field correction for a cylindrical or a line source which is proportional to $1/r^2$ near the source and $1/r$ in the far-field. These near-field corrections could be derived analytically for other idealized source configurations, but such work is beyond the scope of this thesis.

For the developments presented herein, the near-field correction was approximated for actual sources by simply including the far-field directivity factor in Eq. (2.19):

$$\langle w_{G,\beta}\rangle_{t,s} = \frac{\langle \Pi\rangle_t}{2c}\left(\frac{\gamma(\theta_0,\phi_0)}{4\pi r^2}\left\{\beta + (1-\beta)\left[1 + \frac{1}{(kr)^2}\right]\right\} + \frac{4}{R}\right). \tag{2.22}$$

Although this approximation introduces errors for the reasons mentioned, they are typically limited to low frequencies and cases for which measurements are taken very near to a source.

2.3 The Two-Point Method

The two-point method uses a reference directivity source rather than a reference power source, meaning that the directivity factor $\gamma_{ref}(\theta_0,\phi_0)$ is known and is not estimated. The far-field directivity factor will be used in this derivation because it can be readily measured. Should any dependence upon radial distance be known, it could be simply incorporated. The GED weighting factor β will also be kept general for this derivation. Optimal values of β will be covered further in Ch. 3.

Since the directivity factor of the source is known in advance and two measurement points are used, the room constant and sound power can be solved directly. With two measurement points at positions (r_1, θ_0, ϕ_0) and (r_2, θ_0, ϕ_0) from the source, Eq. (2.22) yields

$$\langle w_{1,G,\beta} \rangle_{t,s} = \frac{\langle \Pi \rangle_{t,ref}}{2c} \left[\frac{\gamma_{ref}(\theta_0, \phi_0)}{4\pi {r_1}^2} K_{1,\beta} + \frac{4}{R} \right] \tag{2.23a}$$

and

$$\langle w_{2,G,\beta} \rangle_{t,s} = \frac{\langle \Pi \rangle_{t,ref}}{2c} \left[\frac{\gamma_{ref}(\theta_0, \phi_0)}{4\pi {r_2}^2} K_{2,\beta} + \frac{4}{R} \right], \tag{2.23b}$$

where

$$K_{i,\beta} = \beta + (1 - \beta) \left[1 + \frac{1}{(kr_i)^2} \right] \tag{2.24}$$

is the near-field correction factor. Again, the correction for a monopole is used in this derivation, but it could be replaced by a more suitable near-field correction for a given source. The room constant is then solved as

$$R = \frac{16\pi \left(\frac{\langle w_{2,G,\beta} \rangle_{t,s}}{\langle w_{1,G,\beta} \rangle_{t,s}} - 1 \right)}{\gamma_{ref}(\theta_0, \phi_0) \left(\frac{K_{2,\beta}}{r_2^2} - \frac{K_{1,\beta}}{r_1^2} \frac{\langle w_{2,G,\beta} \rangle_{t,s}}{\langle w_{1,G,\beta} \rangle_{t,s}} \right)}. \tag{2.25}$$

The reference source is then replaced by the device under test (DUT) and two more measurements are taken:

$$\langle w_{3,G,\beta} \rangle_{t,s} = \frac{\langle \Pi \rangle_{t,DUT}}{2c} \left[\frac{\gamma_{DUT}(\theta_0', \phi_0')}{4\pi {r_3}^2} K_{3,\beta} + \frac{4}{R} \right], \tag{2.26a}$$

and

$$\langle w_{4,G,\beta} \rangle_{t,s} = \frac{\langle \Pi \rangle_{t,DUT}}{2c} \left[\frac{\gamma_{DUT}(\theta_0', \phi_0')}{4\pi {r_4}^2} K_{4,\beta} + \frac{4}{R} \right]. \tag{2.26b}$$

These measurements could be taken at a different angle from the reference source measurements, as indicated by (θ_0', ϕ_0'). The directivity factor of the DUT along the axis is thus measured in situ and solved as

$$\gamma_{DUT}(\theta_0', \phi_0') = \frac{16\pi\left(\frac{\langle w_{4,G,\beta}\rangle_{t,s}}{\langle w_{3,G,\beta}\rangle_{t,s}} - 1\right)}{R\left[\frac{K_{4,\beta}}{r_4^2} - \frac{K_{3,\beta}}{r_3^2}\frac{\langle w_{4,G,\beta}\rangle_{t,s}}{\langle w_{3,G,\beta}\rangle_{t,s}}\right]}. \tag{2.27}$$

The sound power of the DUT can be subsequently solved from either Eq. (2.26a) as

$$\langle \Pi_{DUT}\rangle_t = \frac{2\langle w_{3,G,\beta}\rangle_{t,s} c}{\left(\frac{\gamma_{DUT}(\theta_0', \phi_0')}{4\pi {r_3}^2} K_{3,\beta} + \frac{4}{R}\right)}. \tag{2.28}$$

Equation (2.26b) yields a similar result.

2.4 Room Constant

Throughout the literature, there are several proposed definitions for the room constant.[1,2,16,18-21] It was defined by Hopkins and Stryker as[2]

$$R = \frac{S\bar{\alpha}}{1 - \bar{\alpha}}\ , \tag{2.29}$$

where $\bar{\alpha}$ represents the average absorption coefficient and S is the total surface area of the room boundaries. The average absorption coefficient may be calculated by summing the absorption coefficient, α_i, of each surface element multiplied by its surface area S_i and dividing the sum by S:[6]

$$\bar{\alpha} = \frac{\sum S_i \alpha_i}{S}. \tag{2.30}$$

Beranek[16] and others have alternatively defined the room constant as

$$R = S\bar{\alpha}, \tag{2.31}$$

which is clearly an approximation for small values of $\bar{\alpha}$. However, Pierce[1] states that the approximation is generally used due to "the absence of any better model of comparable simplicity." Wells and Weiner refer to the room constant simply as a function of absorption,

$$R = f(\bar{\alpha}), \tag{2.32}$$

without explicitly defining it.[19] They discussed a method similar to the two-point method wherein the room constant could be measured and the explicit formula was not necessary. Thompson and Cortana modified the room constant to account for local energy density anomalies in rooms with complex shapes, absorption, and scattering surfaces.[20,21] One could also add air absorption when calculating the room constant by adding $4mV$, where m is the air absorption coefficient according to ISO 9613 and V is the total room volume.[6,17]

The benefit of the two-point method is that one can measure the room constant directly, without knowing the explicit formula, as was done by Wells and Weiner. One does not need to be concerned with air absorption as long as the temperature and humidity do not vary significantly during the measurement process. In Chs. 3 and 4, Eqs. (2.29)-(2.31) are used to compare to the measured room constant. This is feasible because the rooms are generally "Sabine-like."

2.5 A Three-point Method

Ideally, it would be very useful if a three-point method could be developed to assess the in-situ sound power, directivity factor, and room constant. This would alleviate the requirement for a reference directivity source. Unfortunately, this is not feasible with the Hopkins-Stryker equation in Eq. (2.22). The issue is that the sound power, directivity factor, and room constant terms are not independent variables. With three equations (three different measurements along the same axis), the result is a nonlinear underdetermined system, meaning an infinite number of

solutions is possible for each quantity. In other words, one can solve for the ratio between two of the three variables, but cannot solve all three simultaneously.

The acoustic center of a source could potentially be determined by using a three-point method and the near-field correction discussed in Sec. 2.2. This is accomplished by making three measurements along one axis from an assumed acoustic center of the source and varying the distance that the measurement probe is moved. For example, the first measurement is taken at a distance r from the assumed acoustic center of the source. Since the exact location of the acoustic center is unknown, the distance r cannot be measured or known, but will be solved for. The second and third measurements are then taken at a distances of Δr and $d\Delta r$ from the first measurement, along the same axis, where d is any positive real number. The equations for these three measurements follow from Eq. (2.22) as

$$\langle w_{1_{G,\beta}}\rangle_{t,s} = \frac{\langle \Pi \rangle_t}{2c}\left(\frac{\gamma(\theta_0,\phi_0)}{4\pi r^2}\left\{\beta + (1-\beta)\left[1+\frac{1}{(kr)^2}\right]\right\} + \frac{4}{R}\right) \tag{2.33a}$$

$$\langle w_{2_{G,\beta}}\rangle_{t,s} = \frac{\langle \Pi \rangle_t}{2c}\left(\frac{\gamma(\theta_0,\phi_0)}{4\pi (r+\Delta r)^2}\left\{\beta + (1-\beta)\left[1+\frac{1}{k^2(r+\Delta r)^2}\right]\right\} + \frac{4}{R}\right) \tag{2.33b}$$

$$\langle w_{3_{G,\beta}}\rangle_{t,s} = \frac{\langle \Pi \rangle_t}{2c}\left(\frac{\gamma(\theta_0,\phi_0)}{4\pi (r+d\Delta r)^2}\left\{\beta + (1-\beta)\left[1+\frac{1}{k^2(r+d\Delta r)^2}\right]\right\} + \frac{4}{R}\right). \tag{2.33c}$$

The three unknowns ($\langle \Pi \rangle_t$, r, and R) can be solved simultaneously, with a known $\gamma(\theta_0,\phi_0)$, Δr, and d. The solution is quite complicated and involves a fourth order polynomial, but there is an analytical solution that allows the actual distance to the acoustic center from all three measurements to be solved for. The caveat is that the axis for all three point measurements must actually extend through the acoustic center. If this assumption is incorrect, the method will not accurately solve for r. This three-point method of solving for the distance to the acoustic center will not be explored further in this thesis, but could be useful when measuring complex sources.

2.6 Conclusions

The underlying assumptions of the Hopkins-Stryker equation require that measurements be taken in the direct far field of a source, where PED and KED are equal. This may not be feasible for the two-point method in some rooms, when the need for one point inside the critical distance may require a measurement in the direct near-field of the source. A near-field correction to the Hopkins-Stryker equation was developed for a monopole. While it is imperfect for other sources due to near-field differences, the modification was used to enhance the two-point method, allowing one to solve for the room constant and the sound power of a source in terms of the GED weighting factor β. Numerical and experimental results will be presented in Chs. 3 and 4 to demonstrate the improvements this enables. A three-point method was outlined that could be used to solved for the distance to the acoustic center of a source. Although it was not explored further, it may be useful in future research for complex or large sources.

Chapter 3

Numerical Results

3.1 Hybrid Modal Analysis

Numerical simulations of sound fields in rooms were used to facilitate the exploration of an improved two-point method. The first was based on the hybrid modified modal analysis model described by Xu and Sommerfeldt.[22] Two aspects of this approach differ significantly from what might be termed classical modal analysis. First, the impedance boundary condition used to solve for the eigenvalues and eigenfunctions is not assumed to be infinite. Instead, the boundary condition is assumed to be the real part of the wall admittance. While not an exact representation of the problem, it has several benefits. First and foremost, it allows more rooms with damping to be modeled than with classical modal analysis. This point was considered extremely beneficial for modeling the semi-reverberant rooms of this study, many of which involved considerable damping. In these cases, the eigenvalue problems were solved numerically.

By using only the real part of the boundary admittance, the numerical root search for the eigenvalue is not in the complex domain, which makes it more computationally efficient. The

second aspect which differs from classical modal analysis is that the free-field Green's function of a point source is included as part of the solution. In this case, the model converges much more quickly near the point source, where it would otherwise be very slow. The full development of the method can be found in Appendix A. One of the challenges of the approach is that it requires an admittance value for the boundaries rather than an absorption coefficient. Appendix B provides details on assigning impedance values for a given absorption coefficient and validation of the approach for an actual room.

3.2 Design of Experiments

3.2.1 Room Characteristics

A numerical design of experiments (DOE) was developed to more fully explore and generalize the guidelines learned from the numerical models. The sound fields of nine different rooms were modeled using either a single point source or multiple point sources. The pressure and particle velocity were calculated using the hybrid modified modal analysis (HMMA) method described in Appendix A. The models were all based on actual rooms so the method might be usefully compared. As described in Table 3.1, the nine rooms comprised several different combinations of room dimensions (L_x, L_y, L_z) and average absorption coefficients $\bar{\alpha}$. The volume V, surface area S, source position (x_0, y_0, z_0), Schroeder frequency[1] f_s, and critical distance r_c of each room are also shown in the table. The absorption coefficients used in the models were frequency dependent, measured in 1/3 octave bands. However, Table 3.1 shows the frequency-averaged absorption coefficients $\bar{\alpha}$ for simplicity. The absorption coefficients were applied uniformly to every surface in each room model.

Table 3.1. The characteristics of each of the rooms in the design of experiments.

Room	V	S	$\bar{\alpha}$	f_s	r_c	(x_0, y_0, z_0)	(L_x, L_y, L_z)
1	27	54	0.02	730	0.2	(0.92, 1.82, 1.08)	(3.59,2.89,2.58)
2	27	54	0.20	258	0.5	(0.92, 1.82, 1.08)	(3.59,2.89,2.58)
3	61	99	0.04	418	0.3	(1.75, 1.55, 1.00)	(5.68,4.29,2.51)
4	61	99	0.45	127	1.3	(1.75, 1.55, 1.00)	(5.68,4.29,2.51)
5	205	210	0.02	368	0.3	(1.55, 2.05, 1.50)	(4.98,5.88,6.99)
6	205	210	0.19	135	0.9	(1.55, 2.05, 1.50)	(4.98,5.88,6.99)
7	205	210	0.20	130	1.0	(1.55, 2.05, 1.50)	(4.98,5.88,6.99)
8	252	241	0.45	81	2.0	(2.40, 1.60, 1.50)	(7.30,5.40,6.40)
9	532	476	0.19	90	1.4	(1.90, 2.70, 1.00)	(9.60,15.40,3.60)

The first room is modeled after the variable acoustics chamber (VAC) at Brigham Young University (BYU), with its measured absorption, while the second room has the dimensions of the VAC but the average absorption coefficient of a classroom on campus. The third room models the small reverberation chamber at BYU, while the fourth has the dimensions of the chamber but the average absorption coefficients of an industrial test cell for internal combustion engines. The fifth, sixth and seventh rooms all have the dimensions of the large reverberation chamber at BYU with the average absorption coefficients of the chamber, a dance studio, and a small classroom, respectively. The eighth room represents an industrial test cell with its measured absorption coefficients. The ninth room represents the dance studio with its measured absorption coefficients. The rooms increase in room number from the smallest to largest volumes. The room constant increases roughly the same way, although not exactly due to absorption coefficient variations. The different room constants for each room are shown in Fig. 3.1 as functions of frequency.

The room constants are calculated from the spatially averaged absorption coefficient as shown in Eqs. (2.29) and (2.30). For actual rooms, there is almost always significant uncertainty in the room constant due to limitations of calculating the average absorption coefficient. This is caused by errors in reverberation time, room volume, and room surface area estimations.

However, with numerically modeled rooms, the absorption, volume, and surface area have all been well defined, and there are no obstructions or scattering objects that would complicate the room constant calculations. This gives us the benefit of comparing the room constant estimated numerically using the two-point method and that defined by Hopkins and Stryker in Eq. (2.29).[2]

As evident from Fig. 3.1(a), the room constants have a large spread due to the various sizes and absorption coefficients of the different rooms. Fig. 3.1(b) shows a logarithmic version of the room constants given by

$$L_R = 10 \log\left(\frac{R}{1\ \mathrm{m}^2}\right). \tag{3.1}$$

In the past, it has been noted that seemingly large errors in the room constant derived from the two-point method do not create similarly large errors in sound power levels. This is partly due to the logarithmic nature of the sound power level. The sound power level L_Π from the Hopkins-

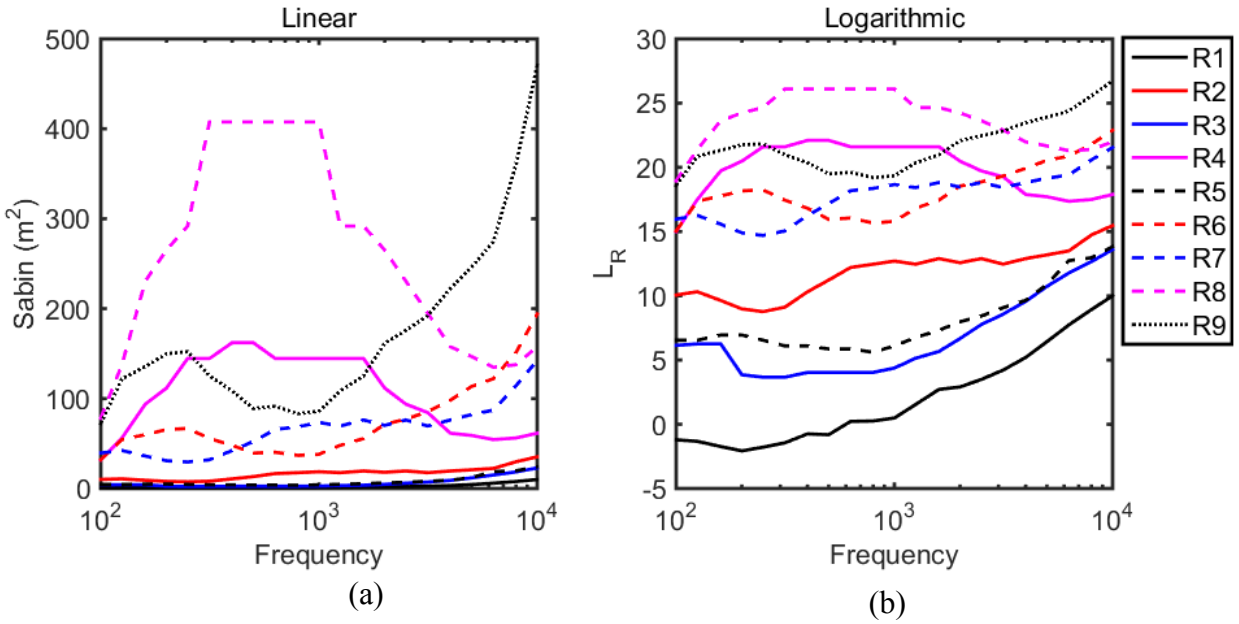

Fig. 3.1. The frequency-dependent room constants of the various rooms in the DOE. Both (a) the linear room constant and (b) the logarithmic room constant L_R are plotted. See Table 3.1 for specific room details.

Stryker equation is composed of direct and reverberant sound contributions, as previously mentioned, and has the following simplified proportionality (on a decibel scale):

$$L_{\Pi} \propto 10 \log\left(\frac{\gamma}{4\pi r^2} + \frac{4}{R}\right). \tag{3.2}$$

Assuming that the measurement position is in the reverberant field so the direct field can be neglected, then the sound power becomes inversely proportional to the room constant:

$$L_{\Pi} \propto 10 \log\left(\frac{4}{R}\right). \tag{3.3}$$

This gives us some context to understand how the linear room constant affects the logarithmic sound power level. From Eq. (3.3), we see that the larger a room constant is, the less contribution the reverberant field produces. A large room constant follows from a room with high absorption, a large surface area, or both. When a room has a large room constant, the diffuse-field assumption behind the Hopkins-Stryker equation begins to break down, meaning one sees greater errors. However, the sound power level may still be measured with reasonable accuracy, due to the fact that the reverberant field contribution with a large room constant is much smaller than the direct field contribution.

3.2.2 Local Spatial Averaging

For each measurement position, a distance to the acoustic center of the source and a directivity factor is defined. When performing a spatial average about that measurement position, the energy density at different distances and angles is measured and averaged. Points in a spatial average have either a different directivity factor or a different distance from the source than the center point of the average. These differences can lead to errors, which is why it is beneficial to know what type of local spatial averaging gives the best results.

Several types of spatial averaging were tested, as depicted in Fig. 3.2. The first was a simple point measurement, which is what has been previously used for the two-point method. The second was a linear spatial average of several discrete points along the axis of measurement, toward and away from the source. The directivity factor at that angle should remain consistent (provided the measurement is in the direct far field) for the entire spatial average. On the other hand, a clear error with this method is caused by underestimation or overestimation of the distance to the source. The third averaging method also involved a linear discrete point traverse, which was perpendicular to the axis of measurement. In this case, both the distance and the directivity factor changed along the traverse, which led to errors. An underestimation of distance is typical for several points of the average. However, it may be assumed that for small averaging lengths, the error due to this underestimation is smaller than that of the parallel linear spatial

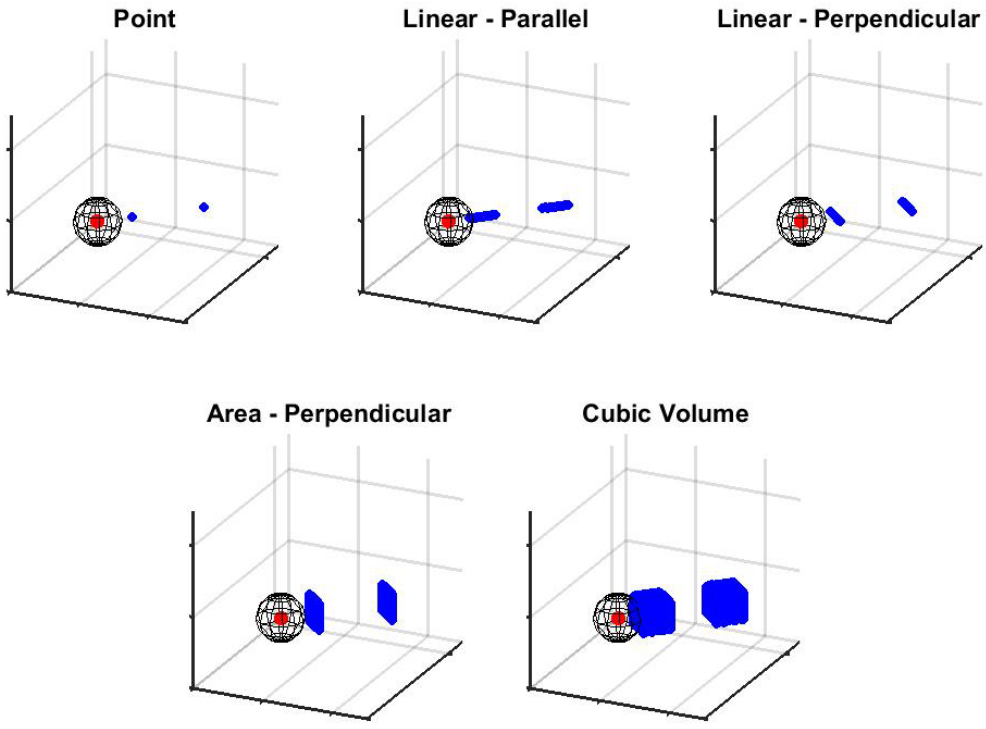

Fig. 3.2. Different methods of spatial averaging that were evaluated numerically. The spherical mesh around the source represents the critical distance for an omnidirectional source. The methods are: (a) a point measurement, (b) a linear average, parallel to the axis of measurement, (c) a linear average, perpendicular to the axis of measurement, (d) an area average, perpendicular to the axis of measurement, and (e) a cubic volume average.

average. The fourth averaging method involved an averaging area perpendicular to the measurement axis, similar to the previous method, but with more points above and below the measurement axis. The fifth method involved a cubic volume around each measurement point, which includes both the advantages and disadvantages of each previous method.

3.2.3 Source Power

The acoustic fields were modeled using HMMA, by simulating a point source in each enclosed room with uniform absorption coefficients. For a monopole in free space, the sound power is calculated as[1]

$$\langle \Pi_M \rangle_t = \frac{\rho_0 c k^2}{8\pi} \left| \hat{Q}_s \right|^2, \tag{3.4}$$

where ρ_0 is the ambient density of air, c is the speed of sound, k is the acoustic wavenumber, and $\hat{Q}_s$ is the complex source strength. The sound power level of the source is calculated as

$$L_{\Pi,M} = 10 \log \left(\frac{\langle \Pi_M \rangle_t}{1 \times 10^{-12}\ \mathrm{W}} \right). \tag{3.5}$$

This can be compared to the sound power levels derived from the HMMA models using the two-point method. The source strength was calculated such that it would output the same power (0.08 W) and sound power level (109 dB PWL) at all frequencies. The density of air was $\rho_0 = 1.21$ and the speed of sound was $c = 343$ for all simulations.

3.2.4 Directivities

In addition to multiple rooms, three different directivities were tested, including those of a monopole, a dipole, and a cardioid source. The dipole was modeled by summing the enclosed complex pressure and particle velocity fields of two closely spaced point sources with a 180° phase difference. The cardioid source was modeled similarly, but using three closely spaced

point sources. Two sources were placed on opposing sides of the center source in the x and $-x$ directions, with opposing polarities. The source was essentially a dipole with a monopole in the center. The source strength required for the cardioid pattern is given by

$$\hat{Q}_{s,1} = \frac{\hat{Q}_{s,0}}{jk_0 d}, \tag{3.6}$$

where $\hat{Q}_{s,0}$ is the source strength of the center monopole, $\hat{Q}_{s,1}$ is the source strength of the two outer point sources (one with an opposite polarity), k_0 is the design wave number for the cardioid pattern, and d is the spacing between the outer sources.

The spacing between the two point sources for the dipole and the outer point sources for the cardioid was $d = 40$ mm. The source strength $\hat{Q}_{s,0}$ was the corresponding source strength to ensure a free-space sound power level of 109 dB PWL as described previously.

The sound power and directivity factor of each source configuration was determined by simulating its free-field pressure response at a distance of 2 m from its center and at 1° increments around a sphere. With these simulations, ISO 3745 could be used to assess the sound powers and directivity factors of the sources as described in Appendix C. Figure 3.3 shows the directivity factors of the dipole and cardioid source configurations at 2 m from the source. The x-y plane of the sound field of all three source configurations for a single frequency is shown in Fig. 3.4, along with a simple diagram of how the sources were positioned (not to scale).

As pointed out earlier, the directivity factor for a source is actually radially dependent in the near-field. Figure 3.5 shows the directivity factor for the cardioid source configuration using a simulated response at six different radii from the center of the source, beginning with 10 centimeters and ending with 10 meters. As the radius of measurement increases, the directivity factor begins to converge to that of the far field. This shows that some error is introduced when

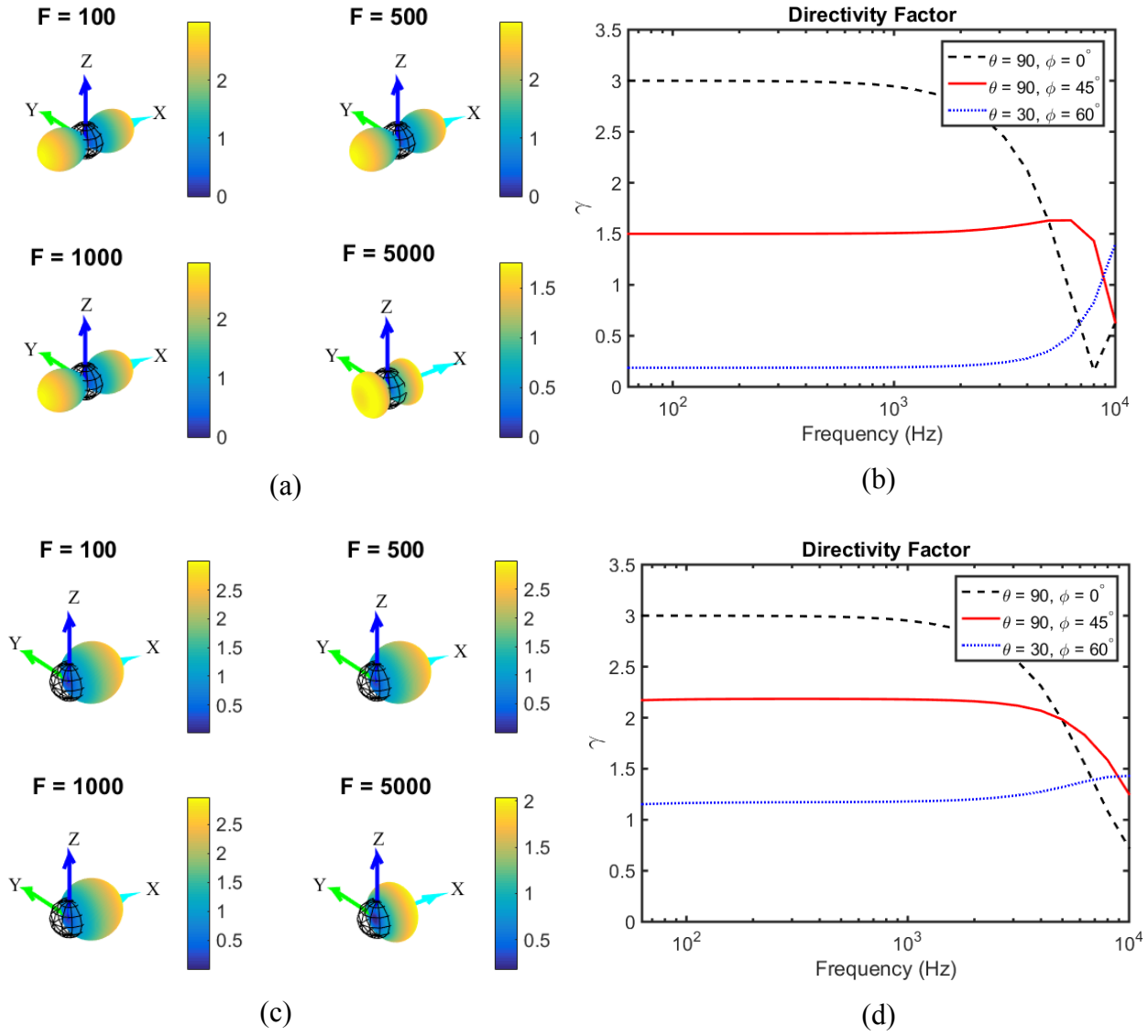

Fig. 3.3. The directivity factor of the dipole source at (a) specific frequencies and (b) specific angles. The directivity factor of the cardioid source at (c) specific frequencies and (d) specific angles. The dipole sources were spaced 40 mm apart. The cardioid is the same configuration as the dipole, with a monopole in the center.

using the two-point method and taking a measurement in the near field, without accounting for the radial dependence of the directivity factor.

However, in practice it is difficult to measure the radially dependent directivity of a physical source. Because of this, the far-field directivity factor of the reference directivity source was measured and used in this thesis to approximate the directivity at all distances from the

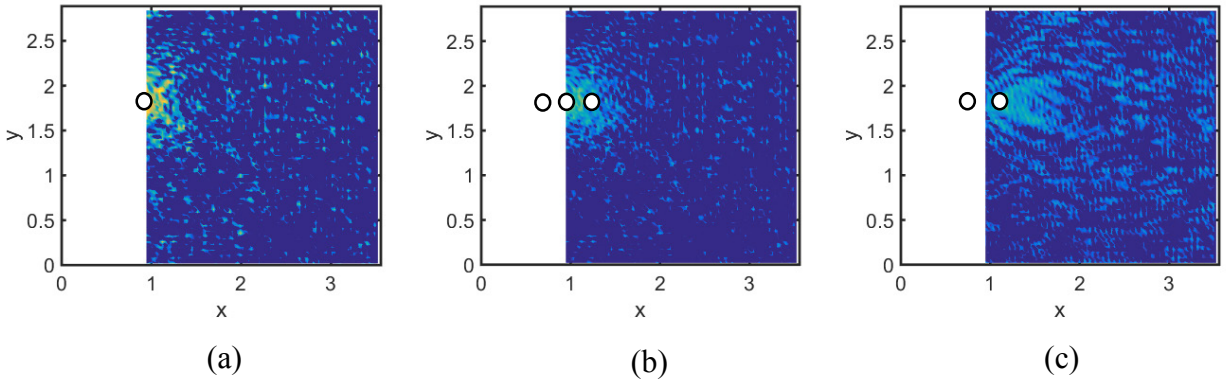

Fig. 3.4. The x-y plane of the sound field in room 2 at the height of the source. The (a) monopole, (b) cardioid, and (c) dipole source directivities can be seen near the source at the left edge the sound field. The sound field was not generated for positions behind the source for computational efficiency.

source. Future research could explore the benefits of using a known near-field directivity factor for sound power and room constant measurements.

3.2.5 Numerical Convergence

In theory, modal analysis requires the summation of an infinite number of modes to calculate the pressure and particle velocity at a point in space. However, as pointed out in

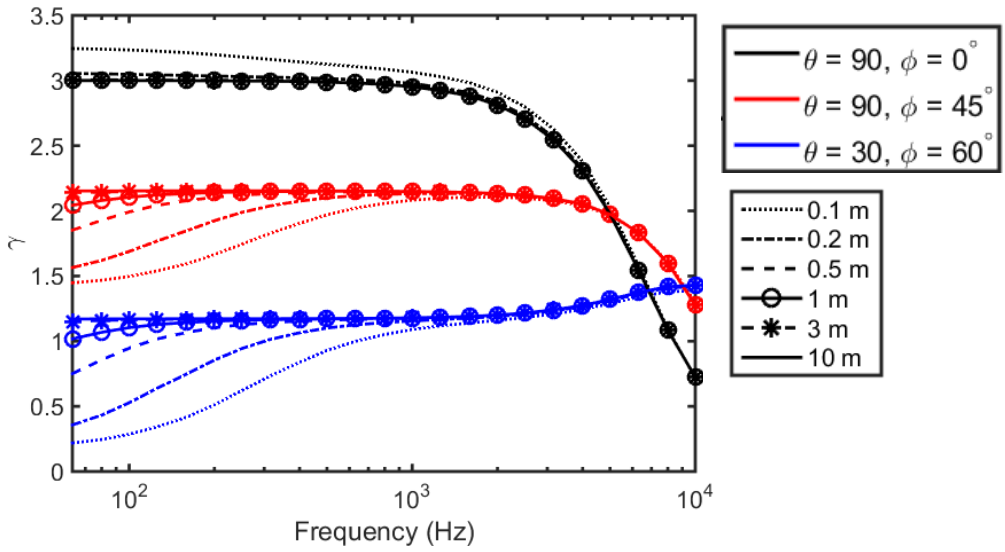

Fig. 3.5. The directivity factor at three different angles for the cardioid source measured at six different radii (0.1, 0.2, 0.5, 1, 3, and 10 meters). As the distance from the center increases, the directivity factor converges to the far-field directivity.

Appendix A, the modal summation must be cut off at a finite number of modes in practice. This is done by using the modal width factor and summing over a number of modal widths.[23] To determine the number of modal widths required for adequate convergence, the pressure values at 30 random points were calculated in the nine rooms used in the DOE. Figure 3.6 shows the difference in the energetically averaged sound pressure level relative to the case using 120 modal widths for all thirty points as a function of the number of modal widths used. It was determined from the convergence trends that a factor of 100 modal widths would be computationally efficient, while still ensuring that the models had converged within a reasonable tolerance of 0.1 dB.

3.2.6 Two-Point Method Example

The DOE was used to generate many different measurements and obtain an average error from the results over several different rooms. For all of the numerical simulations, the frequencies simulated were 1/48 octave bands from 80 Hz to either 5 or 8 kHz, depending on the

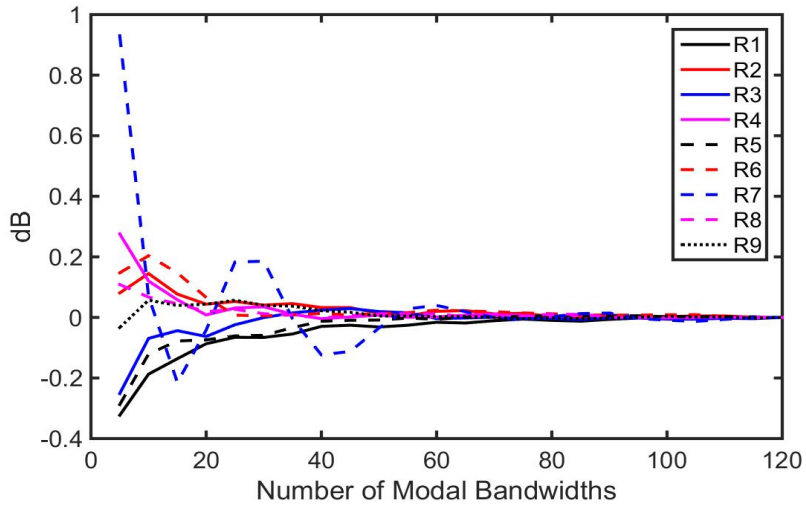

Fig. 3.6. The average sound pressure level relative to a final value with 120 modal bandwidths for all nine rooms used in the DOE.

size of the room. The frequencies were then summed into 1/3 octave bands, meaning 16 narrower bands were summed per 1/3 octave band.

The simulated two-point measurements represented by Figs. 3.7, 3.8, and 3.9 were generated for room 6 with a monopole source. Figure 3.7(a) shows the source (large red dot) in the enclosure (represented by the trihedral corner) and the critical distance (represented by the spherical mesh), along with the two measurement positions (small blue dots). The two measurement positions were at 0.8 m and 3 m from the source, along the axis defined by $\theta_0 = 90°$ and $\phi_0 = 30°$. For reference, $\theta_0 = 90°$ and $\phi_0 = 0°$ is parallel to the *x*-axis and $\theta_0 = 90°$ and $\phi_0 = 90°$ is parallel to the *y*-axis. Figure 3.7(b) shows the free-space sound power level of the monopole, and the sound power level $L_{\Pi,\beta}$ measured by the two-point method [Eq. (2.28)] using both $\beta = 1$ (PED) and $\beta = 0.25$ for the measurement quantities. The room constant is also shown in Fig. 3.7(c) as calculated by Eqs. (2.29), (2.31), and (2.25). The latter is the in-situ room constant measured with the two point method. Figure 3.8 shows the same simulation, but rather than using point measurements, it used a perpendicular linear average. In this case, better agreement is seen between the theoretical values and the simulated measurement values. Figure 3.9 again represents the same simulation, but with a perpendicular area average, which shows even closer agreement between the theoretical and measured values.

3.3 Design of Experiment Results

In order to explore and develop guidelines for the two-point method, 1,000 two-point measurements were simulated in each of the modeled rooms for each source configuration. The simulated measurements were randomly generated for different angles, with different distances from the source and different spatial averaging shapes and sizes. Using a sample size this large, it was possible to generalize some of the findings from the research. Three distinct guidelines

for using the two-point method were explored using the models. The first was the optimal value for the GED weighting factor. The second was the best place for the two-point measurement positions relative to the critical distance. The third was how spatial averaging is beneficial to the two-point method.

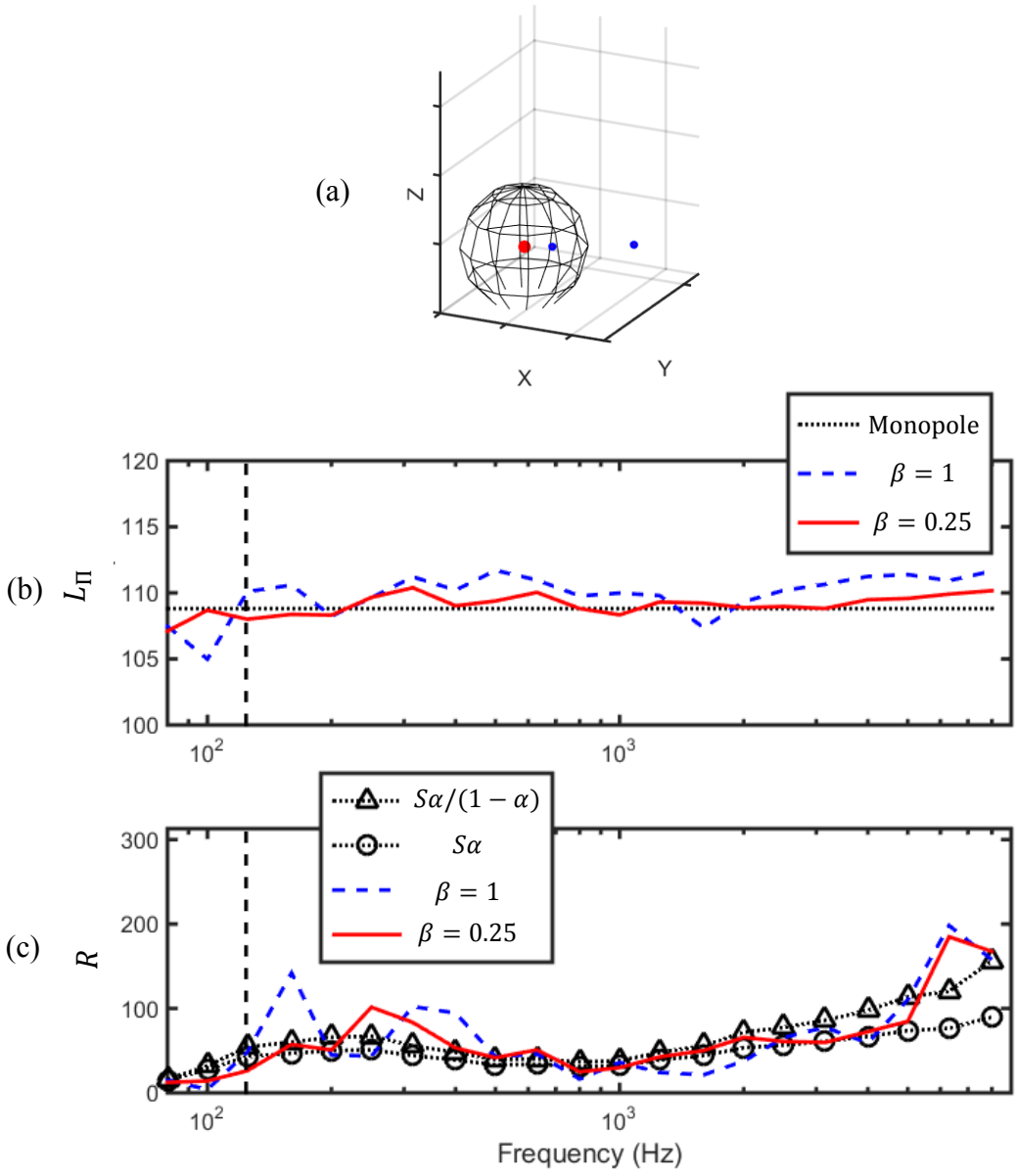

Fig. 3.7. The two-point in situ method simulated in room 6. (a) Two point measurements were used to measure (b) the sound power of the source and (c) the room constant using the two-point method. The spherical mesh around the source represents the critical distance at $r_c = 0.9$ m for an omnidirectional source. The dashed vertical line represents the Schroeder frequency $f_s = 135$ Hz in the room.

To evaluate the effectiveness of the method, the root-mean-square error (RMSE) was assessed over frequency between the actual sound power and the in-situ sound power on a decibel scale. This was similar to the standard deviation calculation used by Marquez and the ISO 3741/ISO 3745.[4-5,15] Specifically, the RMSE calculation for sound power is

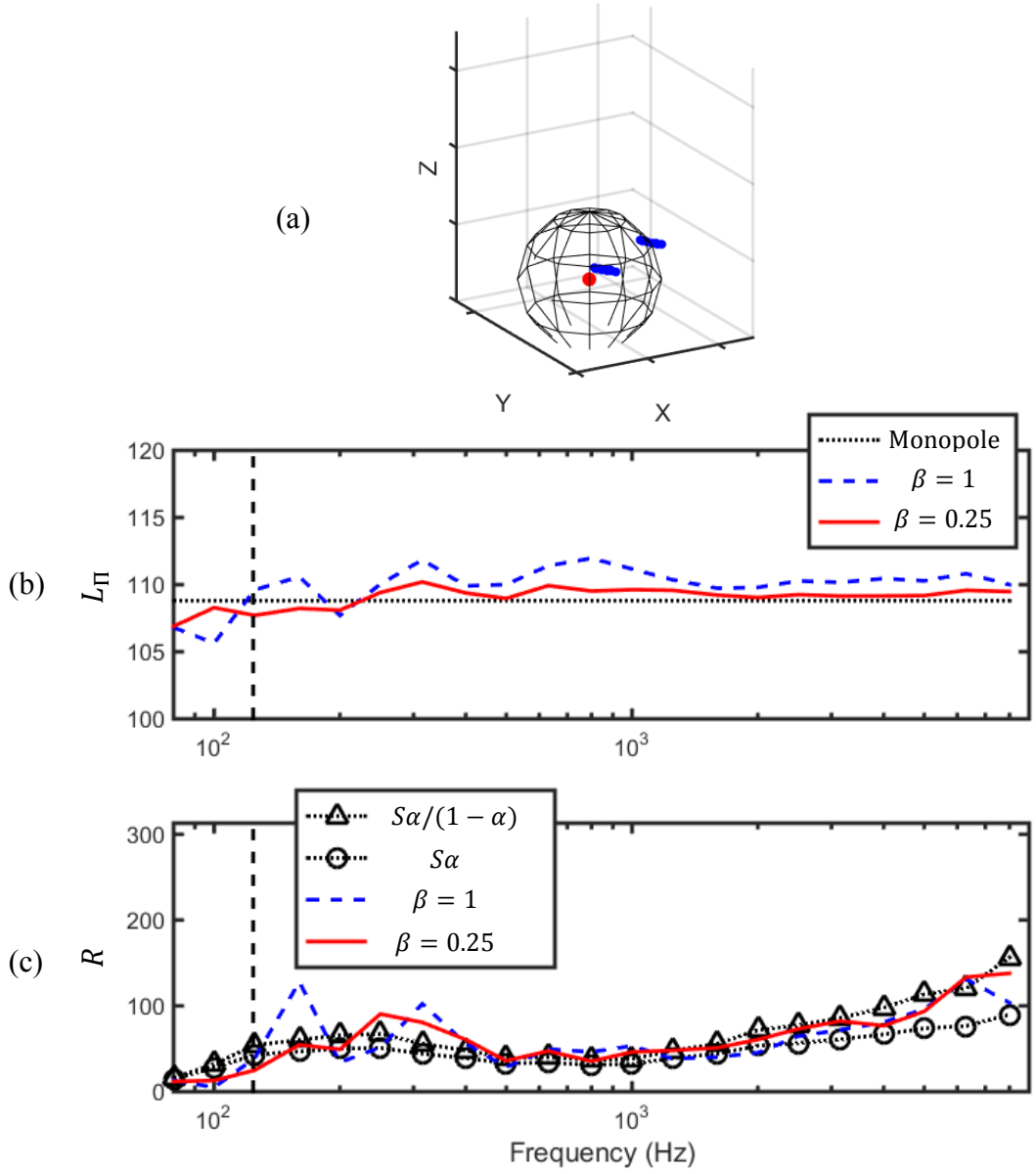

Fig. 3.8. A modified two-point in situ method simulated in room 6. (a) Perpendicular linear spatial averages were used to measure (b) the sound power of the source and (c) the room constant. The spherical mesh around the source represents the critical distance at $r_c = 0.9$ m for an omnidirectional source. The dashed vertical line represents the Schroeder frequency $f_s = 135$ Hz in the room.

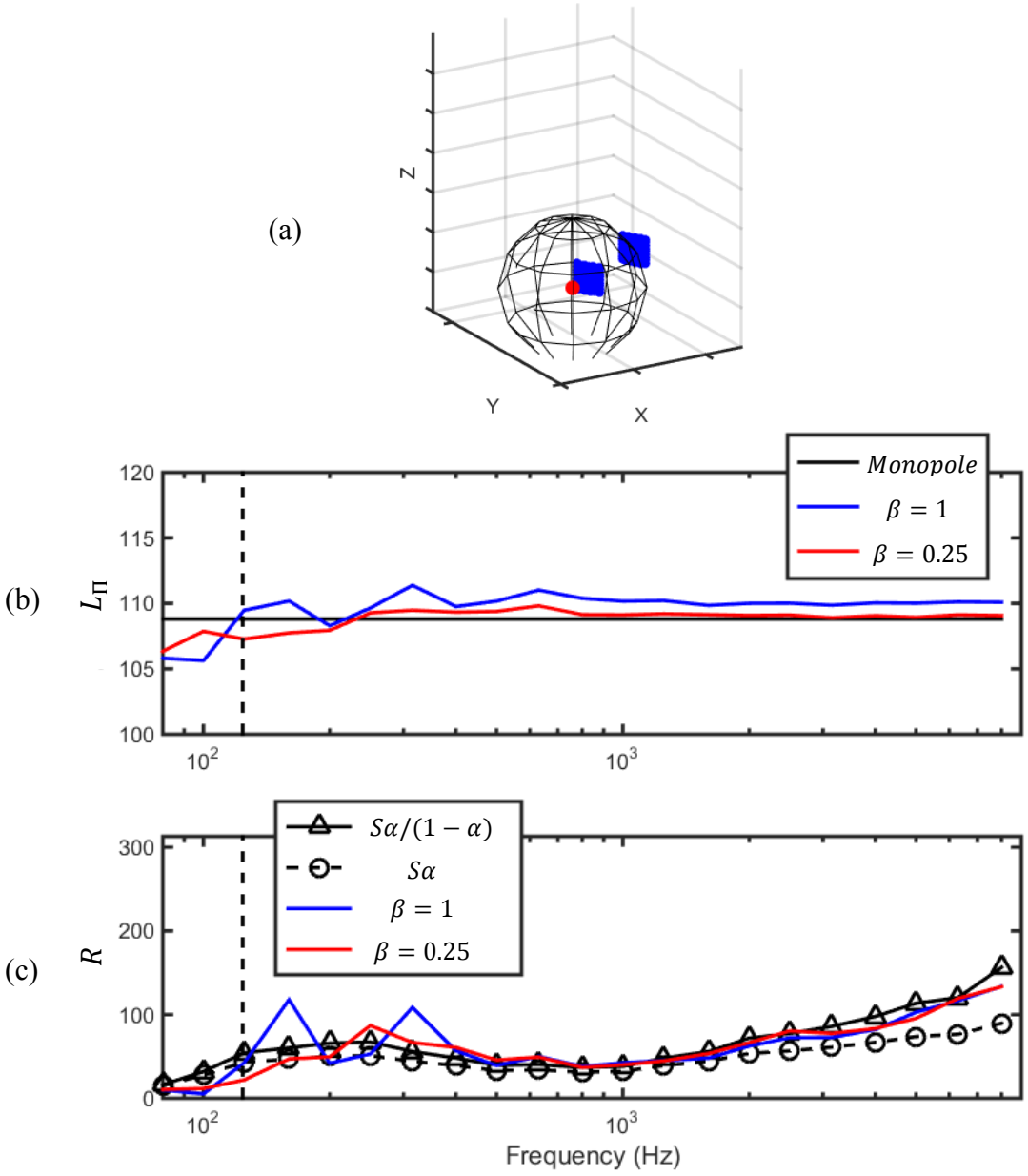

Fig. 3.9. A modified two-point in situ method simulated in room 6. (a) Perpendicular area spatial averages was used to measure (b) the sound power of the source and (c) the room constant. The spherical mesh around the source represents the critical distance at $r_c = 0.9$ m for an omnidirectional source. The dashed vertical line represents the Schroeder frequency $f_s = 135$ Hz in the room.

$$RMSE_{L_\Pi} = \sqrt{\frac{\sum_{i=1}^{N}\left(L_{\Pi_i} - \tilde{L}_{\Pi_i}\right)^2}{N}}, \tag{3.7}$$

where N is the total number of frequencies, L_{Π_i} is the actual sound power level at the i^{th} frequency, and $\tilde{L}_{\Pi_i}$ is the corresponding sound power level determined by the two-point method. Likewise, the RMSE of the room constant was calculated using

$$RMSE_R = \sqrt{\frac{\sum_{i=1}^{N}\left(R_i - \tilde{R}_i\right)^2}{N}}, \tag{3.8}$$

where R is the classical room constant defined by Hopkins and Stryker[2], and $\tilde{R}$ is the measured room constant using the two-point method. The logarithmic RMSE for the room constant

$$RMSE_{L_R} = \sqrt{\frac{\sum_{i=1}^{N}\left(L_{R,i} - \tilde{L}_{R,i}\right)^2}{N}} \tag{3.9}$$

will be used as an additional metric, where L_R is defined by Eq. (3.1) and $\tilde{L}_R$ is the corresponding logarithmic room constant determined using the two-point method.

These error metrics give an idea of how well the measured values match the actual values over frequency and will be used throughout the remainder of this thesis. As indicated earlier, the vertical dashed lines in Figs. 3.7 through 3.9 represent the Schroeder frequency. Below that frequency the diffuse field assumption inherent in the Hopkins-Stryker equation breaks down. Therefore, results from frequencies below the Schroeder frequency are not included in the RMSE calculations.

3.3.1 Optimal Beta

According to Xu et al., the most spatially uniform GED weighting factor is $\beta = 0.25$ for a diffuse field (assumed in the Hopkins-Stryker equation).[14] The question of the optimal weighting factor is raised due to the fact that the two-point method generally uses a point in the

predominantly direct field region and a point in the predominantly reverberant field region. From Fig. 2.3, it can be seen that for the ideal room, the reverberant field contribution in Eq. (2.8) is the same for all values of β. The direct far field, as pointed out previously, is also the same value for all values of β. However, the direct near field, as seen in Eq. (2.19), is dependent upon β. Without the correction for the difference in energy contributions in the direct near field, one might expect that the optimal β value would be closer to $\beta = 1$, since the direct near-field and far-field energy densities are equal for PED.

For each simulation in each room, the optimal β values were found for each measurement axis and frequency, using the MATLAB™ *fmincon* function and the *sqp* algorithm. The cost functions for the optimization were the RMSEs of the logarithmic room constant and sound power level [Eqs. (3.7) and (3.9)]. The process changed the β value from each two-point measurement simulation until the RMSE was minimized. The β values at the first position (β_1) and second position (β_2) in the two-point method were both optimized. Average β values from all optimizations without the near-field correction are shown in Fig. 3.10. As expected, the average value for β increased as frequency decreased (i.e., when r_1 and r_2 were in the direct near field). This follows because the formula without the near-field correction does not account for the increase in KED in the near field, thus causing the RMSE to be higher.

For the case with the near-field correction [see Eq. (2.19)] shown in Fig. 3.11, the optimal β value for nearly every frequency more closely approaches $\beta = 0.25$ for both the sound power and the room constant. With the near-field correction, one can simply use the single value of $\beta = 0.25$ for all frequencies.

Figure 3.12 shows the average of all runs as a function of frequency. Again, variance at low frequencies is present due to the Schroeder frequencies of some of the rooms being higher.

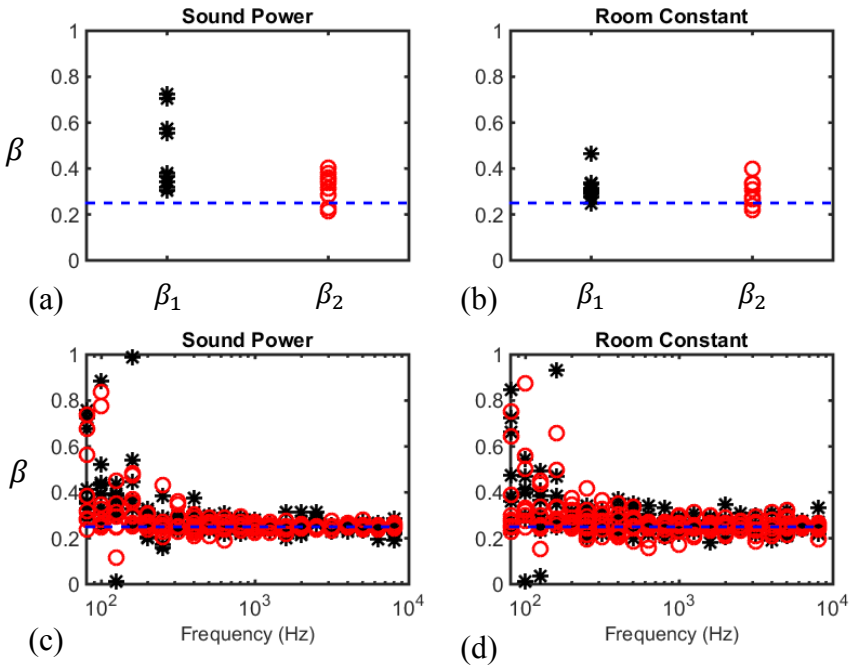

Fig. 3.10. The average GED weighting factors β_1 and β_2 for measurement positions r_1 and r_2 for (a) sound power level and (b) the room constant, optimized over the nine different rooms. It is assumed here that the same β value is used for every frequency. For (c) and (d) the β value varied by frequency for both r_1 and r_2 respectively. The near-field correction was not used for this optimization [see Eq. (2.8)]. The dashed line represents $\beta = 0.25$.

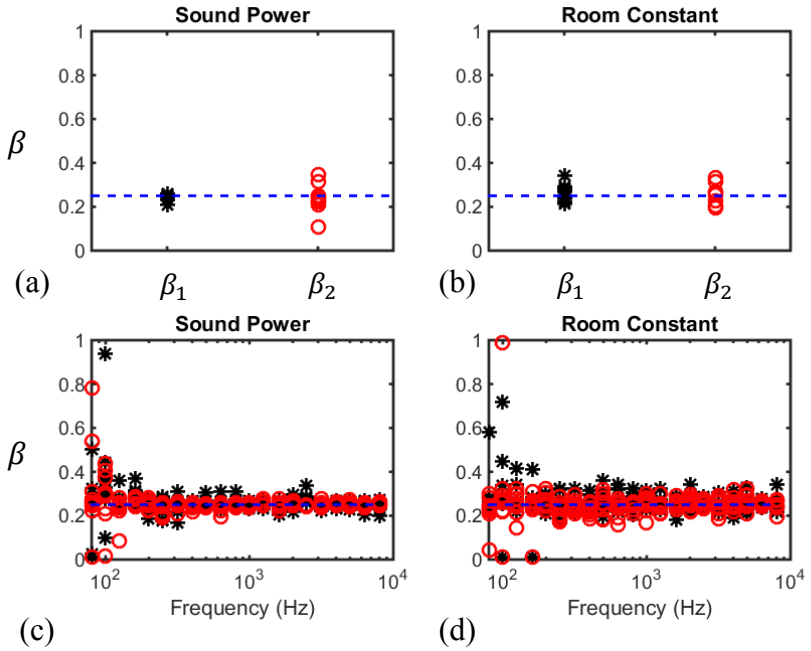

Fig. 3.11. The average GED weighting factor (β) for measurement position 1 and position 2 for (a) sound power level and (b) the room constant, optimized over the nine different rooms. It is assumed here that the same β value is used for every frequency. For (c) and (d) the β value varied by frequency for both r_1 and r_2. The near-field correction was used for this optimization [see Eq. (2.18)]. The dashed line represents $\beta = 0.25$.

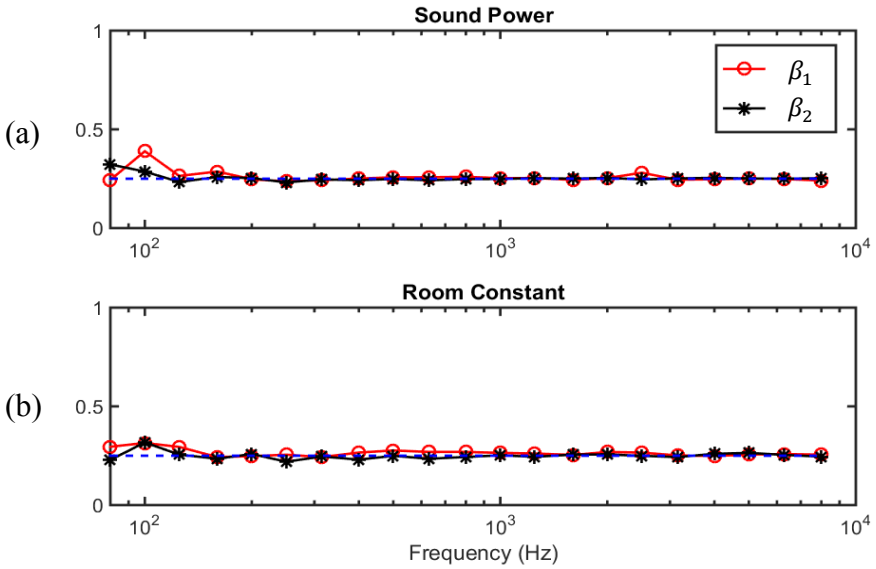

Fig. 3.12. The average GED weighting factor (β) for all nine rooms as a function of frequency for (a) sound power and (b) the room constant. The near-field correction was used for this optimization [see Eq. (2.18)]. The dashed line represents $\beta = 0.25$.

Because $\beta = 0.25$ is the optimal value for the GED measurements, it will be assumed from this point forward that GED refers to $\beta = 0.25$ and PED refers to $\beta = 1$ as before. However, it should be restated that the near-field correction is technically only valid for a monopole source.

3.3.2 Critical Distance

When using the two-point method, it is important to know where to place the measurement sensors in order to most accurately measure the room constant and sound power. Marquez noted from his experimental work that if one measurement was in the predominantly direct field region and the other was in the predominantly reverberant field region, the results tended to be better.[15] From the DOE, we were able to use randomly placed two-point simulations to determine the most accurate placements. By using the known critical distances as a metric, three different placement methods were explored: (1) both points were in the region dominated by the reverberant energy (outside the the critical distance), (2) both points were in

the region dominated by the direct energy (inside the the critical distance), and (3) one point was in each region (both sides of critical distance).

The average RMSEs of all simulations for all nine rooms are shown in Fig. 3.13, where two different measurement quantities are compared, namely PED and GED. The results from the simulations confirm Marquez's assertion that it is beneficial to have one point on each side of the critical distance for both energy quantities.

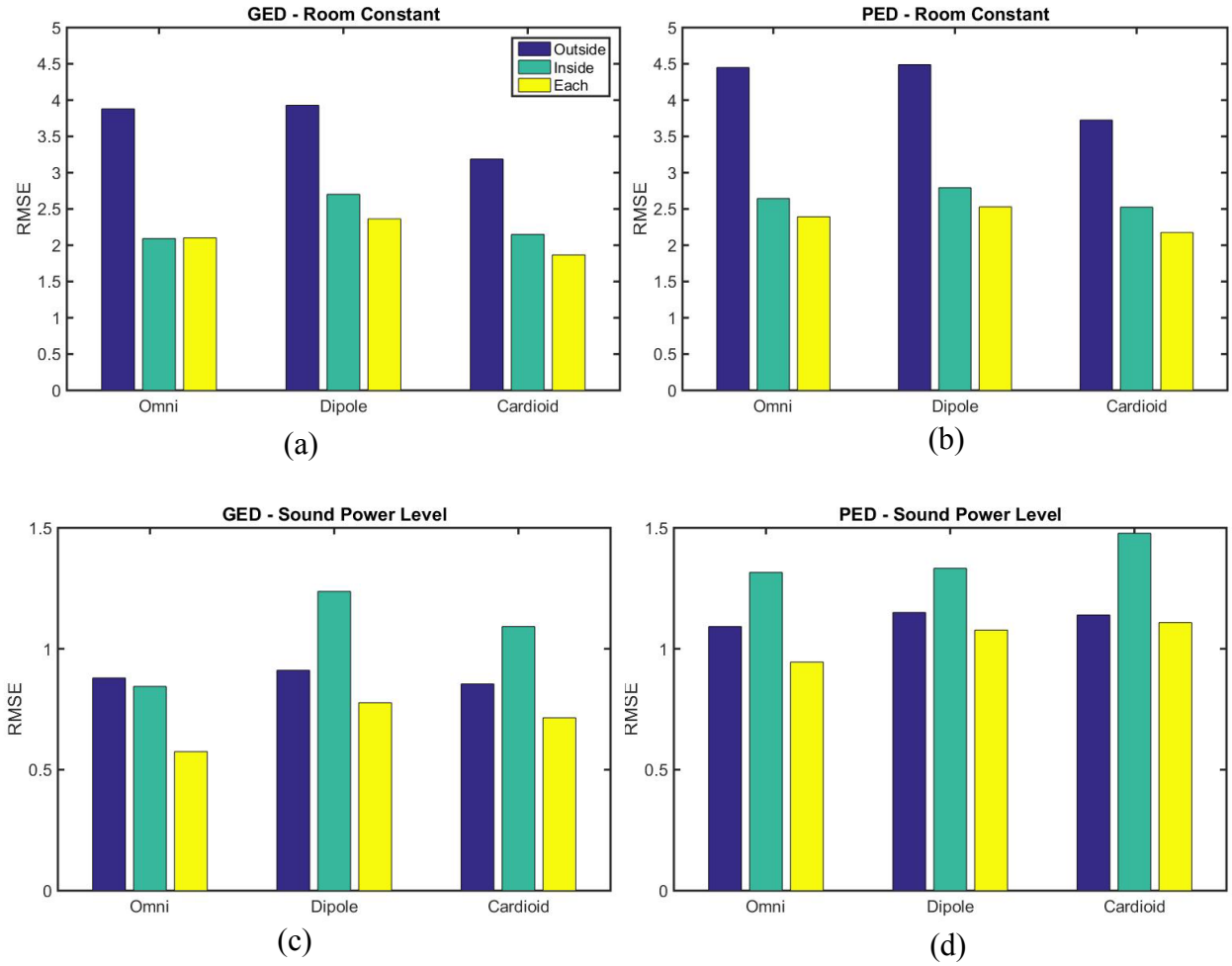

Fig. 3.13. Error as a function of measurement positions both inside, both outside, or on each side of the critical distance. The averages of simulations in all nine rooms are shown. The graphs include: (a) $RMSE_{L_R}$ with GED as the measurement quanitity, (b) $RMSE_{L_R}$ with PED as the measurement quantity, (c) $RMSE_{L_\Pi}$ with GED as the measurement quantity, and (d) $RMSE_{L_\Pi}$ with PED as the measurement quantity. Three different source configurations were simulated: an omnidirectional source, a dipole source, and a cardioid source.

3.3.3 Spatial Averaging

To determine the best method of spatial averaging, 1,000 random measurements for each of the five spatial average types were simulated with one center point on each side of the critical distance. The average RMSEs for both the room constant and the sound power are compared in Fig. 3.14. The averages shown include all sizes of each spatial average (the minimum was 5 cm

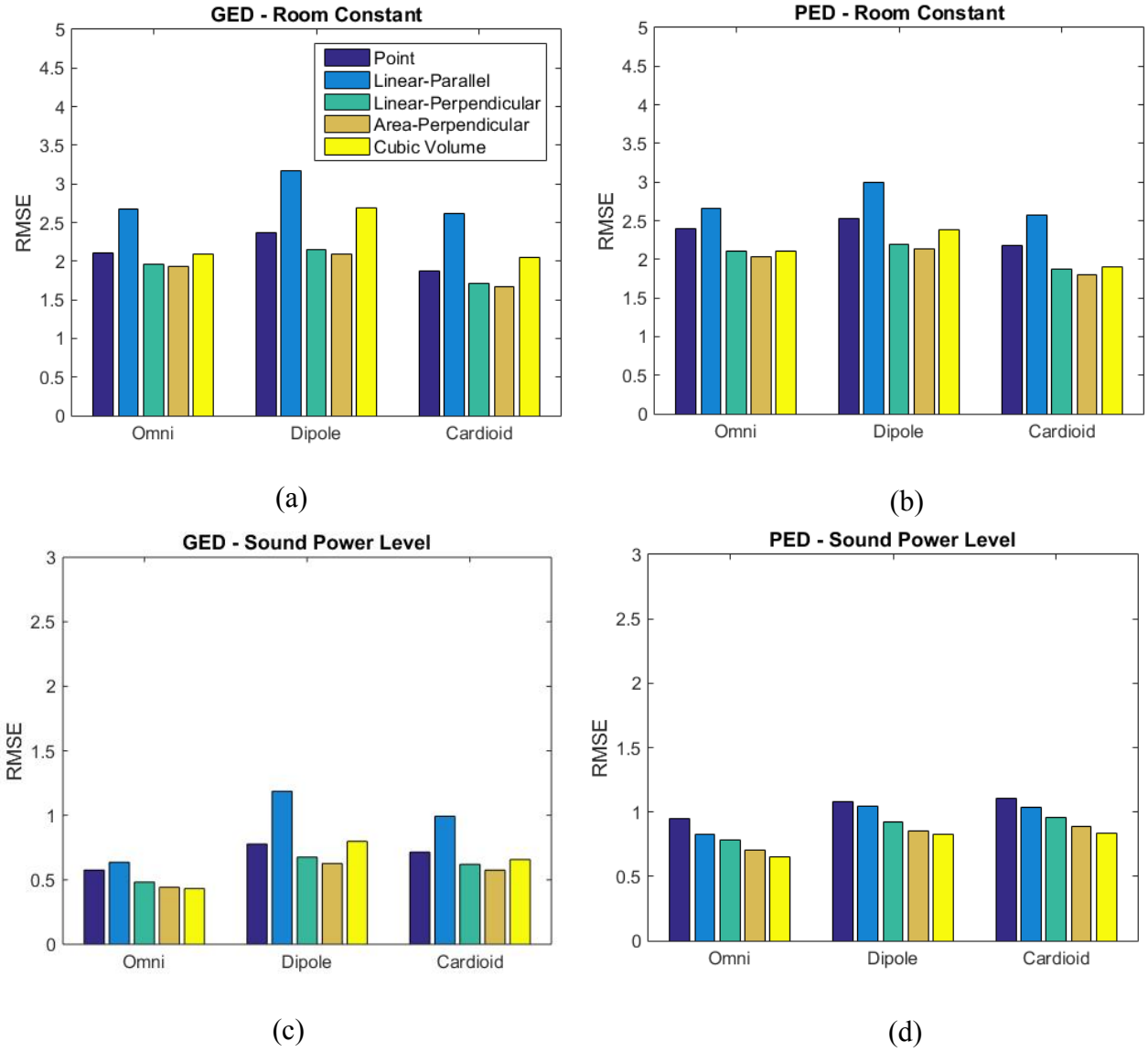

Fig. 3.14. Error as a function of different spatial averaging methods. Averages for all nine rooms are shown. The graphs include: (a) $RMSE_{L_R}$ with GED as the measurement quantity, (b) $RMSE_{L_R}$ with PED as the measurement quantity, (c) $RMSE_{L_\Pi}$ with GED as the measurement quantity, and (d) $RMSE_{L_\Pi}$ with PED as the measurement quantity. Three different source configurations were simulated, an omnidirectional source, a dipole source, and a cardioid source.

and the maximum was 1/2 of the minimum dimension of the room, with a 5 cm step size). In general, as the average expanded from a perpendicular linear average to a perpendicular area average, the error decreased. For the room constant and GED-based sound power assessment, the linear average along the axis of measurement increases the error. As suggested previously, when a spatial average around a point was taken, there were inherent errors in the average. The errors come from the fact that the directivity factors and distances of the central measurement points were known, but the directivity factors and distances to other points in the spatial average regions were not fully accounted for.

These discrepancies were reduced in the reverberant field, where one might expect differences in distance from the source and directivity factor to become more negligible. Closer to the source, the discrepancies were more pronounced. For example, in the near field of a point source, as pointed out earlier, one finds that the GED increases rapidly as the measurement position approaches the source. If a spatial average causes the measurement to extend closer to the source, the energy density will likely be overestimated, causing errors in both the room constant and sound power measurements. From Fig. 3.14, it can be seen that the best averages for GED are linear average or area averages, perpendicular to the axis of measurement. These approaches reduce the errors associated with misrepresented distances to the various averaging points. Errors in the directivity factor, at least for the sources explored in this study, were of smaller consequence.

3.3.4 Spatial Averaging Size

From Xu's work on generalized energy density, we know that with $\beta = 0.25$ in a diffuse field, the GED has a higher spatial correlation than PED.[14] Because of this, one would expect an average of the same size to actually be more effective for PED. In order to test this assertion,

100 random measurements were simulated with one point on each side of the critical distance for all nine rooms in the DOE. A spatial average was then simulated at each point. The perpendicular linear and area spatial averages were used for this test, as they seemed to be the most practical and effective. The room constant and sound power level were then measured with the spatial averages increasing in size. The average RMSEs of both are shown in Fig. 3.15. They begin at a point measurement then increase in size (length for the linear average and square root of the area for the area average) until half of the minimum dimension of the room ($L_{min}/2$). The x-axis of the plots is normalized such that A_{sz} is the average length A_l for the linear average and the square root of the average area $A_{sz} = \sqrt{A_s}$ for the area average. The results shown are for the cardioid source, but the other sources showed very similar trends.

For a point measurement, the error is lower for GED than for PED, as expected. As the average size increases, the error decreases monotonically for sound power level but with little

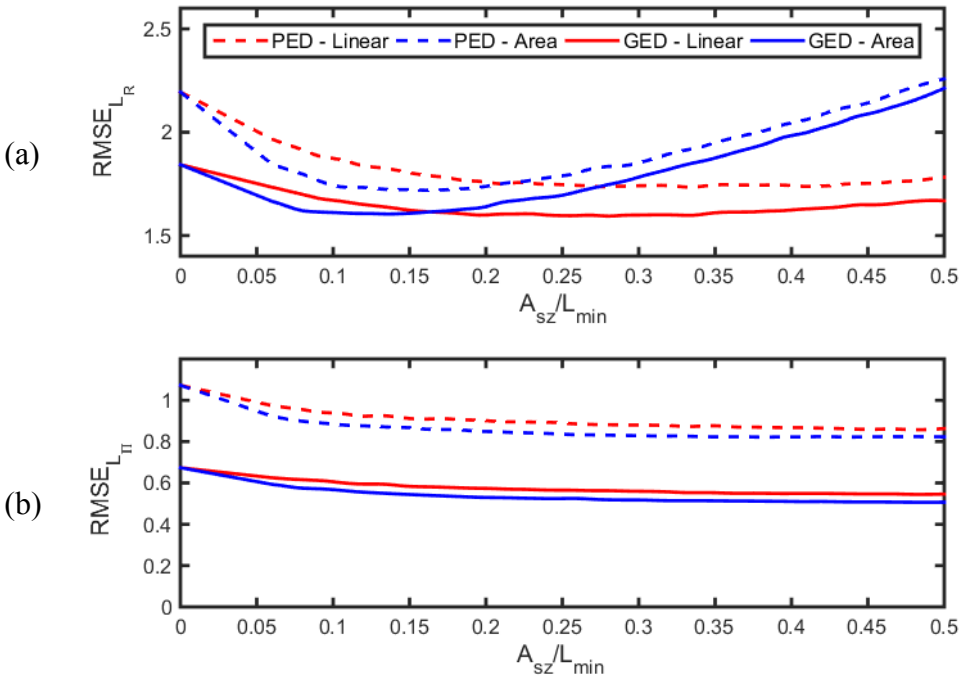

Fig. 3.15. Average RMSE as a function of average size divided by the smallest room dimensions for (a) the room constant and (b) the sound power level. The spatial averages are performed at each measurement position.

incremental benefit above about 15% of L_{min}. For the room constant, an average size larger than about 15% of L_{min} actually causes the RMSE to increase. The average size is equal about both central points in this case. The increase in error is likely due to directivity and distance estimation errors. For the $RMSE_{L_R}$ measured with GED, it appears that the most accurate area or linear average would be between about 10% to 25% of L_{min}. Because larger spatial averages lead to larger errors in measured angle and distance at positions closer to the source, the RMSE is also potentially larger at these points. With that in mind, the same test was run again, but without spatial averaging for the point closer to the source. The results from that experiment are shown in Fig. 3.16. They show a more expected trend in error reduction, which converges as the average about the more distant point gets larger for both the room constant and the sound power level.

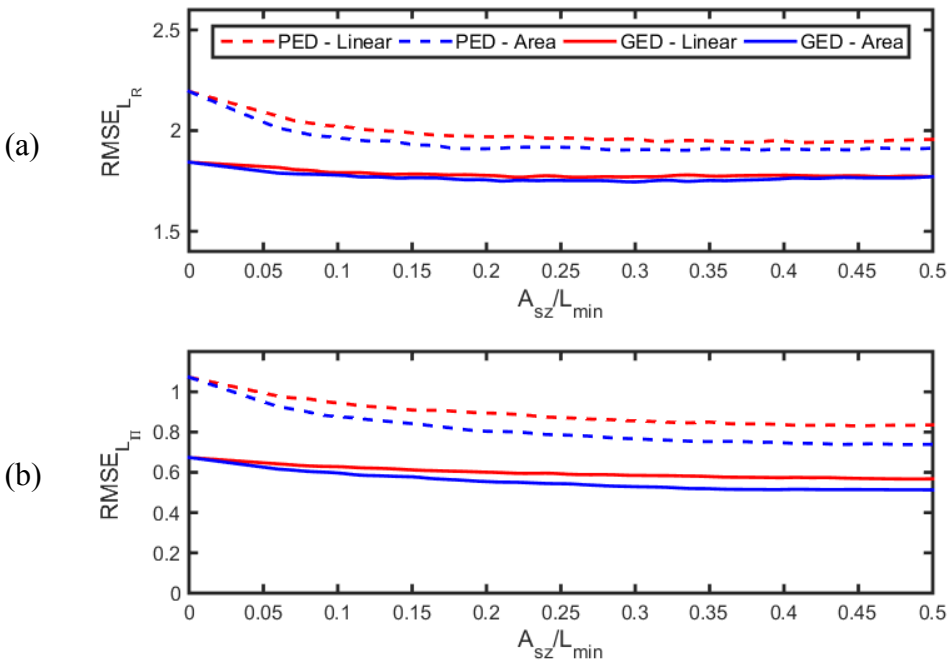

Fig. 3.16. Average RMSE as a function of average size divided by the smallest room dimensions for (a) the room constant and (b) the sound power level. In this case, the average was only performed about the point past the critical distance where the reverberant field dominates.

Considering the spatial correlation mentioned earlier, we expect the error to decrease more rapidly for PED than GED as the spatial average gets larger. This effect can be seen in Fig. 3.16 as the error for PED decreases more rapidly than the error for GED, especially when moving from a point measurement to a small average. At the same time, the results demonstrate the superiority of GED for any averaging size and its benefit as a point measurement.

The average RMSE results also show that for sound power level, a spatial average at both points or only one spatial average in the reverberant field and a point measurement in the near field produce essentially the same error. On the other hand, for the room constant, a small spatial average in both the direct and reverberant fields can yield an error that is lower than that produced by only one spatial average in the reverberant field.

3.4 Rooms with Nonuniform Absorption

The simulations in the DOE were done with a model that assumed uniform absorption on the walls, floor, and ceiling. The assumptions made for the Hopkins-Stryker equation rely on the diffuse nature of the reverberant field, which in turn relies on the assumption that the absorption in the room is distributed rather uniformly. Since that is often not the case in practice, an image source model was used to simulate a room with nonuniform absorption. A hybrid image-source and ray-tracing software package called EASE™ was also used to simulate rooms with nonuniform absorption as well as scattering surfaces and objects.

3.4.1 Image Source Method

The image source method used for this research was based mainly on that described by Lehman and Johannson, which in turn was based on the method of Allen and Berkley.[24,25] The sound pressure at any point in a room can be found from the addition of the pressure of a

principal source and numerous image sources. Each image source amplitude is multiplied by the pressure reflection coefficient of the boundary it is reflected from. The method allows a separate reflection coefficient to be used for each boundary, whereas the HMMA method requires that opposing parallel boundaries have the same impedance values. More details about the image source method can be found in Appendix A.

Four modeled rooms each had dimensions of (5 × 6 × 7) m, with the source located 1.5 meters from the origin in each direction. The varied absorption coefficients of the walls for each room are shown in Table 3.2. While each room has the same average absorption coefficient, the nonuniformity of the boundaries increases with increasing room number.

It was necessary to ensure that a sufficient number of image sources were included in the summations, in a manner similar to including sufficient terms in the modal expansion method. This was done by plotting the energetically averaged sound pressure level of several points throughout each modeled room as a function of the number of image sources. The results are shown in Fig. 3.17 for all four rooms. The average sound pressure levels are plotted relative to the final average rms sound pressure with 150,000 image sources. The number of image sources used in the model was about 100,000, where all four rooms have converged to within ±0.1 dB, as shown in the graphs.

Table 3.2. The wall absorption coefficients for four rooms modeled by the image source method.

Wall	Room Number			
	1	2	3	4
$x = 0$	0.15	0.20	0.13	0.02
$y = 0$	0.15	0.15	0.08	0.40
$z = 0$	0.15	0.10	0.01	0.10
$x = L_x$	0.15	0.10	0.08	0.05
$y = L_y$	0.15	0.15	0.13	0.01
$z = L_z$	0.15	0.20	0.40	0.25

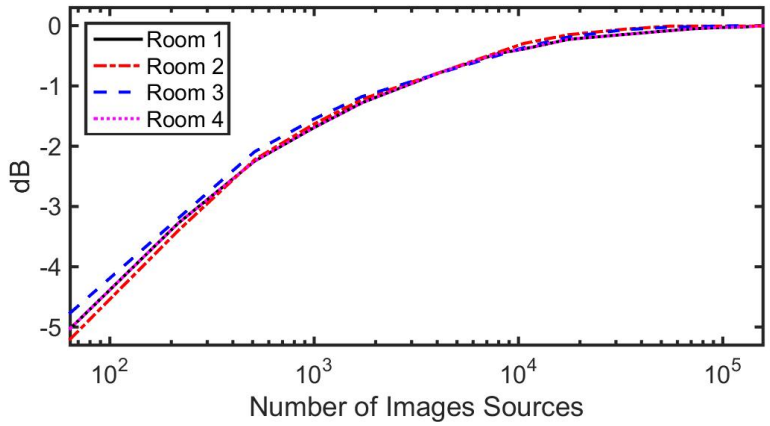

Fig. 3.17. Convergence of the image source method for the number of image sources used for each room. The dB value plotted is the average rms pressure relative to the final value for 150,000 image sources.

The room constant and the sound power associated with the three sources used previously (monopole, dipole, and cardioid) were again measured via simulation using point measurements for each of the four rooms mentioned. The RMSEs are shown in Fig. 3.18 for each of the sources in each modeled room. As expected, the room with the most nonuniform boundary absorption also tends to show the largest error. A few more observations can be made from the results. First, GED is less affected by the nonuniformities than PED, which suggests that it is still more spatially uniform. Second, the dipole source has the largest increase in error for the most nonuniform room.

3.4.2 EASE Models

To test the two-point method with more complex rooms, a few rooms located on the BYU campus were modeled in the EASE room acoustics simulation program.[42] The software is generally used for architectural acoustics and sound system design problems. As such, it allows one to model complex rooms while placing source and listening positions anywhere within the room. It uses a combination of image source and ray-tracing methods to model the sound field.

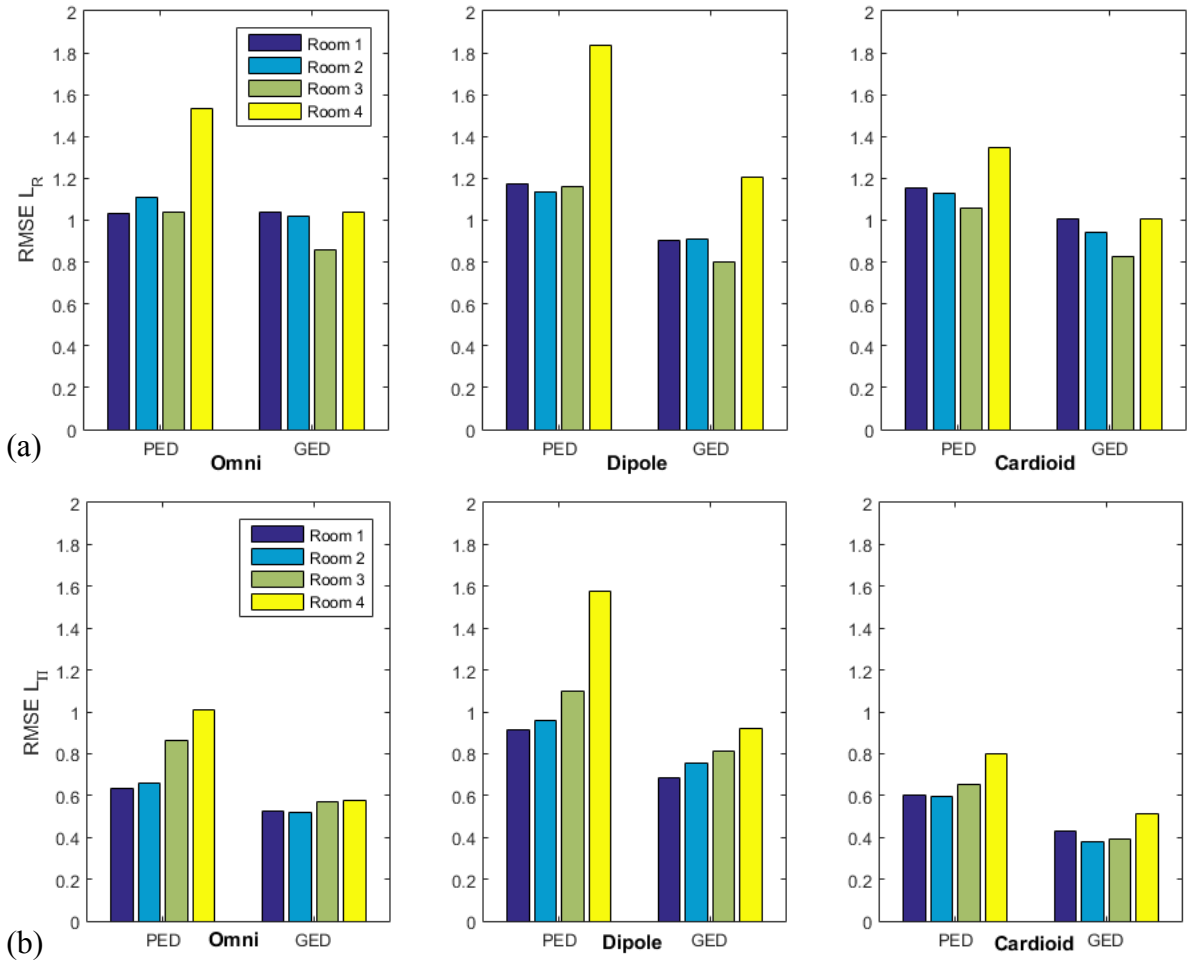

Fig. 3.18. Error from nonuniform boundary conditions for the (a) sound power level and (b) room constant. The room was modeled with 100,000 image sources. The dimensions of the room were (5 × 6 × 7) m and the source was located 1.5 meters from the corner of the room in all directions. The results were generated from 100 random simulations in each room.

One drawback to the program is that it is only able to calculate pressure magnitudes. The author was thus unable to use GED to study the two-point method. Instead, he used PED to test some of the indicated guidelines in a few rooms. The number of rays was 217,000 for all simulations.

The first was the VAC, represented in Fig. 3.19. The walls were modeled with spatially uniform absorption coefficients based on the actual 1/3 octave band reverberation time measurements. The sensor positions are represented by the chairs in the figure and the source is represented by the loudspeaker. The source in the model is a monopole. The sensor positions for the two-point method are located at distances of 0.3 and 1.3 meters from the source. Linear

spatial averages perpendicular to the axis of measurement were also used. The reverberation time in the room was calculated from the impulse response generated by the software. The classical room constant [Eq. (2.29)] then followed from the Eyring-Norris equation.[6] The free-space sound power level of the source was an input into the software and was designed to be a flat 107.6 dB based on the efficiency of the source defined in the software. The theoretical room

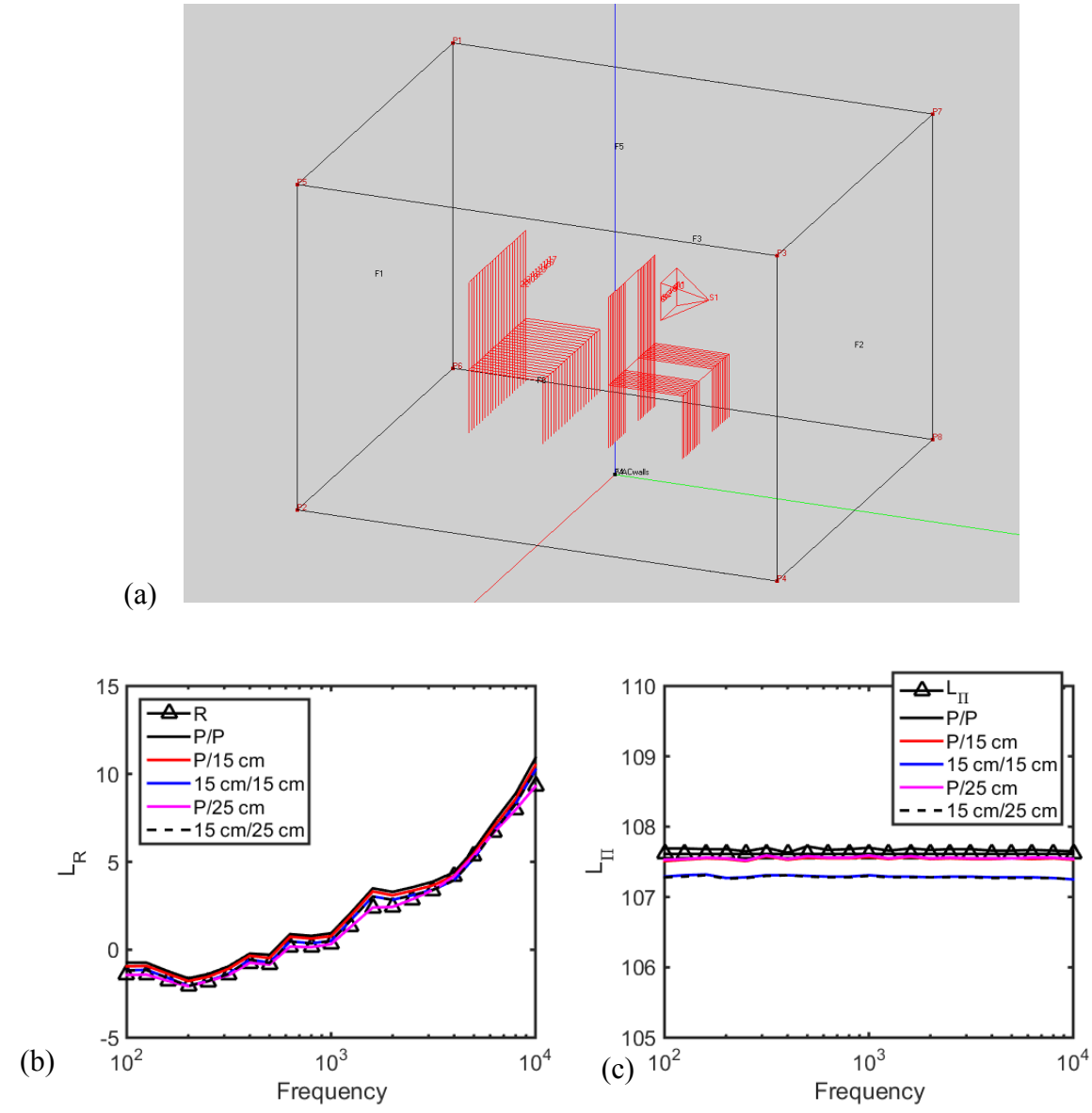

Fig. 3.19. (a) The VAC modeled in EASE. The chairs represent sensor positions. (b) The theoretical room constant (triangles) compared with several two-point method simulations. (c) The theoretical sound power level (triangles) compared with two-point method simulations. In the legends, the size of measurement for each position is noted before and after the slash e.g., a point measurement for r_1 and a 15 cm spatial average for r_2 is denoted by P/15 cm.

constant and sound power level are shown in Fig. 3.19, along with measurements simulated in EASE for a number of linear spatial averaging combinations, perpendicular to the axis of measurement. In general, the two-point method measured the room constant and the sound power level well in the VAC. The best combination seemed to be a point measurement near the source and a small average in the predominantly reverberant field. This coincides with what was found from the DOE.

Another room that was modeled was a BYU lecture hall (Eyring Science Center room C215) as depicted in Fig. 3.20. The first source was a monopole in the hall. The theoretical

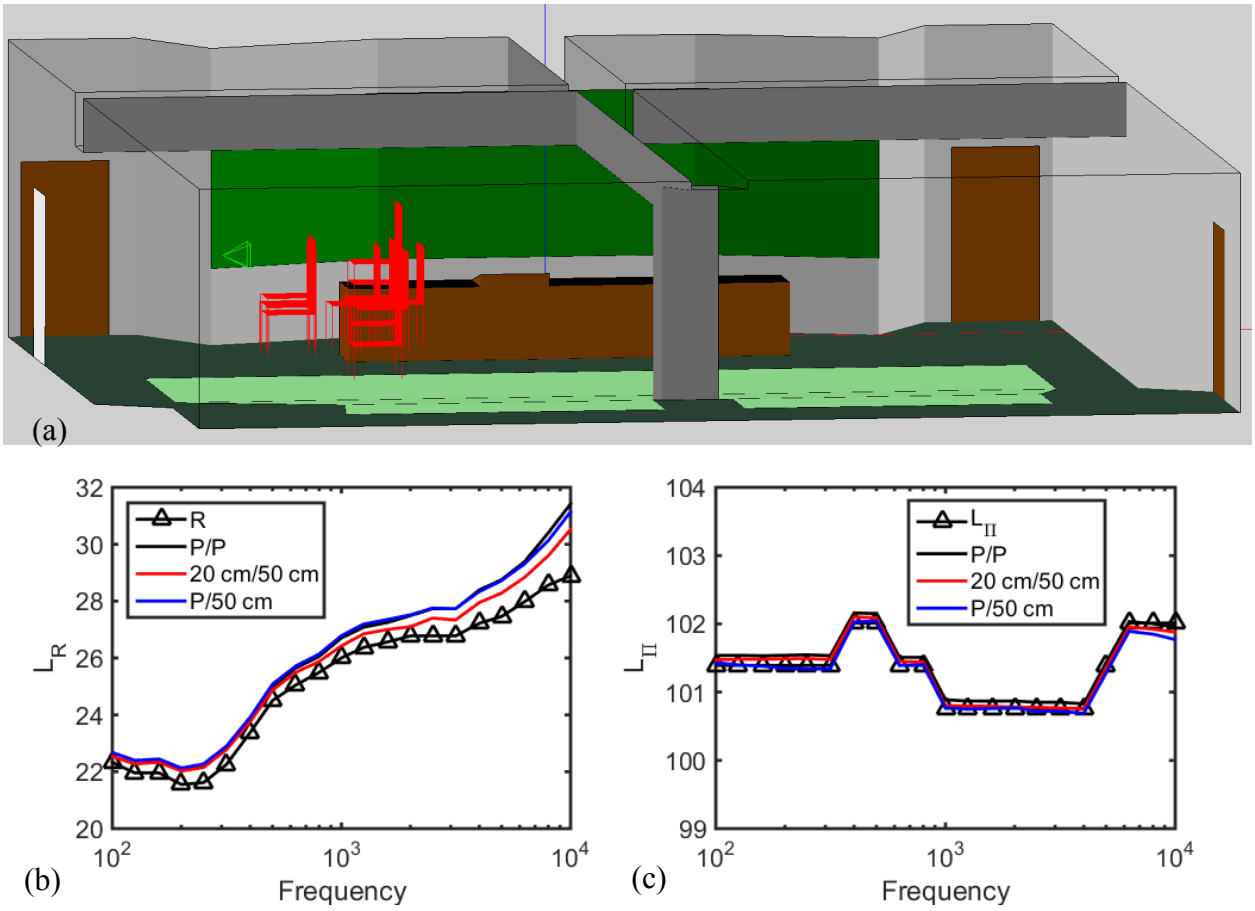

Fig. 3.20. (a) An EASE model of room C215 in the BYU Eyring Science Center. (b) The actual room constant compared with measured room constants using the simulated two-point method. (c) The actual sound power of the source compared with measured sound power levels using the simulated two-point method. In the legend, the size of measurement for each position is noted before and after the slash, e.g. a point measurement for r_1 and a 50 cm spatial average for r_2 is denoted by P/50 cm.

room constant and sound power level are again compared to simulated measurements in Fig. 3.20. The results show that the room constant measurements are somewhat overestimated, especially at higher frequencies, while the sound power measurements are quite accurate for all averaging methods.

A more directional source was also used in the room model, which simulated an average male talker. The software includes a defined frequency-dependent directivity factor and sound power which was used for the experiment. The on-axis directivity factor of the source and the results from the test are shown in Fig. 3.21. The two-point method again measured the sound power level quite well. However, the room constant assessment had even more error at the higher frequencies for the directional source. It is difficult to know exactly why the directional

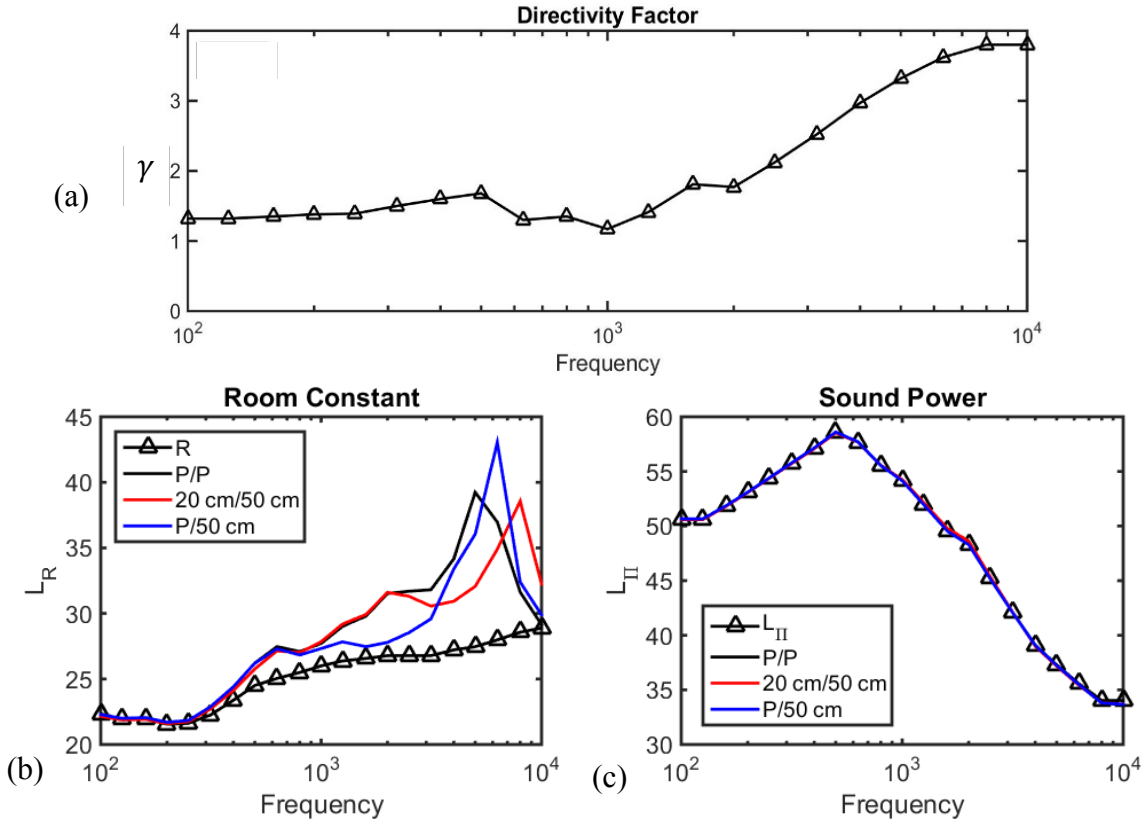

Fig. 3.21. (a) The on-axis directivity factor of a human male talker, modeled in room C215 in the BYU Eyring Science Center. (b) The actual room constant compared with measured room constants using the simulated two-point method. (c) The actual sound power of the source compared with measured sound power level using the simulated two-point method. In the legend, the size of measurement for each position is noted before and after the slash, e.g., a point measurement for r_1 and a 50 cm spatial average for r_2 is denoted by P/50 cm.

source produced more error, as the algorithms used in the software and their reliability are unkown.

One explanation for greater error at higher frequencies could be the fact that the room absorption is so high at those frequencies. Larger errors were also seen from the DOE for rooms with higher room constants. Even for a large room, the reverberant field is no longer diffuse with sufficiently high levels of absorption. The sound power measurement was still measured quite accurately, even with large errors in the room constant. Again, this could be due to the fact that the actual room constant is so large that the errors do not significantly affect the sound power (see the discussion in Sec. 3.2.1).

3.5 Conclusions

The investigation reported in this chapter found that for the near-field corrected version of the Hopkins-Stryker equation, the best GED weighting factor for semi-reverberant rooms was $\beta = 0.25$ for all points and all frequencies above the Schroeder frequency. This is consistent with the results of prior work. It also confirmed that the best positions for the measurement sensors in the two-point method involves one sensor on each side of the critical distance, well within the direct and reverberant field regions. This ensures that both the direct field energy and the reverberant field energy become dominant at one of the sensor positions.

Spatial averaging decreases the measurement error of the room constant and sound power level. For GED, the perpendicular linear average or the perpendicular area average seem to have the most practical benefit, as they would be simple to implement and have a lower error. For point measurements, the GED is typically more accurate than the PED. As expected from theory, the spatial average is more beneficial for PED than for GED due to the high spatial correlation of the latter. However, averaged GED measurements generally outperform averaged

PED measurements. The averaging method with the lowest error on average was a small spatial average, roughly 10% to 25% of the smallest room dimension for both measurement points. In some cases, a single point measurement in the predominantly direct field and a spatial average in the predominantly reverberant field produces the best results. The most accurate spatial average was the area average, perpendicular to the source. The linear average perpendicular to the source was also accurate, and may be more practical for some applications.

As the nonuniformity of the room boundary absorption increases, the errors in the room constant and sound power measurements increase as well. This is expected, as the underlying theory relies on uniformly distributed boundary absorption to create a diffuse field. The GED performs better than PED under nonuniform conditions. It seems to be robust, as long as the nonuniformity of the boundaries is not too extreme.

Chapter 4

Experimental Results

4.1 Energy Density Measurements

The following results are from experiments using the two-point method to measure the room constant and sound power of a source. The energy density was measured using a G.R.A.S. 50VI-1 vector intensity probe. The sensor includes three pairs of phase-matched microphones, facing each other, with an intervening spacer. The particular spacer used in these experiments was 25 mm in length, producing a working frequency range from about 125 Hz to 5,500 Hz.[26]

Pascal and Li presented a systematic method of measuring PED and KED by using the finite-difference method, the auto-spectrum, and the cross-spectrum of the six microphone signals.[27] The PED is given by the expression

$$\text{PED} = \frac{1}{24\rho_0 c^2}\sum_{i=1}^{6} G_{ii} + \frac{1}{12\rho_0 c^2}[C_{21} + C_{43} + C_{65}] \tag{4.1}$$

and the KED is given similarly by

$$\text{KED} = \frac{1}{2\rho_0 c^2 k^2 d^2} \sum_{i=1}^{6} G_{ii} - \frac{1}{\rho_0 c^2 k^2 d^2} [C_{21} + C_{43} + C_{65}], \tag{4.2}$$

where ρ_0 is the density of air, c is the speed of sound, k is the wavenumber, d is the microphone spacing, G_{ii} is the auto-spectrum of the ith microphone, and C_{ij} is the real part of the cross-spectrum between the ith and jth microphone.

4.2 Variable Acoustics Chamber

The VAC was used as the main laboratory environment for studying the two-point method. In its most basic configuration, it is a small room with smooth rigid boundaries and no scattering objects or furnishings. It is a rectangular parallelepiped, which allows for simple calculation of the volume and surface area with accurate results. These facts made room constant calculations more simple and accurate.

Three different absorption configurations were used to vary the room constant. In order to change its behavior, blankets were hung on the walls to increase absorption. The absorption coefficients of the blankets were measured separately in a 210 m^3 reverberation chamber according to ISO 354 as shown in Fig. 4.1.[28] The classical frequency-dependent room constant of the VAC was then calculated using Eq. (2.29), the surface area and absorption coefficients of the empty VAC, by subtracting the absorption area of the rigid walls that were covered by the blankets, and by adding the surface area and absorption coefficient of the blankets. The new average absorption coefficient was then

$$\bar{\alpha} = \frac{\sum_i S_i \alpha_i}{\sum_i S_i}, \tag{4.3}$$

Fig. 4.1. The experimental setup for measuring the absorption coefficients of the blanket in the BYU reverberation chamber. A 20 cm dodecahedron loudspeaker was used as the excitation source and the measurements were taken according to ISO 354.

where the subscript i represents the i^{th} surface in the room and the denominator is the entire surface areas\ of the room. Two blanket configurations were used: one with two blankets (one on each side of two opposing walls) and one with four blankets (one on each wall).

Table 4.1 shows the measured average absorption coefficients for the empty VAC and the absorption coefficients of a single blanket as measured in the reverberation chamber. Absorption coefficients measured above 1 at higher frequencies resulted because the edge of the blanket was not considered in its surface area and because of other measurement artifacts. The room constants for the various configurations are shown in Fig. 4.2. Since there is not much absorption at low frequencies they do not differ much at lower frequencies. Because the room is so small, the Schroeder frequency is quite high (nearly 700 Hz) when it is empty. The absorption lowers the Schroeder frequency, but the room is still limited to a usable bandwidth of about 500 to 6300 Hz, where the upper cut-off frequency is due to the limitations of the energy density sensor.

Table 4.1. The average absorption coefficient of the empty VAC and of the blanket measured in the reverberation chamber. The effective surface area of the VAC is 53.9 m^2 while that of a blanket is 3.5 m^2.

Frequency	VAC	Blanket	Frequency	VAC	Blanket
100 Hz	0.01	0.01	1250 Hz	0.03	0.91
125 Hz	0.01	0.07	1600 Hz	0.03	0.98
160 Hz	0.01	0.11	2000 Hz	0.04	1.06
200 Hz	0.01	0.09	2500 Hz	0.04	1.08
250 Hz	0.01	0.18	3150 Hz	0.05	1.11
315 Hz	0.01	0.24	4000 Hz	0.06	1.25
400 Hz	0.02	0.32	5000 Hz	0.08	1.27
500 Hz	0.02	0.44	6300 Hz	0.10	1.33
630 Hz	0.02	0.50	8000 Hz	0.13	1.25
800 Hz	0.02	0.63	10000 Hz	0.16	1.37
1000 Hz	0.02	0.76			

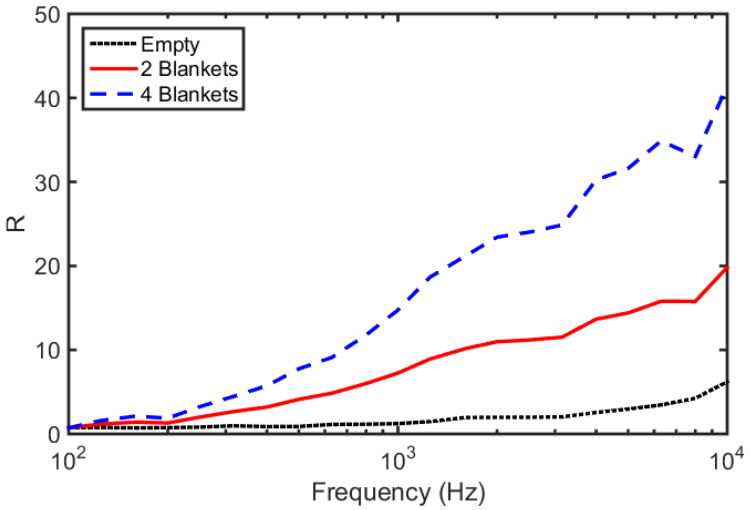

Fig. 4.2. Different room constant configurations in the Variable Acoustics Chamber (VAC). The room constants were calculated using Eq. (2.29) and the absorption coefficient for the blankets measured using ISO 354.

4.3 Near-Field Correction

In order to experimentally verify the near-field correction to the Hopkins-Stryker equation it was necessary to use a source where radiation resembled that of a monopole. A 7.5 cm diameter spherical loudspeaker with a dodecahedron driver configuration was used inside the VAC to measure the room constant for the verification. The energy density probe and dodecahedron are shown in Fig. 4.3. The dodecahedron is very small and essentially omnidirectional beyond 2 kHz.

A pulley system was used to measure the potential and kinetic energy densities along an axis moving away from the source. The room constant was measured using the two-point method for positions close to the source and positions well into the reverberant field. No spatial averaging was included. Due to the assumed omnidirectionality of the source, a directivity factor of unity was used for all frequencies when solving for the room constant. The source was also considered to have a near-field directivity factor that was more omnidirectional than that of a larger source.

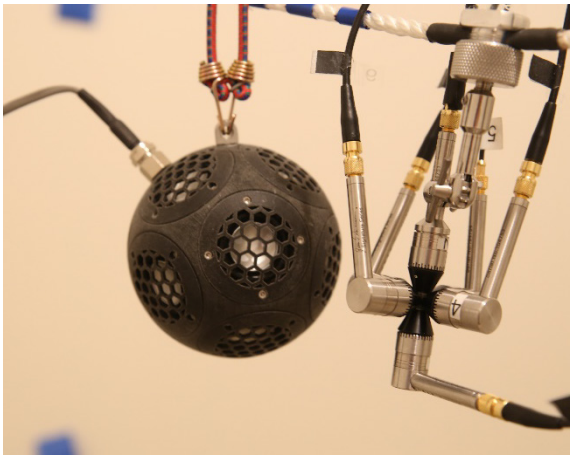

Fig. 4.3. The 7.5 cm spherical dodecahedron loudspeaker and the energy density probe in the VAC.

Figure 4.4 shows the measured logarithmic room constant L_R in the empty VAC using PED, GED, and GED with near-field corrections [see Eqs. (2.5), (2.8), and (2.19)]. These are compared to the calculated room constants based on Eqs. (2.29) and (2.31). For GED, the near-field correction provides a better measurement of the room constant at lower frequencies, as expected. Figures 4.5 and 4.6 show similar results for the two-blanket and four-blanket VAC configurations. These results also show the superiority of GED and that the near-field correction is necessary and beneficial when making some measurements close to the source. The accuracy of the room constant measurement might be improved by using local spatial average and a measured directivity factor (especially a near-field directivity factor) instead of an assumed omnidirectional pattern.

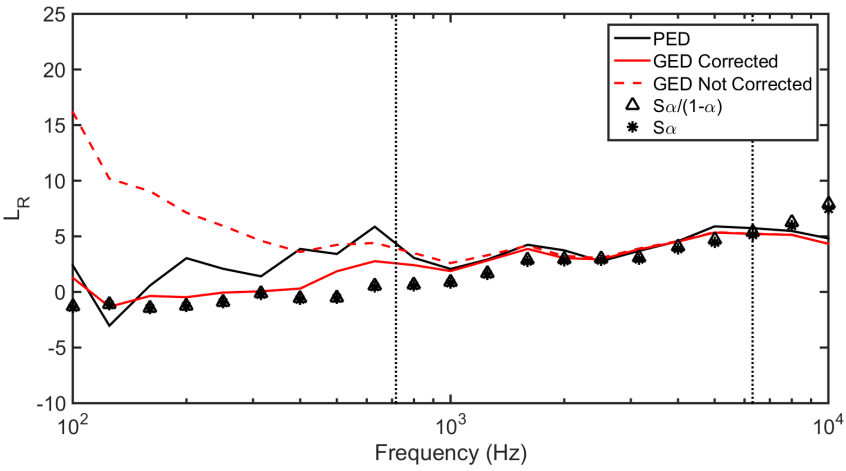

Fig. 4.4. The room constant measured using the two point method and the 7.5 cm spherical dodecahedron loudspeaker in the VAC with no blankets on the walls. The first position r_1 was 11.4 cm away from the center of the source and the second position r_2 was 1.07 m away. The dashed red line represents the uncorrected two-point method GED result and the solid red line includes the near-field correction. The vertical dashed lines are the Schroeder frequency f_s of the room with no blankets and the upper limit of the probe.

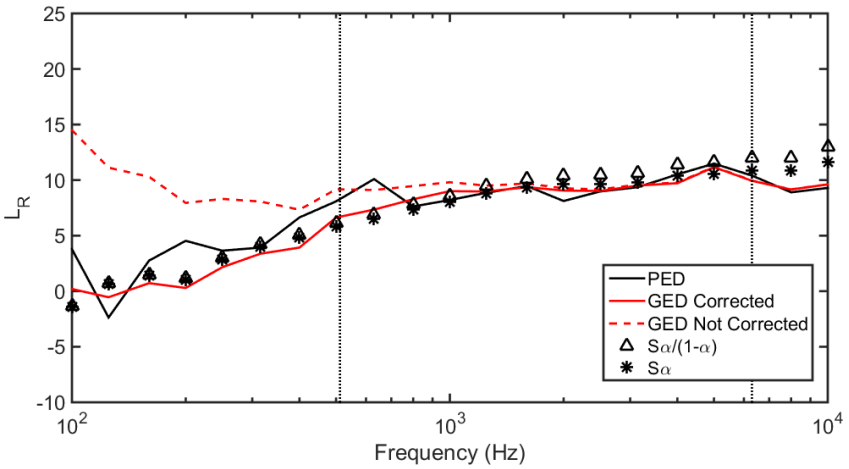

Fig. 4.5. The room constant measured using the two point method and the 7.5 cm spherical dodecahedron loudspeaker in the VAC with two blankets on the walls. The first position r_1 was 11.4 cm away from the center of the source and the second position r_2 was 1.07 m away. The dashed red line represents the uncorrected two-point method GED result and the solid red line includes the near-field correction. The vertical dashed lines are the Schroeder frequency f_s of the room with two blankets and the upper limit of the probe.

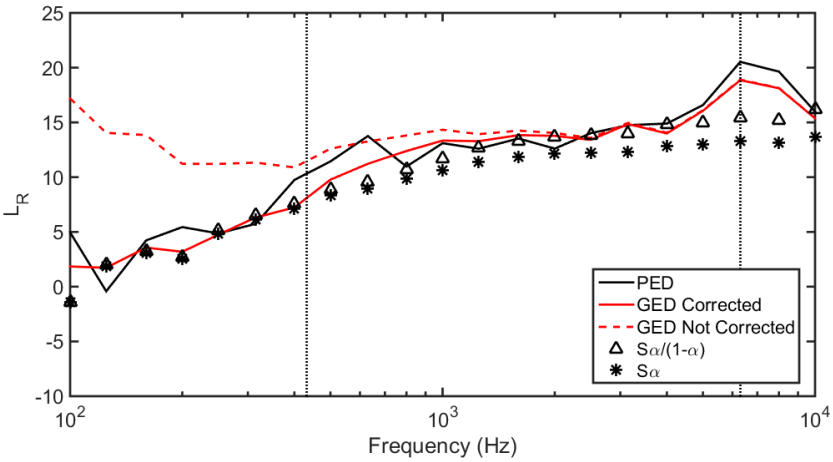

Fig. 4.6. The room constant measured using the two point method and the 7.5 cm spherical dodecahedron loudspeaker in the VAC with four blankets on the walls. The first position r_1 was 11.4 cm away from the center of the source and the second position r_2 was 1.07 m away. The dashed red line represents the uncorrected two-point method GED result and the solid red line includes the near-field correction. The vertical dashed lines are the Schroeder frequency f_s of the room with four blankets and the upper limit of the probe.

4.4 Measurement Positions

As indicated in Ch. 3, the reason for taking a measurement near a source (i.e., in the direct near field rather than the direct far field) is to ensure a measurement position on either side of the critical distance. It was shown numerically that a point well on each side gives the best results when measuring the room constant. Based on the number of measurements that were taken in the VAC, this same result can be shown experimentally.

Figure 4.7 is a scatter plot showing the RMSE of the logarithmic room constant [see Eq. (3.9)], with the Schroeder frequency as a lower frequency limit and the 6300 Hz 1/3 octave band as the upper limit. The size and color of each marker corresponds to the error level; the larger and brighter the marker, the higher the error (see the color scale). The dashed lines show the frequency averaged critical distance and divides the graph into four quadrants. The upper right quadrant represents the region wherein both points r_1 and r_2 are beyond the critical distance. Both measurements are thus dominated by the reverberant field. The lower left quadrant represents the region wherein both points are within the critical distance and dominated by the direct field. The lower right quadrant represents the best region wherein the first point is within the critical distance and the second is beyond it. The upper left region is not used because that would represent a measurement where $r_1 > r_2$, which contradicts the measurement assumption.

Figures 4.8 and 4.9 show the same results for two and four blankets in the VAC. From the figures it is clear that the lower right quadrant has the lowest error, which again suggests that one point should be on each side of the critical distance, validating what was discovered numerically and suggested by Marquez.[15]

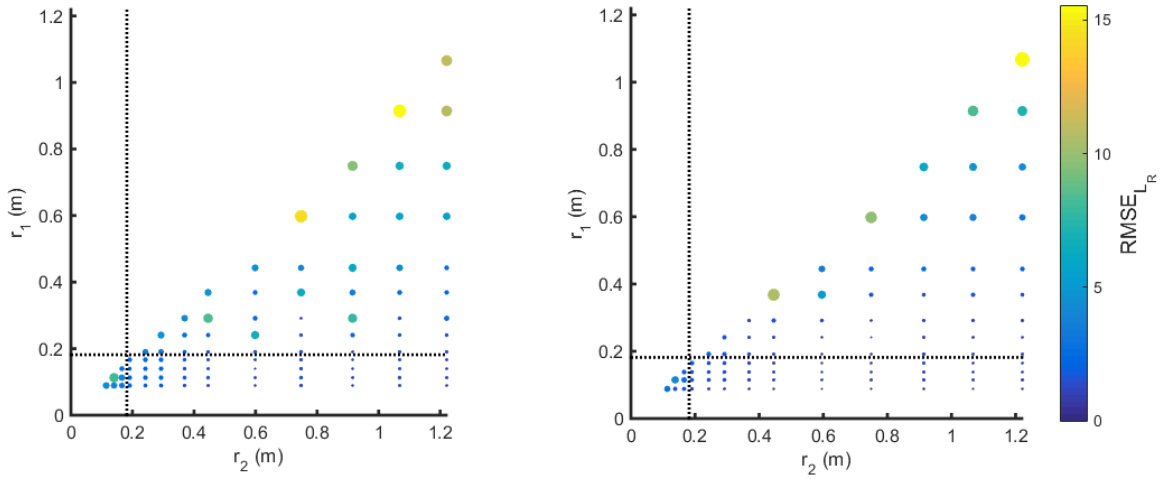

Fig. 4.7. The logarithmic RMSE of the room constant [see Eq. (3.9)] measured in the VAC with no blankets for (a) PED and (b) GED. Each point represents a specific combination of r_1 and r_2 to compute the room constant using the two-point method. The dashed lines represent the critical distance and split the graph into four quadrants. The lower left is where both points are within the critical distance (near the source). The upper right is where both points are beyond the critical distance. The lower right is where the first point is less than the critical distance and the second point is beyond it. The larger and brighter markers represent a higher error, whereas the smaller and darker markers represent lower error.

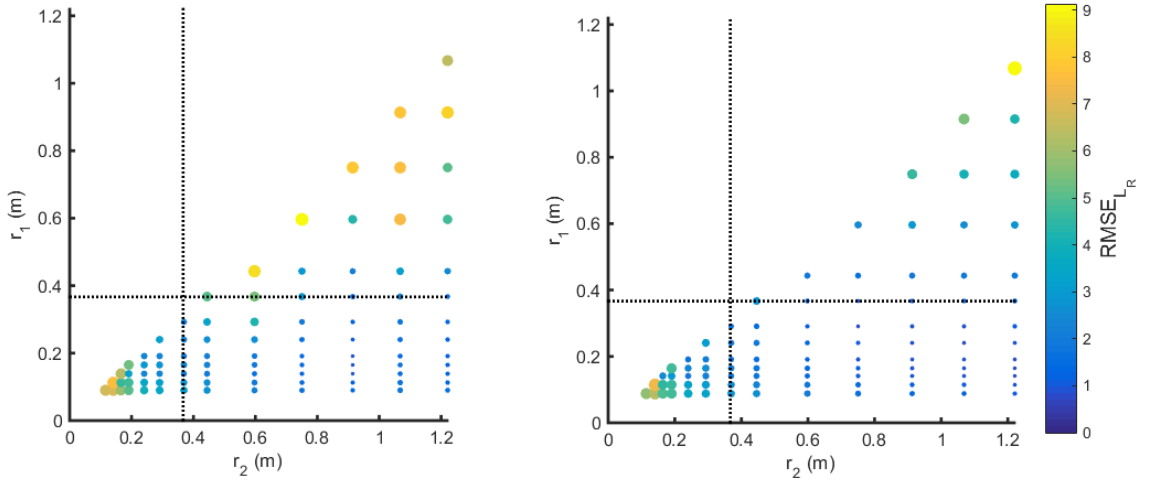

Fig. 4.8. The logarithmic RMSE of the room constant [see Eq. (3.9)] measured in the VAC with two blankets for (a) PED and (b) GED.

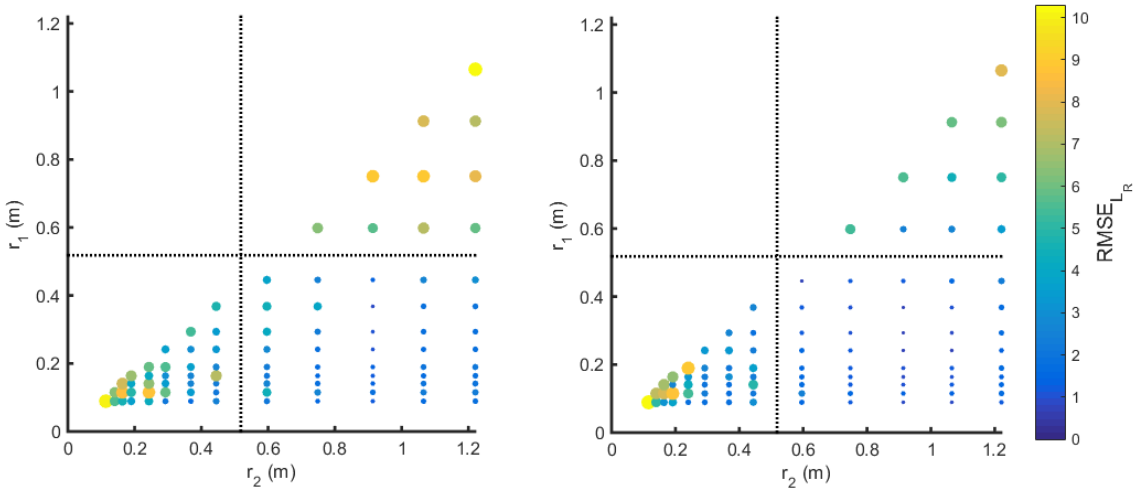

(a) (b)

Fig. 4.9. The RMSE of the room constant measured in the VAC with four blankets for (a) PED and (b) GED.

4.5 Reference Directivity Source

A reference directivity source was used for other two-point measurements, as shown in Fig. 4.10. It is a 7.6 cm full-range driver in a 22.9×15.2×10.2 cm box with a passive radiator of the same size above the active driver. The acoustic center was considered to be at the center of the dust cap on the active driver. Marquez recommended that the reference directivity source be one with

Fig. 4.10. Reference directivity loudspeaker used in the VAC with two blankets and four blankets to study the effects of spatial averaging. The lower cone is the active driver, while the upper cone is a passive radiator.

a relatively smooth directivity pattern over frequency and angle.[15] This speaker was readily available for experimentation and the directivity factor was measured according to a variant of ISO 3745. Many more measurement points were used than required to increase its accuracy and that of the sound power measurement. [5] The passive radiator complicates the directivity at lower frequencies, but not enough to require the use of another loudspeaker. Directivity factor balloons at select frequencies are shown in Fig. 4.11(a), where radius and color represent the directivity factor at different angles. Figure 4.11(b) also shows the directivity factor as a function of frequency for angles around the normal axis of the loudspeaker. It is relatively smooth around

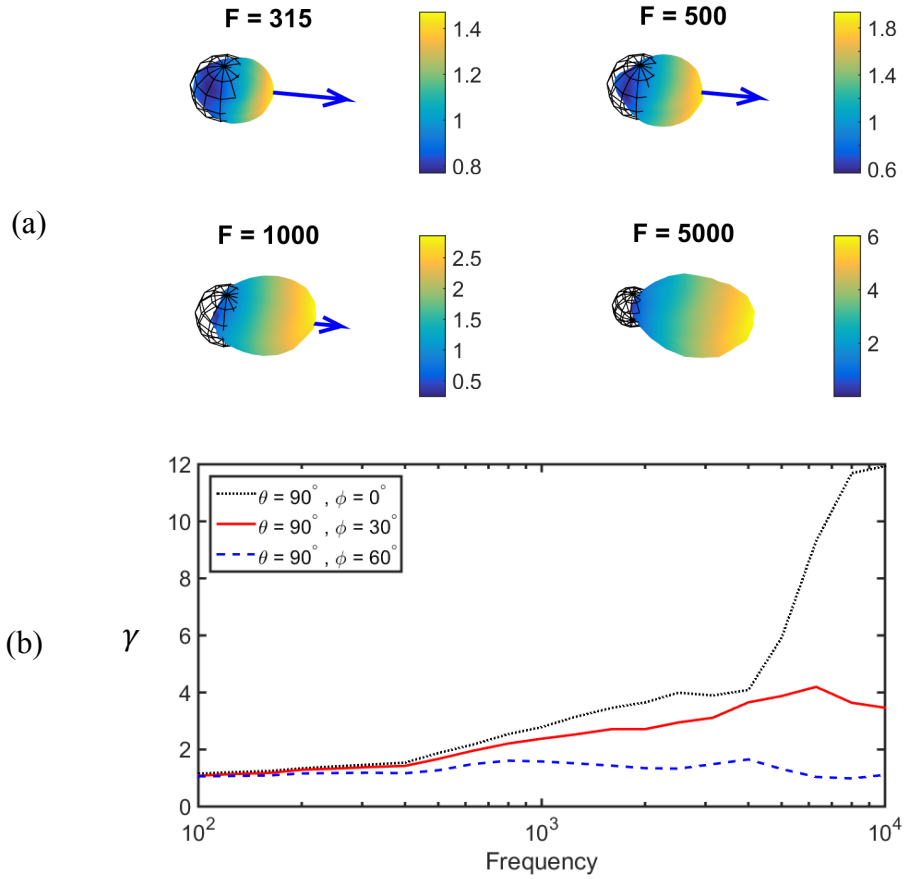

Fig. 4.11. The directivity factor of the reference sound source. (a) Balloon plots showing the directivity factor via color and radius. The blue arrows represent the principal axis, pointing directly away from the center of the active driver. The mesh sphere represents the unity directivity factor of an omnidirectional source. (b) The directivity factor as a function of frequency for several angles. The $\theta = 90°$, $\phi = 0°$ case represents the principal axis.

these positions, which means that small errors in the reference angle do not significantly affect the directivity factor value.

4.6 Spatial Averaging in the VAC

The numerical results described earlier point to local spatial averaging as a way to improve the two-point method. To explore this option experimentally, the room constant of the VAC was again measured with the two-blanket and four-blanket configurations and the reference directivity source. The source was placed at (0.915, 1.82, 1.08) m and measurements were taken along the $\theta_0 = 80°$ and $\phi_0 = 15°$ axis at 0.6 m and 1.7 m. Several measurements were also made in a linear grid about the measurement positions, about 6 cm apart, perpendicular to the axis of the measurement. The measurements of the room constant using the two-point method and the two-blanket configuration are shown in Figs. 4.12 and 4.13 for PED and GED, respectively. The near-field correction was used for the GED measurements. A point measurement is shown in comparison to a spatially averaged measurement and the classical

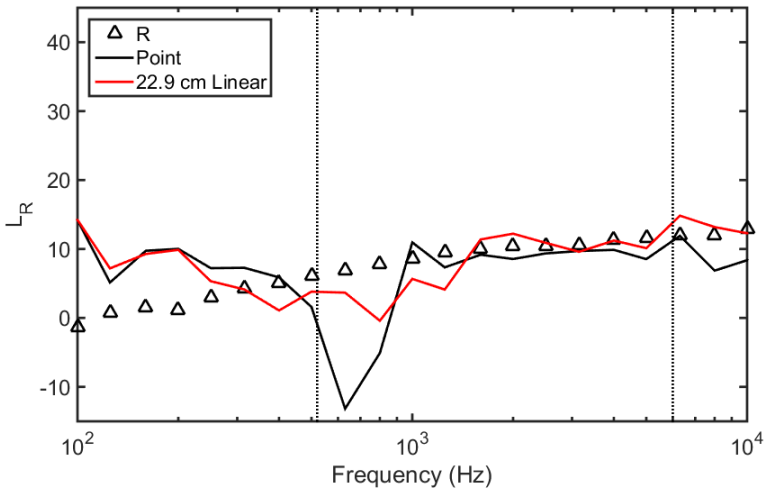

Fig. 4.12. The room constant measured in the VAC with two blankets using the reference directivity source and the two-point in situ method with PED as the measurement quantity. The calculated room constant (triangles) is compared with a point measurement and a 22.9 cm linear perpendicular average. The vertical lines represent the Schroeder frequency and the upper spectral limit of the probe.

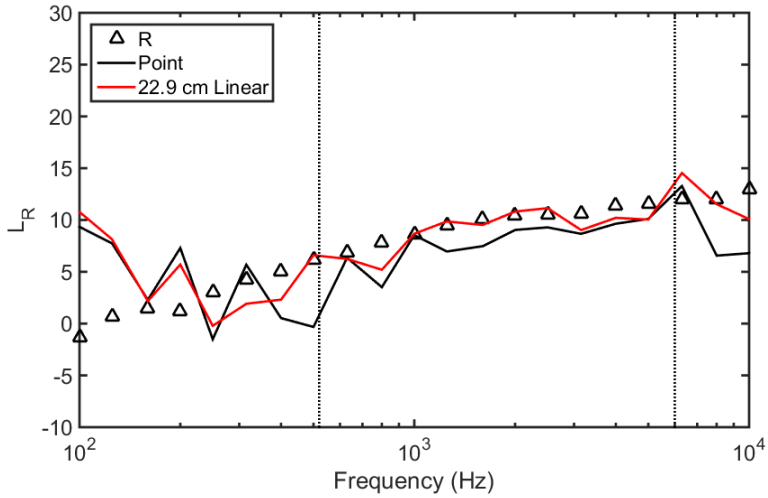

Fig. 4.13. The room constant measured in the VAC with two blankets using the reference directivity source and the two-point in situ method with GED as the measurement quantity.

prediction calculated from the reverberation time of the empty room and the measured absorption of the blankets, as described in Sec. 4.2. The spatially averaged measurement shows an improvement when compared to the point measurement. The GED also gives a better estimation of the room constant than PED for spatially averaged quantities. Figure 4.14 shows the RMSE of the room constant for several different spatial averages about both position r_1 and r_2. The spatial averages were all perpendicular to the axis of measurement. The linear averages

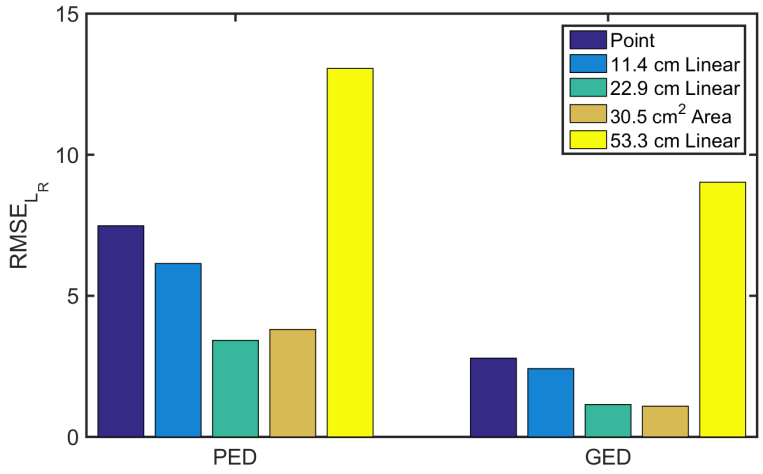

Fig. 4.14. The error in room constant as measured in the VAC with two blankets using the reference directivity source and the two-point in situ method for several different average types, all perpendicular to the measurement axis.

were 11.5 cm, 23 cm, and 53 cm long, and the area measurement was 30.5 cm^2. The grid size was 6 cm as mentioned before. Again, the reference value for the RMSE is the classical prediction of the room constant shown in Eq. (2.29).

By increasing the average size at each point, we see some improvement in the room constant measurement, especially between the Schroeder frequency and the upper usable frequency of the probe. The exception is with the 53.3 cm long linear average. As mentioned previously, there are a few possible reasons for this. First, by averaging over a large region of a line or area, there are components of the average that are at much greater distances than the distance to the center of the averaging region. This discrepancy in central distance versus actual distance to the averaging point becomes larger as the average size gets larger, thus adding to the error. Another reason is that the length of the average is nearly the same as r_1. This causes the average to sweep a large angle and consequently the directivity factor at some points of the average could be significantly different from that used at the central measurement position. To minimize this issue, the average should have a much smaller length than the distance from the source to the measurement position.

Figures 4.15, 4.16, and 4.17 are similar to the previous figures but for the four-blanket configuration of the VAC. The results are consistent with what was seen in the two-blanket configuration. A spatial average is beneficial, especially in the reverberant field, far from the source. From Figs. 4.14 and 4.17 we also see that the spatial average is significantly more beneficial for PED than GED, as discussed in Ch. 3.

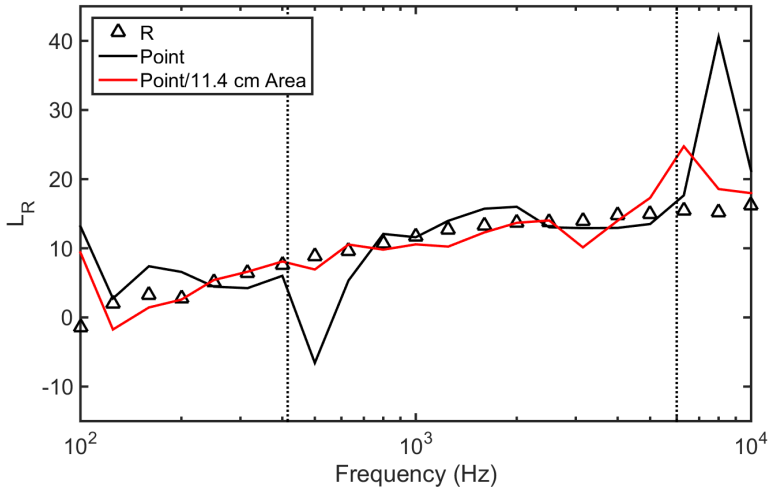

Fig. 4.15. The room constant measured in the VAC with four blankets using the reference directivity source and the two-point in situ method with PED as the measurement quantity. The legend entry Point/11.4 cm Area indicates that the spatial average was performed only about the point farthest from the source. The point near the source had no spatial averaging.

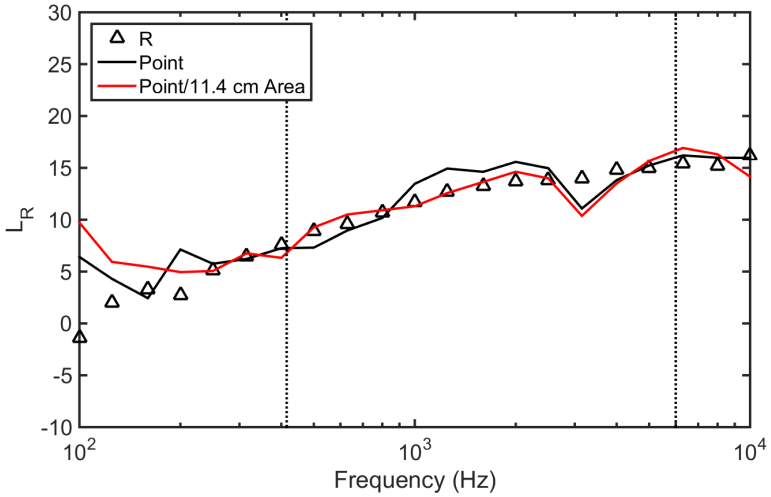

Fig. 4.16. The room constant measured in the VAC with four blankets using the reference directivity source and the two-point in situ method with GED as the measurement quantity. The legend entry Point/11.4 cm Area indicates that the spatial average was performed only about the point farthest from the source. The point near the source had no spatial averaging.

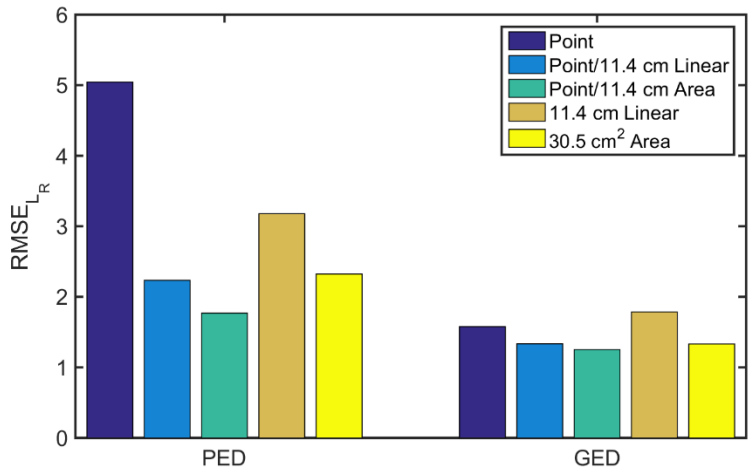

Fig. 4.17. The error in room constant as measured in the VAC with four blankets using the reference directivity source and the two-point in situ method for several different average types, all perpendicular to the measurement axis.

Measuring a spatial average by taking a grid of measurements one at a time and then averaging is not always a practical solution. A few alternatives are available to this method. If one is standing inside the room and the sensor is on a boom arm, it may be slowly "waved" around for an average during the measurement. Another alternative would be to use a rotating boom, turntable, or pulley device to trace out a spatial average during a measurement.

4.7 Sound Power Measurements

Another purpose of the two-point method is to measure the sound power of a source under less-than-ideal conditions. Several different measurements were accordingly taken to test the usefulness of the method. Marquez showed that the sound power of a loudspeaker could be measured in nonideal rooms.[15] In the work conducted for this research, a few sources with less predictable behaviors were used to further validate the approach for general field measurements.

4.7.1 Variable Acoustics Chamber

The sound powers produced by three sources were measured in the VAC. These included (1) a handheld vacuum cleaner, (2) a blender motor without a jar, and (3) a combination belt and disc sander. The vacuum and the blender had symmetries or sizes that allowed approximations of their acoustic centers near their geometric centers. However, the acoustic and geometric centers of the third source, the belt and disc sander, were more difficult to determine, making it a good case study for larger, distributed, and asymmetric sources. The sound powers of the blender and the vacuum were alternatively measured according to ISO 3741 and ISO 3745 standards. The sound power of the belt and disc sander was alternatively measured only according to ISO 3741.

In the VAC, the same reference directivity source was used as mentioned earlier, with the empty, two-blanket, and four-blanket configurations. The setup for the vacuum is pictured in Fig. 4.18 in the four-blanket configuration. When using the two-point method with a small source such as this, a single position for the device under test (DUT) and the reference directivity source can be used sequentially, which allows for more options for the two sensor positions. For larger, cumbersome to move sources, the DUT and the reference source can both be placed in the room at the same time, as pictured in Fig. 4.19.

Figures 4.20 through 4.22 show the results from the two-point in situ method for the vacuum, blender, and belt and disc sander, respectively. They each include overlaid results for the three different absorption configurations. These particular measurements were point GED measurements, rather than spatially averaged measurements. The near-field correction was applied to all sound power measurements. The results show good overall agreement for all three conditions. Table 4.2 shows the A-weighted sound power levels measured for each source.

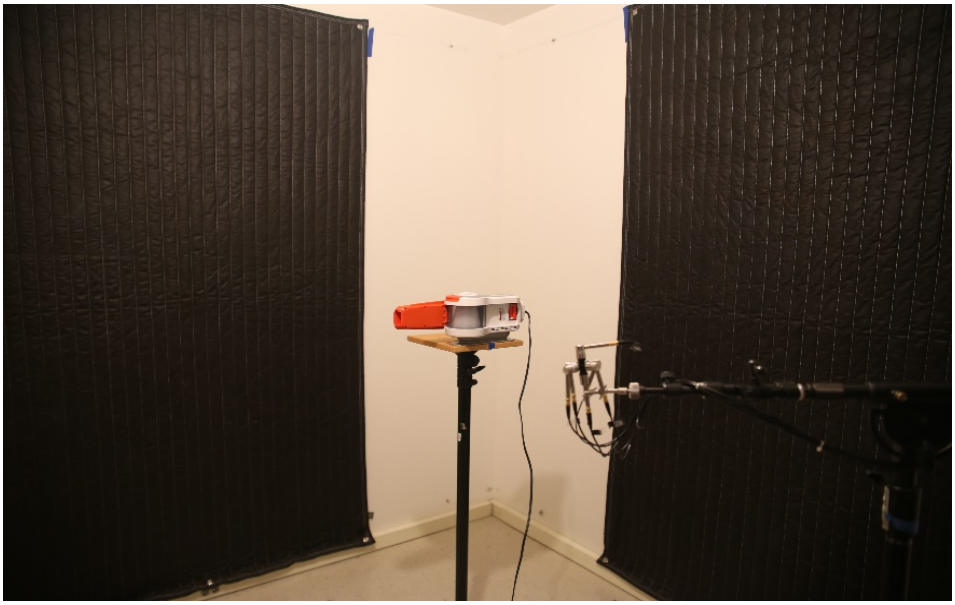

Fig. 4.18. The handheld vacuum in the VAC with the four-blanket configuration.

Fig. 4.19. The measurement configuration for the sound power of the belt and disc sander in the VAC with two blankets. The reference directivity source is on the left and the DUT is on the right. The sensor is positioned closer to the former.

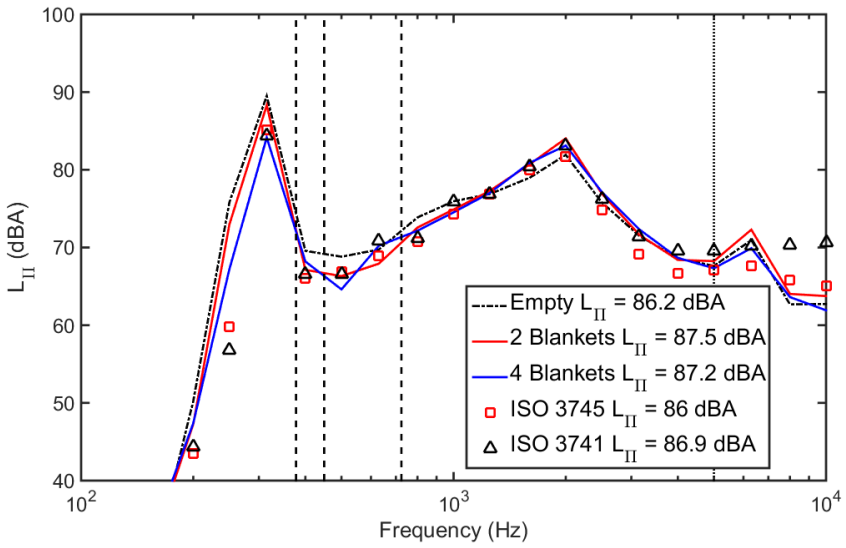

Fig. 4.20. The A-weighted sound power level curves of the blender measured in the VAC under the three different absorption conditions. The measurement quantity used was GED. The dashed lines represent the Schroeder frequency for each condition,with the highest being the empty condition and lowest being the four-blanket configuration. The upper dotted line represents the upper cut-off frequency of the energy density sensor. Results from ISO 3745 and ISO 3741 measurements are also overlaid for comparison.

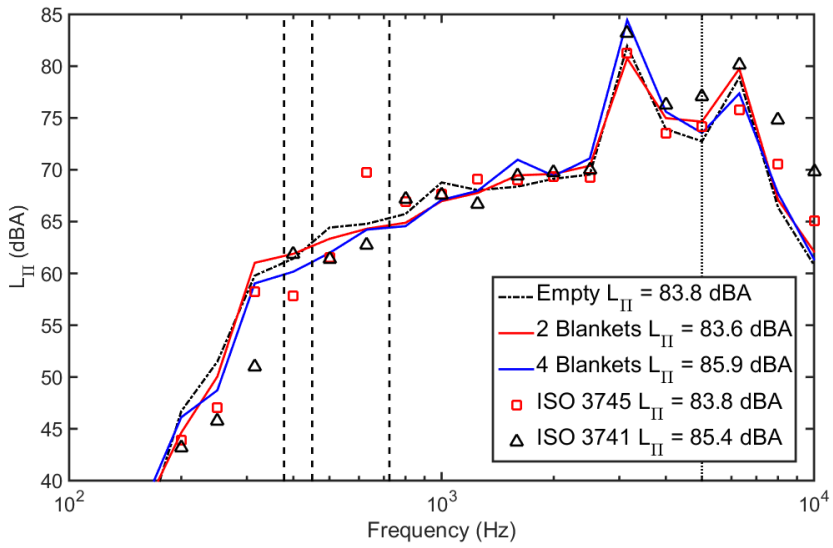

Fig. 4.21. The A-weighted sound power level curves of the vacuum measured in the VAC under the three different absorption conditions.

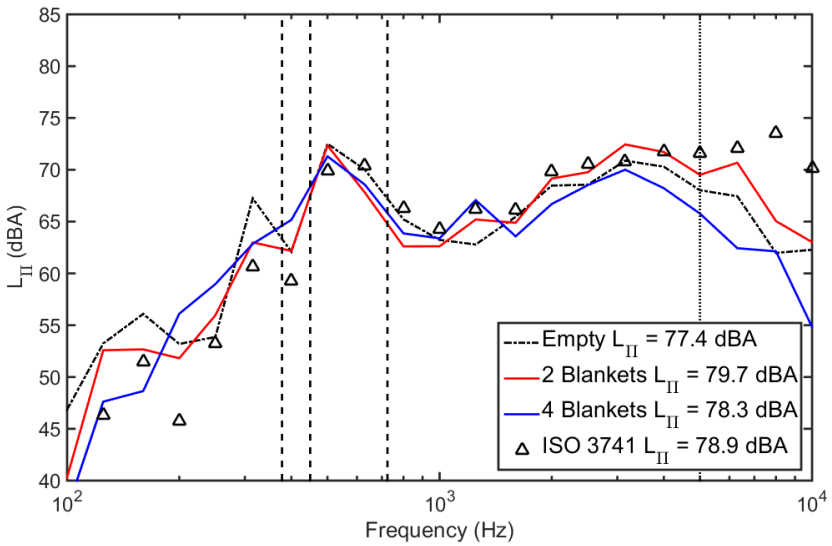

Fig. 4.22. The A-weighted sound power level curves of the belt and disc sander measured in the VAC under the three different absorption conditions.

All of the A-weighted levels were calculated for all frequencies above the Schroeder frequency and below the upper frequency limit of the probe. All measurements are within about 2 dBA of the ISO 3745 standard measurement. For the belt and disc sander, only the ISO 3741 sound power level was measured. This standard appears to be consistently higher than the ISO 3745 standard above about 3 kHz, which, if adjusted for, would lower the total sound power of the belt and disc sander, hence lowering the error of the two-point method. Table 4.3 shows the RMSE of the sources compared to ISO 3745 for the blender and vacuum and ISO 3741 for the belt sander. Most cases have an RMSE below 2 dB while one has an RMSE of 3.1 dB.

Table 4.2. The A-weighted sound power levels of the sources measured in the VAC under the three different absorption conditions. These values are compared to results using the ISO 3741 and 3745 standards.

Source	Sound Power Level (dBA)				
	Empty	Two Blankets	Four Blankets	ISO 3741	ISO 3745
Vacuum	83.8	83.6	85.9	85.5	83.8
Blender	86.2	87.5	87.2	87.1	86
Sander	77.4	79.7	78.3	80	--

Table 4.3. The RMSE of the sound power levels of the sources measured in the VAC under the three different absorption conditions. The ISO 3745 measurement was used as a reference value to calculate the RMSE for the vacuum and the blender. The ISO 3741 measurement was used for the sander.

Source	RMSE (dB)		
	Empty	Two Blankets	Four Blankets
Vacuum	1.9	1.6	1.6
Blender	1.3	1.2	1.2
Sander	2	1.9	3.1

Although the small room causes the lower cut-off frequency to be higher than one might desire, the results for sound power measurements are quite good. The smaller sources, especially, were quite accurate considering both the ISO 3745 and ISO 3741 standard, which have 95% uncertainty values between 1.2 and 1.4 dB for well-behaved sources.[4,5] Both the vacuum and the blender have considerable tonal components as well, which generally makes the sound power even more difficult to assess.[4]

The two-point measurements represent a practical method for engineers without the resources of an anechoic or reverberation chamber to measure the sound power level of a device with reasonable accuracy in a small, convenient room. Even with the use of blankets, the absorption of the VAC may have been more uniform than typical offices or other work environments. This, perhaps, contributes to the accuracy of the sound power level measurements, even though the room was quite small. The next sections explore measurements in rooms with conditions that were less uniform.

4.7.2 Laboratory Room

Room U186C in the BYU Eyring Science Center (Fig. 4.23) is a laboratory and equipment storage room. It is a moderate-sized room, with many different objects that provide scattering and absorption in a nonuniform fashion. The estimated volume of the room was 166 m^3 and the surface area was 191 m^2 (without accounting for objects in the room). The

Fig. 4.23. The two-point in situ method in room U186C of the Eyring Science Center on BYU campus. The reference directivity speaker and the belt sander are shown. This room is used for equipment storage and experiments.

frequency-averaged reverberation time was about 0.5 seconds, the Schroeder frequency was 110 Hz and the frequency-averaged critical distance was 1.05 m.

The sound power measurements of the belt and disc sander were measured with a few different positions using the two-point method (shown in Table 4.4). Only point measurements were made in this room. The low-frequency cutoff is set at 200 Hz because the noise floor in the room below 200 Hz was significant, especially considering that the output of the sander was very

Table 4.4. Measurement distances (in meters) for the two-point method measuring the sound power of the belt and disc sander in U186C.

Configurations	Reference Source		Sander	
	r_1	r_2	r_3	r_4
1	0.37	1.78	0.91	2.31
2	0.37	2.21	0.48	2.31
3	0.83	1.78	0.91	1.87
4	0.83	2.21	0.48	1.87

low in this spectral region. Figure 4.24 shows the sound power level measurements of the sander.

They show good agreement at all measurement points, with A-weighted sound power levels less than 2 dB from the ISO 3741 measurement for all configurations. Configuration 2 had the lowest error and also the measurement positions that were farthest from the critical distance. This suggests that it is beneficial for the positions to be well within the direct and reverberant fields, but near-field directivity of the source should be considered as a complication if r_1 is too close to the source.

The frequency-dependent room constant was also calculated according to Eq. (2.29) from the measured reverberation times in the room and the estimated volume and surface area. It must be stated that the calculation requires accurate estimations of the volume and surface area of a room, which is not likely in a room like U186C, with so many obstructive objects that complicate them. Figure 4.25 shows the logarithmic room constant measured by the two-point

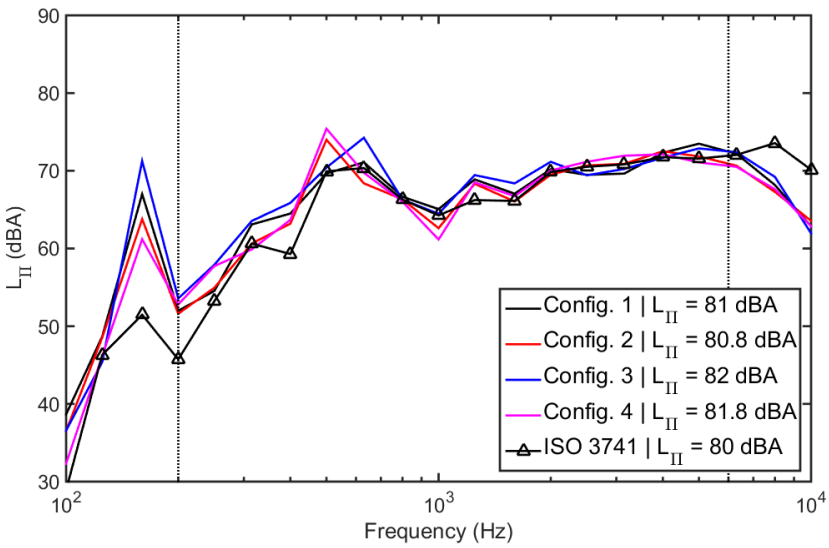

Fig. 4.24. The A-weighted sound power level of the belt sander measured in room U186C. The lower dashed line represents a background noise floor cutoff frequency while the upper dashed line represents the upper cutoff frequency of the energy density sensor.

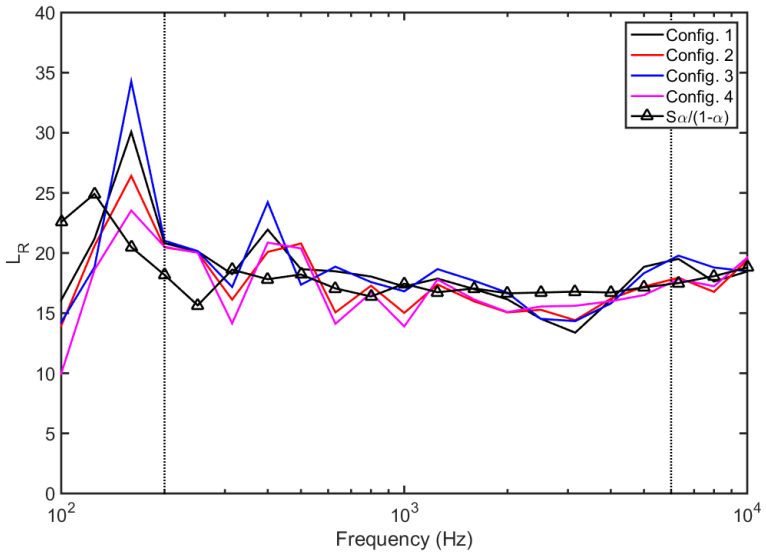

Fig. 4.25. The room constant level measured by the two-point in situ method in room U186C. The lower-frequency vertical dotted line represents a background noise floor cutoff frequency while the upper dotted line represents the upper usable frequency limit of the energy density sensor. The estimated room constant (triangles) was calculated from the measured reverberation time and the estimated volume and surface area of the room.

method, compared with the calculated room constant from the reverberation times and volume and surface area. The discrepancy is less above the 200 Hz background noise cutoff frequency.

4.7.3 Lecture Hall

Room C215 is a lecture hall in the Eyring Science Building at BYU. It has an estimated volume of 590 m^3, a surface area of 611 m^2, and a Schroeder frequency of approximately 80 Hz. The two-point measurement setup with the reference directivity loudspeaker is pictured in Fig. 4.26. Again, since the vacuum and blender were small sources, they were simply substituted in the same position as the reference source for sound power level measurements.

Fig. 4.26. The two-point in situ method in room C215 of the Eyring Science Center on the BYU campus. The reference directivity loudspeaker is shown.

This room was much larger than those described previously, so there was a lot of room to experiment with "manual" spatial averaging. This consisted of loosening the joints on the microphone stand and slowly moving the sensor back and forth and up and down (perpendicular to the measurement axis) while data was being measured and time averaged.[16] The results in Fig. 4.27 for the blender show that the best combination for overall sound power measurement seemed to involve a point measurement for the position near the source and a small spatial average far from the source. The small average comprised about a 0.09 m^2 total area average about the measurement position. Figure 4.28 shows similar results for the vacuum. The 300 Hz lower frequency cutoff in this case is due to considerable background noise compared to the signal at those frequencies. As done previously, the total sound power level was calculated between the lower and upper cutoff frequencies.

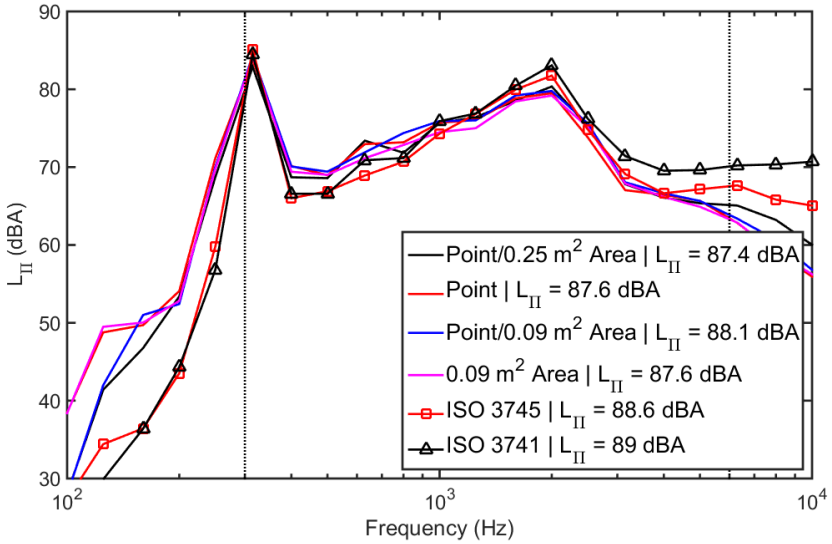

Fig. 4.27. The A-weighted sound power level of the blender measured in room C215. The lower frequency vertical dotted line represents a background noise floor cut-off frequency while the upper dotted line represents the upper frequency limit of the energy density sensor. The Point/0.25 m^2 Area text in the legend represents a point measurement at r_1 and a 0.25 m^2 perpendicular area measurement at r_2. The Point text in the legend represents a measurement where both r_1 and r_2 were point measurements. Similarly, the measurement with only 0.09 m^2 Area represents two perpendicular area measurements of the same size at r_1 and r_2.

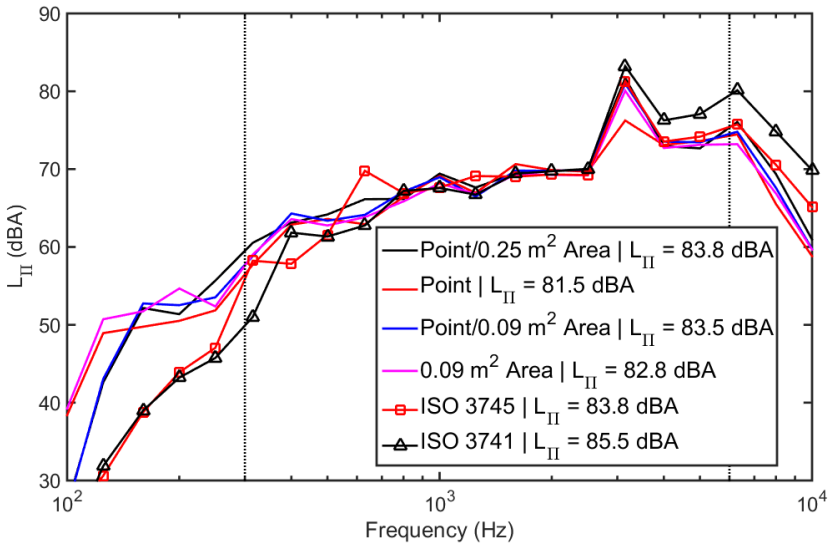

Fig. 4.28. The A-weighted sound power level of the vacuum measured in room C215.

The theoretical and measured room constants are presented in Fig. 4.29. The measured room constant is below the estimated value for the room constant over most frequencies. The latter comes from a reverberation time measurement and an estimate of the volume and surface area of the room. The volume and surface area of the room are difficult if not impossible to know exactly, which causes errors in the estimation. The two-point method uses a known directivity factor to measure the room constant rather than estimate it. This example shows that the sound power levels of two sources were measured accurately using an in situ measurement of the room constant, rather than estimating it. In cases such as these, where the volume and surface area are difficult to estimate, it may be more beneficial to simply measure the room constant in situ. Along these same lines, Cotana explained that the actual value of the room constant can be region dependent, based on the localized scattering and absorption in a room.[20-21] This could explain some of the discrepancy because the in situ room constant was measured in

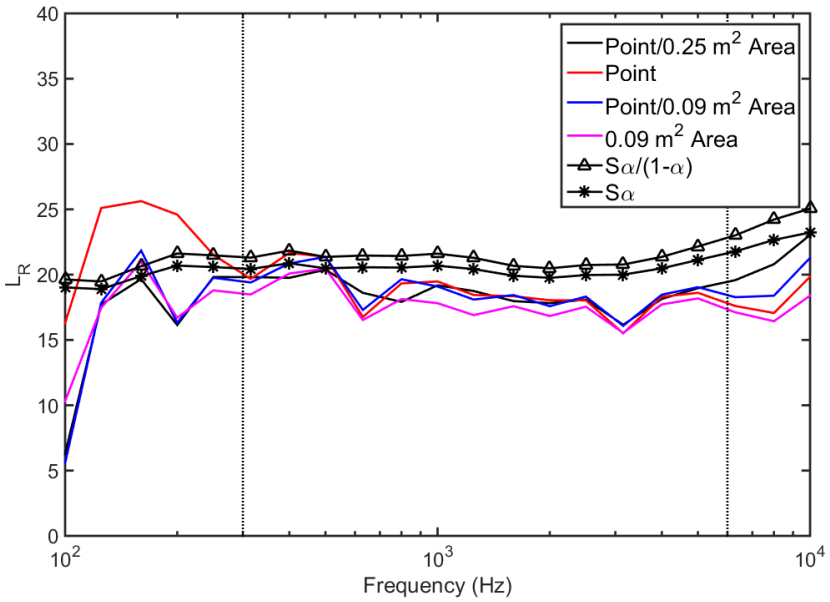

Fig. 4.29. The logarithmic room constant measured by the two-point in situ method in room C215. The lower frequency dashed line represents a background noise floor cutoff frequency while the upper frequency dashed line represents the upper cutoff frequency of the energy density sensor. The estimated room constant (triangle) is estimated from the reverberation time and the volume and surface area of the room.

one region of the room, whereas the room constant calculation was based on the reverberation times averaged from many positions in the room.

A possible source of error in the room constant measurements may result from the fact that the reverberant field in large rooms has been found to decay with increasing distance.[36-39] This reverberant field decay is not considered in the two-point method in its current form, so a room this large could lead to some error in the room constant measurement. Future research could explore the use of a reverberant field decay factor $\tau(r,k)$ in the room constant term of the modified Hopkins-Stryker as a function of distance and wavenumber:

$$\langle w_{G,\beta}\rangle_{t,s} = \frac{\langle \Pi \rangle_t}{2c}\left(\frac{\gamma(\theta_0,\phi_0)}{4\pi r^2}\left\{\beta + (1-\beta)\left[1+\frac{1}{(kr)^2}\right]\right\} + \frac{4}{\tau(r,k)R}\right). \tag{4.4}$$

4.8 Conclusions

Several experiments were performed to validate the two-point measurement theory from Ch. 2, and results from the numerical experiments from Ch. 3. The near-field correction was shown to be beneficial for a small dodecahedron source, greatly improving the in situ room constant calculation for GED at lower frequencies. The suggestion that one measurement position should be in the predominantly direct field and one should be in the predominantly reverberant field was also affirmed using the same source.

Spatial averaging improves both the sound power level measurement and the room constant measurements. The work in this chapter demonstrated that a simple and effective method of spatial averaging was to use a point measurement in the direct field region and a perpendicular spatial average in the reverberant field region. As discussed in Ch. 3, the simplest spatial average is a linear average, perpendicular to the axis of measurement.

The sound powers produced by three arbitrary sources were measured in three different environments using GED as the measurement quantity. The A-weighted sound power level was measured to within about 2 dBA of the ISO 3745 standard for most cases. Spatial averaging and a measurement position on either side of the critical distance improved the RMSE for more accurate measurements.

Chapter 5

Conclusions

The two-point in situ method using GED has proven to be a practical and effective method of measuring both the room constant and sound power of a source in nonideal semi-reverberant rooms. The RMSE relative to current ISO standard measurements for sound power was found experimentally to be between about 1 dB and 3.5 dB, depending on the source and room conditions.

This work has explored improvements to the two-point method. Local spatial averaging was studied both numerically and experimentally and found to improve the method. The optimal value of the GED weighting factor using the two-point method was found numerically. The best method of sensor placement was found both numerically and experimentally. A near-field correction for the two-point method was developed for a monopole. The room constant was measured using the two-point method. The results from this thesis showed improvements to room constant measurements when compared to earlier results of Marquez. These improvements resulted from spatial averaging of measurements, the optimal placement of sensors, near-field correction, as well as recognizing the importance of representing the room constant

logarithmically. The sound powers produced by three arbitrary sources were measured using the two-point method improvements with good results. Several insights were learned from this research and are summarized here:

1. The underlying assumptions of the Hopkins-Stryker equation require that measurements be taken in the direct far field of a source. This may be impossible for some rooms and sources, because the location of the critical distance requires one point of the two-point method to be in the direct near-field region of the source. However, for a point source, one can correct the amplitude for any GED value of β. The correction can also be used as a starting point to approximate the near-field effects of other sources.
2. With the near-field corrected version of the Hopkins-Stryker equation, the best GED weighting factor was found to be $\beta = 0.25$ for all points and frequencies above the Schroeder frequency, which is consistent with prior diffuse-field work.[15]
3. The best measurement sensor positions for the two-point method involve one well on either side of the critical distance. This ensures that the direct-field energy or the reverberant-field energy is dominant at each location.
4. Spatial averaging decreases the errors associated with room constant and sound power measurements. When using GED, the perpendicular linear or area average seem to have the most practical benefit. For both point measurements and spatially averaged measurements, GED is generally more accurate than PED. However, it was seen that a spatial average is more beneficial for PED than GED due to the higher spatial correlation of GED. The spatial average with the lowest error was a spatial average about 10% to 25% of the smallest room dimension. Care should be taken to ensure that the average size is smaller than the distance from the source to the central measurement location. If

the directivity of the source is likely to be complicated in the near field or change significantly over the averaging region, one can use a point measurement for the close measurement and a spatial average for the more distant measurement. The most accurate spatial average for the experiments was the area average, perpendicular to the axis from the source. The linear average perpendicular to the axis was also accurate and may be more practical in some applications.

5. As the nonuniformity of the room boundaries increases, the error in the room constant and sound power measurements increases as well. This is expected, as reverberant field theory relies on uniform boundaries or well distributed absorption to create a diffuse field. The GED performs better than PED under nonuniform conditions and seems to be robust, as long as the nonuniformity of the boundaries is not too extreme.
6. Several experiments were performed to validate the results from numerical experiments. The near-field correction was shown to be beneficial for a small dodecahedron loudspeaker, greatly improving the in situ room constant calculation for GED at low frequencies, i.e., involving the direct near field. The assertion that placing one measurement position in the direct field and one in the reverberant field was also validated using this loudspeaker.

The sources and rooms used in this research do not cover all the possibilities one might encounter using the two-point method. Future research could explore the use of the method on more varied sources and rooms in an attempt to characterize errors that might arise and establish the conditions for which the two-point method would not be recommended. An example of the two-point method underestimating the sound power level of a large distributed source is shown in Appendix D. This could be further explored to develop guidelines for larger and more

complicated sources. The three-point method described in Ch. 2 could possibly be helpful in identifying the acoustic center of large sources.

The environment that the source is in also presents limitations. Ambient noise can cause problems that must be addressed. The reverberant field assumption made for the Hopkins-Stryker equation also assumes that the spatially averaged reverberant field is constant throughout the room. Several examples in the literature show that this is not always the case for many rooms.[20-21,36-39] These references include potential methods for correcting reverberant field decay using the Hopkins-Stryker equation. It would be beneficial to explore more of these results to build in a feasible correction to the in situ room constant measurement method that accounts for these discrepancies.

The Hopkins-Stryker equation neglects the fact that the directivity factor of a source in the near field is radially dependent. If one point of the two-point method is in the direct near field of the source and the other is in the far field, along the same axis, the directivity factor at each points is not necessarily the same. Methods of accounting for this effect (such as near-field acoustical holography), both for the reference source and the DUT, would help eliminate some of the errors associated with the directivity assumptions. The author recommends that additional research in these and other areas be conducted to further enhance the methods discussed in this thesis.

References

[1]A. D. Pierce, *Acoustics: An Introduction to its Physical Principles and Applications* (Acoustical Society of America, New York, 1989), pp. 45, 162, 267-268, 270, 293.

[2]H. F. Hopkins and N. R. Stryker, "A proposed loudness-efficiency rating for loudspeakers and the determination of system power requirements for enclosures," Proc. IRE **36**, 315-335 (1948).

[3]E. C. Petersen, "An overview of standards for sound power determination," Application Note BO 0416, Bruel & Kjaer Instruments, Inc. (1994), available online at http://www.bksv.com/doc/BO0416.pdf (last viewed March 4, 2016).

[4]ISO 3741:2010. "Acoustics – Determination of sound power levels and sound energy levels of noise sources using sound pressure – Precision methods for reverberation test rooms" (International Organization for Standardization, Geneva, 2010).

[5]ISO 3745:2012. "Acoustics – Determination of sound power levels and sound energy levels of noise sources using sound pressure – Precision methods for anechoic rooms and hemianechoic rooms" (International Organization for Standardization, Geneva, 2012).

[6]H. Kuttruff, *Room Acoustics*, 5th ed. (Spon Press, New York, 2009), pp. 44, 55, 83, 86, 131.

[7]J. B. Moreland, "Measurement of sound absorption in rooms," J. Acoust. Soc. Am. **61**, 476-483 (1977).

[8]C. Ianniello, "Walk away method versus reverberation time method in determining the room constant," Applied Acoustics **14**, 83-92 (1980).

[9]R. Wells, "Apparatus noise measurement." Electrical Engineering **75**, 419-419 (1956).

[10]G. M. Diehl, *Machinery Acoustics*. (Wiley, 1974).

[11]ASTM Standard E33, 2010, "Standard Test Method for Field Measurement of Sound Power Level by the Two-Surface Method" (ASTM International, West Conshohocken, PA, 2010).

[12]P. G. Terrell, W. J. Hanson, and M. D. Ramsey, "Predicting noise reduction from absorptive treatments in industrial spaces: Alternatives to the 'Sabine' method," Am. Ind. Hyg. Assoc. J. **44**, 809-813 (1983).

[13]J. A. Moryl, "A study of acoustic energy density in a reverberation room," Ph.D. thesis, The University of Texas at Austin (1987).

[14]B. Xu, S. D. Sommerfeldt, and T. W. Leishman, "Generalized acoustic energy density," J. Acoust. Soc. Am. **130**, 1370-1380 (2011).

[15]D. Marquez, "Estimating the Acoustic Power of Sources in Nonideal Enclosures Using Generalized Acoustic Energy Density," M.S. Thesis, Brigham Young University, 2014, available online at http://scholarsarchive.byu.edu/etd/3977/ (last viewed March 4, 2016).

[16]L. L. Beranek, *Acoustics* (McGraw-Hill, New York, 1954), pp. 109, 298-324.

[17]ISO 9613-1:1993. "Acoustics –Attenuation of sound during propagation outdoors – Part 1:Calculation of the absorption of sound by the atmosphere " (International Organization for Standardization, Geneva, 1993).

[18]M. Hodgson, "Experimental evaluation of the accuracy of the Sabine and Eyring theories in the case of non-low surface absorption,"J. Acoust. Soc. Am. **94**, 835-840 (1993).

[19]R. J. Wells and F. M. Wiener, "On the determination of the acoustic power of a source of sound in semi-reverberant spaces," NOISE Control **7**, 21-29 (Jan./Feb, 1961).

[20]J. Thompson, L. Mitchell, and C. Hurst, "A modified room acoustics approach to determine sound pressure levels in irregularly proportioned factory spaces," Proc. Inter-Noise **76**, Washington DC, 1976, pp. 465-468.

[21]F. Cotana, "An improved room acoustic model." Appl. Acoust. **61**, 1-25 (2000).

[22]B. Xu, and S. D. Sommerfeldt, "A hybrid modal analysis for enclosed sound fields," J. Acoust. Soc. Am. **128**, 2857-2867 (2010).

[23]D. Nutter, T. W. Leishman, S. D. Sommerfeldt, and J. D. Blotter, "Measurement of sound power and absorption in reverberation chambers using energy density," J. Acoust. Soc. Am. **121**, 2700-2710 (2007).

[24]J. Allen, and D. A. Berkley, "Image method for efficiently simulating small-room acoustics," J. Acoust. Soc. Am. **65**, 943-950 (1979).

[25]E. A. Lehmann and A. M. Johansson, "Prediction of energy decay in room impulse responses simulated with an image-source model," J. Acoust. Soc. Am. **124**, 269-277 (2008).

[26]G.R.A.S. Sound & Vibration, "Vector Intensity Probe Type 50VI-1 Instruction Manual," available online at http://www.gras.dk/media/docs/files/items/m/a/man_50VI-1.pdf (last viewed March 4, 2016).

[27]J.-C. Pascal, and J.-F. Li, "A systematic method to obtain 3D finite-difference formulations for acoustic intensity and other energy quantities," J. Sound and Vib. **310**, 1093-1111 (2008).

[28]ISO 354:2003. "Acoustics – Measurement of sound absorption in a reverberation room" (International Organization for Standardization, Geneva, 2003).

[29]Y. Naka, A. A. Oberai, and G. Shinn-Cunningham, "Acoustic eigenvalues of rectangular rooms with arbitrary wall impedances using the interval Newton/generalized bisection method," J. Acoust. Soc. Am. **118**, 3662-3671 (2005).

[30]J. Borish, "Extension of the image model to arbitrary polyhedra," J. Acoust. Soc. Am. **75**, 1827-1836 (1984).

[31]S. Nielsen – Seismic Waves and Sources (2008) available online at ftp://ftp.ingv.it/pub/stefan.nielsen/ROSE_CLASS/NOTES/s07.pdf (last viewed March 4, 2016).

[32]P. Peterson, "Simulating the response of multiple microphones to a single acoustic source in a reverberant room," J. Acoust. Soc. Am. **80**, 1527-1529 (1986).

[33]M. R. Schroeder, "Integrated-impulse method measuring sound decay without using impulses," J. Acoust. Soc. Am. **66**, 497-500 (1979).

[34]T. W. Leishman, S. Rollins, H. M. Smith, "An experimental evaluation of regular polyhedron loudspeakers as omnidirectional sources of sound," J. Acoust. Soc. Am. **120**, 1411-1422 (2006).

[35]P. M. Morse and K. U. Ingard, *Theoretical Acoustics*, (Princeton University Press, New Jersey,1968) pp. 320.

[36]M. Long, *Architectural Acoustics*, 2nd ed. (Academic Press, Missouri, 2014) pp. 338-341.

[37]M. Kleiner and J. Tichy, *Acoustics and Design of Small Rooms* (GBR: CRC Press, London, 2014), pp. 86-90.

[38]D. Davis, E. Patronis, P. Brown, *Sound System Engineering*, 4th ed. (Focal Press, Massachusetts, 2013), Ch. 12.

[39]M. Hodgson, "Experimental evaluation of simplified models for predicting noise levels in industrial workrooms," J. Acoust. Soc. Am. **103**, 1933-1939 (1998).

[40]B. Xie, *Head-Related Transfer Function and Virtual Auditory Display*, 2nd ed. (J. Ross Publishing, Plantation, FL, 2013), pp. 144.

[41]ISO 3741:2010. "Acoustics – Determination of sound power levels and sound energy levels of noise sources using sound pressure – Engineering/survey methods for use in situ in a reverberant environment" (International Organization for Standardization, Geneva, 2010).

[42]AFMG Technologies GmbH EASE™ Software available online at http://ease.afmg.eu/ (last viewed March 4, 2016).

Appendix A

Numerical Models

Acoustic field modeling is useful for predicting pressure or particle velocity values at certain positions in a room. There are several advantages of using modal analysis (MA) and image source (IS) methods for this purpose. The first is the simplicity of the models. They are based on the acoustic wave equation and describe the steady-state response of the room. They are relatively simple to code using a mathematical program such as MATLAB and, depending on accuracy, may not be computationally expensive. Another advantage is that the foundation for each method is generally understood and accepted in the acoustics community.

The following derivations are limited to a room with a "shoebox" geometry—a rectangular parallelepiped—although both methods may be generalized to other geometries. The room has dimensions $L_x \times L_y \times L_z$, a volume V, and a surface area S. The origin of the room is in the corner, as shown in Fig. (A.1). Both methods incorporate distinct assumptions that limit their accuracy and scope. These assumptions will be addressed in the derivations.

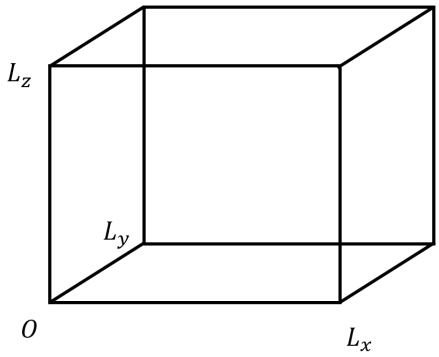

Fig. A.1. A rectangular parallelepiped with the origin (O) in the corner.

A.1 Modal Analysis

The modal solution is a linear combination of modal eigenfunctions

$$\hat{p} = \sum_n a_n \Psi_n, \tag{A.1}$$

where a_n are the modal amplitudes and the eigenfunctions satisfy the homogeneous Helmholtz equation

$$\nabla^2 \Psi_n + k_n^2 \Psi_n = 0 \tag{A.2}$$

and the boundary-value problem, where k_n^2 represents the eigenvalues. The inhomogeneous wave equation for a point source at a single position r_0 in a room is

$$\nabla^2 p - \frac{1}{c^2}\frac{\partial^2 p}{\partial t^2} = -j\rho_0 ckQ_s(t)\delta(\vec{r} - \vec{r}_0). \tag{A.3}$$

The term on the right hand side represents the point source, where Q_s is the source strength.[1]

Assuming the solution is time harmonic, or taking the Fourier transform of Eq. (A.3), gives the inhomogeneous Helmholtz equation follows as

$$\nabla^2 \hat{p} + k^2 \hat{p} = -j\rho_0 ck\hat{Q}_s \delta(\vec{r} - \vec{r}_0), \tag{A.4}$$

where the circumflex marks denote complex variables in the frequency domain (ω). To solve for the modal amplitudes and eigenfunctions in Eq. (A.1), one can first multiply Eq. (A.4) by the conjugate of the eigenfunction Ψ_m^*, where the subscript m represent the mth mode:

$$\Psi_m^* \nabla^2 \hat{p} + k^2 \Psi_m^* \hat{p} = -j\rho_0 ck \hat{Q}_s \delta(\vec{r} - \vec{r}_0)\Psi_m^*. \tag{A.5}$$

Adding zero to the quantity $\Psi_m^* \nabla^2 \hat{p}$,

$$\Psi_m^* \nabla^2 \hat{p} = \Psi_m^* \nabla^2 \hat{p} + (\hat{p}\nabla^2 \Psi_m^* - \hat{p}\nabla^2 \Psi_m^*) = \hat{p}\nabla^2 \Psi_m^* + \nabla \cdot (\Psi_\mathrm{m}^* \nabla \hat{p} - \hat{p}\nabla \Psi_m^*), \tag{A.6}$$

Eq. (A.5) becomes

$$\hat{p}\nabla^2 \Psi_m^* + \nabla \cdot (\Psi_\mathrm{m}^* \nabla \hat{p} - \hat{p}\nabla \Psi_m^*) + k^2 \Psi_m^* \hat{p} = -j\rho_0 ck \hat{Q}_s \delta(\vec{r} - \vec{r}_0)\Psi_m^*. \tag{A.7}$$

Since the eigenfunction satisfies the Helmholtz equation [see Eq. (A.2)],

$$(k^2 - k_m^2)\hat{p}\Psi_m^* + \nabla \cdot (\Psi_\mathrm{m}^* \nabla \hat{p} - \hat{p}\nabla \Psi_m^*) = -j\rho_0 ck \hat{Q}_s \delta(\vec{r} - \vec{r}_0)\Psi_m^*. \tag{A.8}$$

Integrating over the entire volume, using Gauss' theorem, and applying the sifting property of the Dirac delta function, this becomes

$$\iiint_V (k^2 - k_m^2)\hat{p}\Psi_m^* dV + \iint_S (\Psi_\mathrm{m}^* \nabla \hat{p} - \hat{p}\nabla \Psi_m^*) \cdot \mathrm{n}\, dS = -j\rho_0 ck \hat{Q}_s \Psi_m^*(\vec{r}_0), \tag{A.9}$$

which matches the second line of Eq. (A.8) in Xu.[17]

We can simplify the result further by using what we know about the impedance boundary conditions for (presumably) locally reacting surfaces. The normal specific acoustic wall impedance Z_S is the pressure over the normal velocity component $\hat{u}_n$ into the surface S:

$$Z_S = \left(\frac{\hat{p}}{\hat{u}_n}\right)_S. \tag{A.10}$$

The latter is determined from the time-harmonic Euler's equation

$$\hat{u}_n = -\frac{1}{j\omega\rho_0}\frac{\partial\hat{p}}{\partial n} = -\frac{1}{j\omega\rho_0}\nabla\hat{p}\cdot\vec{n}, \tag{A.11}$$

where $\vec{n}$ is the unit vector *into* the surface of the wall. It follows that

$$\hat{p} = -\frac{Z_S}{j\omega\rho_0}\frac{\partial\hat{p}}{\partial n}. \tag{A.12}$$

Using the normalized, dimensionless specific acoustic impedance

$$\zeta = \frac{Z_S}{\rho_0 c}, \tag{A.13}$$

the relationship can be rewritten as

$$\zeta\frac{\partial\hat{p}}{\partial\vec{n}} = -jk\hat{p} \tag{A.14}$$

or

$$\frac{\partial\hat{p}}{\partial\vec{n}} = \gamma\hat{p}, \tag{A.15}$$

where

$$\gamma = -jk\left(\frac{\rho_0 c}{Z_S}\right) = -\frac{jk}{\zeta} \tag{A.16}$$

is proportional to the dimensionless specific acoustic admittance and will be called the modified specific acoustic admittance.* The boundary condition for the eigenfunction is likewise

$$\left(\frac{\partial\Psi_n}{\partial\vec{n}}\right)_S = \gamma'\Psi_n. \tag{A.17}$$

* Traditionally, the normalized specific acoustic admittance is written as $\beta = \frac{\rho_0 c}{\hat{Z}_S}$. The modified specific acoustic admittance includes the extra *jk* modifier on the normalized specific acoustic admittance, as in Eq. (A.16).

The value of γ' is typically set to zero for classical modal analysis, and will be further defined in section A.3.

Using Eqs. (A.15) and (A.17) we can write Eq. (A.9) as

$$\iiint_V (k^2 - k_m^2)\hat{p}\Psi_m^* dV + \iint_S (\gamma - \gamma')\hat{p}\Psi_m^* dS = -j\rho_0 ck\hat{Q}_S\Psi_m^*(\vec{r}_0). \quad \text{(A.18)}$$

We then expand the pressure as a linear combination of modal amplitudes and eigenfunctions as in Eq. (A.1) and interchange summation and integration to yield

$$\sum_n a_n \iiint_V (k^2 - k_m^2)\Psi_n\Psi_m^* \, dV + \sum_n a_n \iint_S (\gamma - \gamma')\Psi_n\Psi_m^* dS = -j\rho_0 ck\hat{Q}_S\Psi_m^*(\vec{r}_0). \quad \text{(A.19)}$$

Here the index n represents one mode, which is a combination of all the index terms, $n = (n_x, n_y, n_z)$. We can simplify these equations and write them in matrix form to solve for a_n very efficiently. We begin by making the substitutions

$$C_{mn} = \iiint_V \Psi_n\Psi_m^* \, dV = \Lambda_{mn}\delta_{mn} \quad \text{(A.20)}$$

and

$$D_{mn} = \iint_S (\gamma - \gamma')\Psi_n\Psi_m^* dS, \quad \text{(A.21)}$$

where Λ_{mn} is a normalization constant and δ_{mn} is the Kronecker delta function. Equation (A.19) can then be rewritten as

$$\sum_n a_n[(k^2 - k_m^2)C_{mn} + D_{mn}] = -j\rho_0 ck\hat{Q}_S\Psi_m^*(\vec{r}_0), \quad \text{(A.22)}$$

or in matrix form

$$\begin{bmatrix} (k^2 - k_1^2)C_{11} + D_{11} & D_{12} & \cdots \\ D_{21} & (k^2 - k_2^2)C_{22} + D_{22} & \cdots \\ \vdots & \vdots & \ddots \end{bmatrix} \cdot \begin{bmatrix} a_1 \\ a_2 \\ \vdots \end{bmatrix} = \begin{bmatrix} -j\rho_0 ck\hat{Q}_S \Psi_1^*(\vec{r}_0) \\ -j\rho_0 ck\hat{Q}_S \Psi_2^*(\vec{r}_0) \\ \vdots \end{bmatrix}. \tag{A.23}$$

The modal amplitudes a_n can be solved quite simply from Eq. (A.23) and the pressure at any point in the room can be calculated using Eq. (A.1).

A.2 Eigenfunctions

The eigenfunction from Eq. (A.1) can be determined using the separation of variables technique. We begin by assuming the eigenfunction is a product of three spatially independent functions:

$$\Psi = \Psi_x(x)\Psi_y(y)\Psi_z(z). \tag{A.24}$$

From Eq. (A.2) we see that

$$\frac{\Psi_x''}{\Psi_x} + \frac{\Psi_y''}{\Psi_y} + \frac{\Psi_z''}{\Psi_z} + k^2 = 0. \tag{A.25}$$

Each term can subsequently be set equal to a constant:

$$\frac{\Psi_x''}{\Psi_x} = -k_x^2; \quad \frac{\Psi_y''}{\Psi_y} = -k_y^2; \quad \frac{\Psi_z''}{\Psi_z} = -k_z^2. \tag{A.26}$$

Solving for Ψ_i in Eq. (A.26) yields

$$\begin{aligned} \Psi_x &= A\cos(k_x x) + B\sin(k_x x), \\ \Psi_y &= C\cos(k_y y) + D\sin(k_y y), \\ \Psi_z &= E\cos(k_z z) + F\sin(k_z z), \end{aligned} \tag{A.27}$$

so that Eq. (A.24) becomes

$$\Psi = [A\cos(k_x x) + B\sin(k_x x)]\left[C\cos(k_y y) + D\sin(k_y y)\right][E\cos(k_z z) + F\sin(k_z z)]. \tag{A.28}$$

Using the boundary conditions from Eq. (A.17) in the x direction at the $x = 0$ wall and solving for the constant B yields

$$\frac{-k_x A\sin(k_x 0) + k_x B\cos(k_x 0)}{A\cos(k_x 0) + B\sin(k_x 0)} = \frac{k_x B}{A} = -\gamma'_{x0},$$

$$B = -\frac{\gamma'_{x0} A}{k_x}. \tag{A.29}$$

The modified specific acoustic admittance γ' is negative because the negative x direction is into the wall. We can now write Eq. (A.27) as

$$\Psi_x = A\left[\cos(k_x x) - \frac{\gamma'_{x0}}{k_x}\sin(k_x x)\right]. \tag{A.30}$$

Now using the $x = L_x$ boundary condition, we can write

$$\frac{-A[k_x\sin(k_x L_x) + \gamma'_{x0}\cos(k_x L_x)]}{A\left[\cos(k_x L_x) - \frac{\gamma'_{x0}}{k_x}\sin(k_x L_x)\right]} = \gamma'_{xL}, \tag{A.31}$$

which simplifies to the transcendental equation

$$\tan(k_x L_x) = \frac{(\gamma'_{x0} + \gamma'_{xL})k_x}{\gamma'_{x0}\gamma'_{xL} - k_x^2}. \tag{A.32}$$

The same process yields similar equations in the y and z directions:

$$\tan(k_y L_y) = \frac{(\gamma'_{y0} + \gamma'_{yL})k_y}{\gamma'_{y0}\gamma'_{yL} - k_y^2} \tag{A.33}$$

and

$$\tan(k_z L_z) = \frac{(\gamma'_{z0} + \gamma'_{zL})k_z}{\gamma'_{z0}\gamma'_{zL} - k_z^2}. \tag{A.34}$$

By assuming that parallel walls have the same admittance, we may further reduce Eq. (A.32) to

$$k_x \tan\left(\frac{k_x L_x}{2}\right) = -\gamma_x' \tag{A.35}$$

or

$$k_x \cot\left(\frac{k_x L_x}{2}\right) = \gamma_x', \tag{A.36}$$

with similar results in the y and z directions. The eigenvalues k_x, k_y, k_z can be solved numerically by using the interval Newton/generalized bisection (INGB) method.[29]

In summary, to solve for the pressure in the room we use a linear combination of modal eigenfunctions, where the modal amplitudes a_n are solved using Eq. (A.23), the eigenvalues from Eqs. (A.32) through (A.34), and the eigenfunctions from Eq. (A.28).

A.3 Boundary Conditions

Up to this point, we have derived the equations in the most general terms, making very few assumptions. We now need to decide how to treat the modified specific acoustic admittance γ' for the eigenvalue boundary condition in Eq. (A.17). The following sections discuss different methods and their benefits and drawbacks.

A.3.1 Exact Modal Analysis

The actual Robin boundary condition is given in Eq. (A.15), with the modified normalized specific acoustic admittance γ given by Eq. (A.16). To match our boundary conditions exactly we would set $\gamma' = \gamma$. This is known as the exact modal analysis (EMA) method, giving the advantage of eigenfunctions that satisfy the exact boundary conditions. This condition also makes the square matrix in Eq. (A.23) sparse (as $D_{mn} = 0$ always) so the modes are uncoupled. The disadvantage of EMA is that γ' is complex, which means that the

eigenvalues must be solved numerically in the complex domain, which can be computationally expensive.

A.3.2. Classical Modal Analysis (Large Impedance Approximation)

Another option for γ' is to say that the admittance of the boundary is so small that it is effectively zero, making $\gamma' = 0$. This classical modal analysis (CMA) approach is the derivation that Pierce outlines[1] and will be briefly explained here. With $\gamma' = 0$, Eq. (A.28) becomes

$$\Psi = \cos(k_x x)\cos(k_y y)\cos(k_z z). \tag{A.37}$$

We can solve for the eigenvalues by substituting $\gamma' = 0$ into Eq. (A.32):

$$\tan(k_x L_x) = 0, \tag{A.38}$$

which leads to the allowed values

$$k_{x_{n_x}} = \frac{n_x \pi}{L_x}, \tag{A.39}$$

with

$$n_x = 0,1,2,\ldots \tag{A.40}$$

For the *y* and *z* directions, n_y and n_z are also nonnegative integers:

$$k_{y_{n_y}} = \frac{n_y \pi}{L_y};\ n_y = 0,1,2,\ldots \tag{A.41}$$

and

$$k_{z_{n_z}} = \frac{n_z \pi}{L_z};\ n_z = 0,1,2,\ldots \tag{A.42}$$

For computational purposes, the indices n_x, n_y, n_z must be truncated to a finite number of modes. If the impedance of the walls is sufficiently large, we may assume that the $m \neq n$ terms in Eq. (A.21) are negligible and set them to zero such that

$$D_{nn} = \iint_S \gamma \Psi_n^2 dS. \tag{A.43}$$

The normalization constant from Eq. (A.20) can be written as

$$\Lambda_n = \frac{V}{\epsilon_{n_x}\epsilon_{n_y}\epsilon_{n_z}}, \tag{A.44}$$

where

$$\epsilon_i = \begin{cases} 1; & i = 0 \\ 2; & i \neq 0 \end{cases}. \tag{A.45}$$

With these assumptions, we can rewrite Eq. (A.22) for a single term and then solve for the modal amplitudes a_n such that

$$a_n = -\frac{j\rho_0 ck\hat{Q}_s \Psi_n(\vec{r}_0)}{\Lambda_n(k^2 - k_n^2) - D_{nn}}. \tag{A.46}$$

The pressure can then be written using Eq. (A.1) as

$$\hat{p} = -j\rho_0 ck\hat{Q}_s \sum_n \frac{\Psi_n(\vec{r}_0)\Psi_n(\vec{r})}{\Lambda_n(k^2 - k_n^2) - jk\iint_S \Psi_n^2 \frac{\rho_0 c}{Z_S} dS}. \tag{A.47}$$

A.3.3 Modified Modal Analysis

So far we have discussed the two extremes for γ' that we may use. The EMA approach uses the actual wall admittance while the CMA approach assumes that the walls are extremely rigid or that the admittance is negligible for the eigenfunction boundary. While EMA is difficult to solve and CMA does not match the actual boundary conditions, modified modal analysis (MMA) attempts to bridge the gap between the two methods by setting $\gamma' = Re\{\gamma\}$. This keeps the true boundary condition partially satisfied, and ensures that the eigenvalue root search is more efficient than that of EMA because it is not in the complex domain.

A.3.4 Hybrid Modal Analysis

While the above methods provide a complete solution to the wave equation in the enclosure—as long as the boundary conditions are chosen appropriately—the solution requires many eigenvalues to converge to a solution in the region near the point source. This weakness may be overcome by adding the free-field Green's function for a point source to Eq. (A.1), providing a direct-field and reverberant-field term in the solution:

$$\hat{p} = \frac{j\rho_o ck\hat{Q}_s}{4\pi}[G(\vec{r}|\vec{r}_0) + F(\vec{r})], \tag{A.48}$$

where $G(\vec{r}|\vec{r}_0)$ is the free-field Green's function,

$$G(\vec{r}|\vec{r}_0) = \frac{e^{-jk\cdot(\vec{r}-\vec{r}_0)}}{|\vec{r}-\vec{r}_0|}, \tag{A.49}$$

and $F(r)$ is the reverberant field term[1,35]

$$F(\vec{r}) = \sum b_n \Psi_n. \tag{A.50}$$

Using Eqs. (A.48) and (A.49) in Eq. (A.18), and employing the sifting property of the Dirac delta function on the right-hand side [see Eqs. (A.8) and (A.9)] yields

$$\begin{aligned} &\iiint_V (k^2 - k_m^2)\frac{j\rho_o ck\hat{Q}_s}{4\pi}(G + \sum_n b_n\Psi_n)\Psi_m^* dV \\ &\quad + \iint_S (\gamma - \gamma')\frac{j\rho_o ck\hat{Q}_s}{4\pi}(G + \sum_n b_n\Psi_n)\Psi_m^* dS \\ &\quad = \iiint_V -j\rho_0 ck\hat{Q}_S\delta(\vec{r}-\vec{r}_0)\Psi_m^*(\vec{r}_0)\, dV. \end{aligned} \tag{A.51}$$

Putting all the b_n terms on one side and dividing through by $j\rho_0 ck\hat{Q}_s/4\pi$ leads to the expression

$$\sum_n b_n (k^2 - k_m^2) \iiint_V \Psi_m^* \Psi_n dV + \sum_n b_n \iint_S (\gamma - \gamma') \Psi_m^* \Psi_n dS$$

$$= - \iiint_V (k^2 - k_m^2) G \Psi_m^* dV - \iint_S (\gamma - \gamma') G \Psi_m^* dS \qquad \text{(A.52)}$$

$$- \iiint_V 4\pi\delta(\vec{r} - \vec{r}_0) \Psi_m^* \, dV.$$

The left hand side of this equation is formally the same as the left-hand side of Eq. (A.22), so from here we concentrate on the right-hand side of Eq. (A.52). Grouping the terms within a single volume integral, we can write the right hand side as

$$\ldots = - \iint_S (\gamma - \gamma') G \Psi_m^* dS - \iiint_V \{[k^2 G + 4\pi\delta(\vec{r} - \vec{r}_0)] - k_m^2 G\} \Psi_m^* \, dV. \qquad \text{(A.53)}$$

Because the Green's function is a solution to the inhomogeneous Helmholtz equation [Eq. (A.4)] for unit monopole amplitude or $\hat{Q}_s = -j4\pi/\rho_0 ck$, we can rewrite $4\pi\delta(\vec{r} - \vec{r}_0) = -\nabla^2 G - k^2 G$ in the volume integral, such that

$$\ldots = - \iint_S (\gamma - \gamma') G \Psi_m^* dS - \iiint_V [-\nabla^2 G - k_m^2 G] \Psi_m^* \, dV. \qquad \text{(A.54)}$$

Distributing the eigenfunction inside the volume integral and using Eq. (A.2), we have

$$\ldots = - \iint_S (\gamma - \gamma') G \Psi_m^* dS - \iiint_V [-\Psi_m^* \nabla^2 G + G \nabla^2 \Psi_m^*] \, dV. \qquad \text{(A.55)}$$

Using Green's second identity for the volume integral then yields

$$\ldots = - \iint_S (\gamma - \gamma') G \Psi_m^* dS - \iint_S [G \nabla \Psi_m^* - \Psi_m^* \nabla G] \cdot \vec{n} \, dS. \qquad \text{(A.56)}$$

The surface integrals can be combined. We can also use Eq. (A.17) for the gradient of the eigenfunction, giving

$$\ldots = -\iint_S [(\gamma - \gamma')G\Psi_m^* + G\gamma'\Psi_m^* - \Psi_m^*\nabla G \cdot \vec{n}]dS \tag{A.57}$$

or

$$\ldots = -\iint_S \left[\Psi_m^*\left(\gamma G - \frac{\partial G}{\partial \vec{n}}\right)\right]dS, \tag{A.58}$$

which matches the solution from Xu and Sommerfeldt.[22] The entire equation for the modal amplitudes after including the free-field Green's function in the solution is similar to Eq. (A.22), with a significant change to the right-hand side:

$$\sum_n b_n[(k^2 - k_m^2)C_{mn} + D_{mn}] = -\iint_S \left[\Psi_m^*\left(\gamma G - \frac{\partial G}{\partial n}\right)\right]dS. \tag{A.61}$$

The solutions are more complicated due to the surface integral, but they may be evaluated numerically. The sound pressure then results from Eq. (A.48) by substituting the b_n values into Eq. (A.50).

Xu and Sommerfeldt show that this hybrid method converges with fewer modes in the summation than the standard formulation. This method can be used with any method mentioned previously (EMA, CMA, MMA), but is most effective when used in conjunction with MMA because the convergence rate improves while the boundary conditions are still partially met. This hybrid modified modal analysis method (HMMA) is the approach used in this thesis for simulations.

A.4 Convergence

A.4.1 Truncating Summation Terms

In theory, the number of modes to include in the summation is infinite. Since this cannot be realized in practice, a method of determining how many modes should be used is critical. As

can be noted in the denominator of Eq. (A.47), as the eigenvalue or modal wavenumber k_m approaches the acoustic wavenumber k, the modal amplitude becomes large. When the modal wavenumber is far from the acoustic wavenumber, the modal amplitude will become negligible. This allows us to define a modal width k_w that defines the range of modes to sum over.

Pierce explains through a series of approximations that the imaginary part of Eq. (A.47) can be reduced to $ikS\bar{\alpha}/4V$.[1,6] From this approximation, an associated half-energy bandwidth

$$k_{BW} = \frac{S\bar{\alpha}}{4V}, \tag{A.62}$$

can be defined in terms of wavenumber.[1,6] We can then define a number of bandwidths N_{BW} to determine limits for the number of eigenvalues to sum over.[23] The modal width is then defined as $k_w = N_{BW}k_{BW}$. The eigenvalues included in the summation are the values between $k \pm k_w$. This allows for quicker calculations by neglecting all of the modes with negligible amplitudes that exist outside the modal width. The approach is illustrated in Fig. A.2. The modal amplitudes for a room with an average absorption coefficient $\bar{\alpha} = 0.5$ and excited at a frequency of 500 Hz are normalized to the maximum value and plotted as a function of modal wavenumber. The vertical dashed red lines represent the cutoff wavenumbers around the resonance; modal amplitudes outside the wavenumbers are not included in the summation. The judicious use of limited numbers of summation terms produces a significant savings in computation time, while still enabling reasonable solutions.

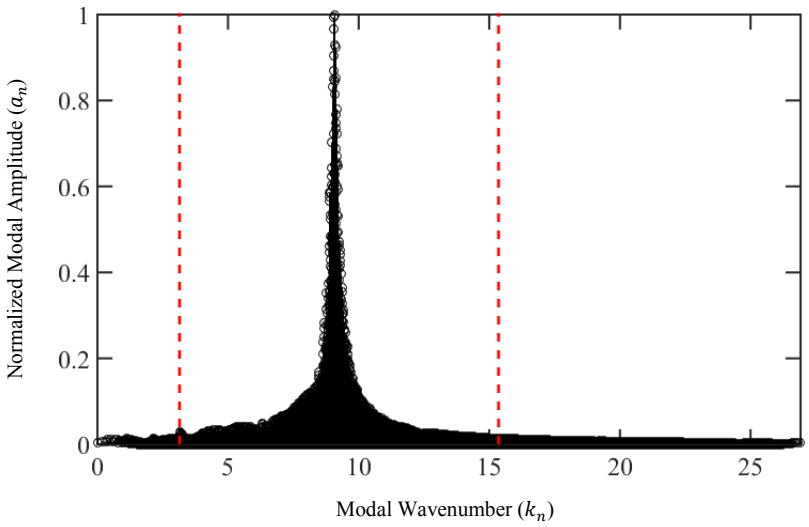

Fig. A.2. The normalized modal amplitudes of a room with dimensions $(L_x,\ L_y,\ L_z) = (10, 16, 3)$, an $\bar{\alpha} = 0.5$, and a 500 Hz excitation are plotted as a function of modal wavenumber. Anything outside of the red dashed lines is not included in the modal summation. The number of bandwidths was $N_{BW} = 50$ for this case. The distance between the two dashed lines is $2k_w$.

A.4.2 Classical Modal Analysis and Hybrid Modified Modal Analysis

As discussed earlier, the HMMA overcomes the CMA weakness of poor convergence near the point source for the traditional method. Farther from the source, the two are nearly identical for low absorption but begin to diverge as absorption increases. These effects are seen in Fig. A.3 where the PED for two different uniform absorptions ($\bar{\alpha} = 0.01$ and $\bar{\alpha} = 0.1$) are plotted at different distances from a monopole along a common axis. The HMMA method for a single modal width is compared to the CMA method for three increasing modal widths. The response of the same point source radiating into free-space is also plotted for comparison. As more eigenvalues are included in the summation (larger modal width) the CMA method converges to the HMMA method and the free-field response of the point source near the source. The advantages then of using the HMMA method are that fewer terms are required to converge in the

predominantly direct field and that more absorptive boundary conditions may be used, whereas the CMA is limited to the assumption of very rigid walls.

It is important to note that there are some undulations in Fig. A.3 in the expected reverberant field region (far from the source). The Hopkins-Stryker equation does not predict these undulations, but instead assumes a constant value in the local spatially averaged reverberant-field. Undulations over space and frequency are expected in the reverberant field.[6] Fig. A.3 actually demonstrates the necessity for local spatial averaging to smooth these reverberant field undulations out. In practice, 1/3 octave bands are often measured, which inherently smooth the results.

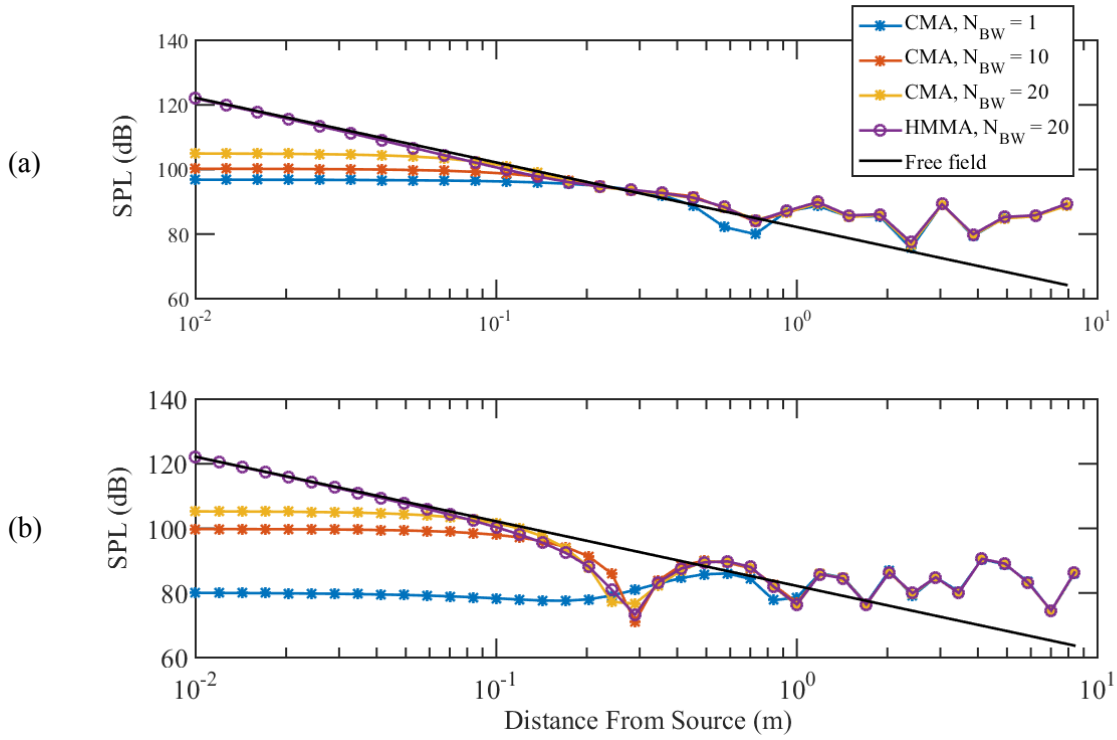

Fig. A.3. The axial SPL (re 20μ Pa) for two enclosures is plotted for both HMMA ($N_{BW} = 20$) and CMA, the latter with three different modal widths ($N_{BW} = 1, 10, \text{and } 20$) as functions of distance from the point source along a line. The room dimensions are $(L_x, L_y, L_z) = (5, 6, 7)$ m. The absorption is (a) $\bar{\alpha} = 0.1$ and (b) $\bar{\alpha} = 0.01$ both of which are uniformly distributed about the room. The source excites the room at 200 Hz and is positioned exactly 1 m from the origin in all directions for both cases. The points were measured along the $\theta = 45°$ and $\phi = 50°$ axis. The free-field sound power level for the monopole source was 90 dB re 10^{-12} W.

A.5 Image Source Method

When a source is near a rigid (or nearly rigid) reflecting plane, the reflection of a sound ray from the boundary to a position in the field can be treated as though it emerged from an image source with the same source strength. This concept is illustrated in Fig. A.4. For an enclosure, this concept can be extended infinitely for each boundary. The steady-state acoustic pressure and particle velocity responses are then the summations of all image source contributions at a certain position. The following derivation of the image-source method is based on the derivation from Allen and Berkley[24] for a rectangular parallelepiped enclosure geometry (see Fig. A.1), but could be generalized to other geometries.[30]

A.5.1 Rigid Wall Solution

The image source method can be derived from the modal analysis solution for completely rigid walls.[24] This is represented by Eq. (A.47) with an infinite wall impedance ($Z_S \to \infty$):

$$\hat{p}(k,\vec{r}_0,\vec{r}) = -j\rho_0 ck\hat{Q}_s \sum_{n_x=0}^{\infty}\sum_{n_y=0}^{\infty}\sum_{n_z=0}^{\infty} \frac{\Psi_{n_x,n_y,n_z}(\vec{r}_0)\Psi_{n_x,n_y,n_z}(\vec{r})}{\Lambda_{n_x,n_y,n_z}\left(k^2 - k_{n_x,n_y,n_z}^2\right)}, \tag{A.63}$$

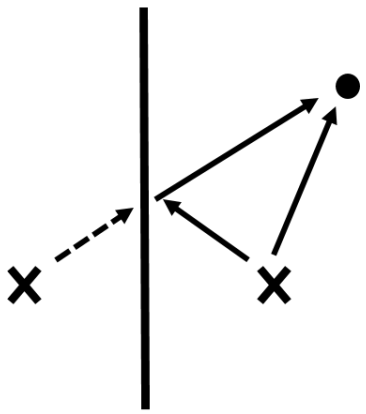

Fig. A.4. The direct and reflected sound due to a rigid boundary. The reflection can be represented as an image source on the other side of the boundary.

where $\vec{r}_0$ and $\vec{r}$ represent the source and receiver positions respectively. The eigenvalues for a rigid-walled room are given in Eqs. (A.39) through (A.42) and the eigenfunction is given in Eq. (A.37).

The eigenfunctions for a rigid-walled room are comprised of cosine functions, which are even:

$$\cos(-x) = \cos(x). \tag{A.64}$$

This property allows us to substitute for the normalization constant [see Eqs. (A.44) and (A.45)] with a sum from $-\infty$ to ∞ over n_x, n_y and n_z. A simple example in one dimension will illustrate how this is done. Assuming $n_y = n_z = 0$,

$$\sum_{n_x=0}^{1} \frac{\cos(n_x x)}{\Lambda_{n_x}} = \frac{\cos(0x) + 2\cos(1x)}{L_x}. \tag{A.65}$$

By summing from $n_x = -1$ to $n_x = 1$ without the ϵ_{n_x} factor of the normalization constant, we again have

$$\sum_{n_x=-1}^{1} \frac{\cos(n_x x)}{L_x} = \frac{\cos(-x) + \cos(0x) + \cos(x)}{L_x} = \frac{\cos(0x) + 2\cos(1x)}{L_x}, \tag{A.66}$$

This concept can be expanded to all three dimensions, meaning one can write Eq. (A.63), by factoring out $V = L_x L_y L_z$ without the additional ϵ_i normalization constant as

$$\hat{p}(k, \vec{r}_0, \vec{r}) = \frac{-j\rho_0 ck\hat{Q}_s}{V} \sum_{n_x=-\infty}^{\infty} \sum_{n_y=-\infty}^{\infty} \sum_{n_z=-\infty}^{\infty} \frac{\Psi_{n_x,n_y,n_z}(\vec{r}_0)\Psi_{n_x,n_y,n_z}(\vec{r})}{\left(k^2 - k_{n_x,n_y,n_z}^2\right)}. \tag{A.68}$$

The eigenfunctions can be written in terms of complex exponentials using the relationship

$$\Psi_x = \cos(k_x x) = \frac{1}{2}\left(e^{jk_x x} + e^{-jk_x x}\right). \tag{A.69}$$

Using $n = (n_x, n_y, n_z)$, multiplying $\Psi_n(\boldsymbol{r}_0)\Psi_n(\boldsymbol{r})$, and collecting terms, the pressure becomes

$$\hat{p} = -\frac{j\rho_0 ck\hat{Q}_s}{8V}\sum_{n=-\infty}^{\infty}\sum_{m_x=0}^{1}\sum_{m_y=0}^{1}\sum_{m_z=0}^{1}\frac{e^{j(k_n\cdot d_m)}}{[k^2-k_n^2]}, \tag{A.70}$$

where d_m represents the following eight combinations

$$\mathrm{d}_m = \left[x_0 + (2m_x - 1)x\,, y_0 + (2m_y - 1)y,\ z_0 + (2m_z - 1)z\right]. \tag{A.71}$$

As with n, we may substitute $m = (m_x, m_y, m_z)$ and represent the triple sum with one sum

$$\hat{p} = -\frac{j\rho_0 ck\hat{Q}_s}{8V}\sum_{n=-\infty}^{\infty}\sum_{m=0}^{1}\frac{e^{j(k_n\cdot d_m)}}{[k^2-k_n^2]}. \tag{A.72}$$

Using the sifting property of the delta function

$$\int_{-\infty}^{\infty}\delta(x-a)F(x)dx = F(a), \tag{A.73}$$

we can write Eq. (A.72) as

$$\hat{p} = -\frac{j\rho_0 ck\hat{Q}_s}{8V}\sum_{m=0}^{1}\iiint_{-\infty}^{\infty}\frac{e^{j(\xi\cdot d_m)}}{[k^2-\xi^2]}\sum_{n=-\infty}^{\infty}\delta(\xi-k_n)d^3\xi. \tag{A.74}$$

Using a Fourier series for the *x*-component, with analogs for the y and z components, we see that

$$\sum_{n_x=-\infty}^{\infty}\delta\left(\xi_x - \frac{n_x\pi}{L_x}\right)d\xi_x = \frac{L_x}{\pi}\sum_{n_x=-\infty}^{\infty}e^{j2L_x n_x\xi_x}, \tag{A.75}$$

which allows us to rewrite Eq. (A.74) as

$$\hat{p} = -\frac{j\rho_0 ck\hat{Q}_s}{8V}\sum_{m=0}^{1}\iiint_{-\infty}^{\infty}\frac{e^{j(\xi\cdot d_m)}}{[k^2-\xi^2]}\left(\frac{L_xL_yL_z}{\pi^3}\right)\sum_{n=-\infty}^{\infty}e^{j2\left(L_xn_x\xi_x+L_yn_y\xi_y+L_zn_z\xi_z\right)}d^3\xi, \tag{A.76}$$

which simplifies to

$$\hat{p} = -\frac{j\rho_0 ck\hat{Q}_s}{(2\pi)^3}\sum_{m=0}^{1}\iiint_{-\infty}^{\infty}\sum_{n=-\infty}^{\infty}\frac{e^{j\xi(d_m+d_n)}}{[k^2-\xi^2]}d^3\xi, \tag{A.77}$$

where

$$d_n = 2\left(n_x L_x, n_y L_y, n_z L_z\right). \tag{A.78}$$

One can see that Eq. (A.77) is equivalent to the free-field Green's function of a monopole by recognizing that the triple integral is a Fourier transform of a plane wave. A spherical wave can be represented by summing an infinite number of plane waves[31]:

$$\frac{e^{ik|a|}}{4\pi|a|} = \frac{1}{8\pi^3}\iiint_{-\infty}^{\infty}\frac{e^{j\,\xi\cdot a}}{[k^2-\xi^2]}d^3\xi. \tag{A.79}$$

Using this expression we can write Eq. (A.76) more simply as

$$\hat{p} = -j\rho_0 ck\hat{Q}_s\sum_{m=0}^{1}\sum_{n=-\infty}^{\infty}\frac{e^{jk|d_m+d_n|}}{4\pi|d_m+d_n|}. \tag{A.80}$$

The acoustic pressure response in the frequency domain is thus given by the Eq. (A.80). If an impulse response is desired, an inverse Fourier transform is required, although the image source derivation was originally developed for an impulse response in the time domain.[24-25,32]

A.5.2 Nonrigid Walls

The image source method was derived by assuming completely rigid walls or that there was effectively no absorption in the room. Allen and Berkley proposed that although the answer may not be exact, the image source method could still be used for rooms under certain conditions: (1) a frequency range of 100 Hz to 4,000 Hz, (2) a pressure reflection coefficient of $R > 0.7$ which translates to an average absorption coefficient of $\bar{\alpha} < 0.5$, (3) room geometries of typical offices, and (4) the source and receiver are not too close to a wall.[24]

Under these conditions, we can develop an image source method useful in typical rooms where the pressure reflection coefficient is less than unity. For typical nonrigid enclosure boundary conditions, the amplitude of a ray decreases in proportion to the pressure reflection coefficient R of the boundary. The amplitude for each image source is then decreased by the number of boundaries that it crosses in order to reach the receiver position. The factor that the pressure amplitude is decreased by may be written as[25]

$$A(n,m) = R_{x1}^{|n_x - m_x|}\, R_{x2}^{|n_x|}\, R_{y1}^{|n_y - m_y|}\, R_{y2}^{|n_y|}\, R_{z1}^{|n_z - m_z|}\, R_{z2}^{|n_z|}, \tag{A.81}$$

where R_{x1} represents the reflection coefficient of the $x = 0$ wall, R_{x2} is the $x = Lx$ wall, and so on. Notice that either a complex or a real-valued pressure reflection coefficient is possible.

For a wall with a known boundary impedance, the pressure reflection coefficient may be written as

$$R = \frac{\zeta \cos(\theta_i) - 1}{\zeta \cos(\theta_i) + 1}, \tag{A.82}$$

where ζ is the normalized specific acoustic impedance in Eq. (A.13) and θ_i is the angle of wave incidence on the boundary. In order to simplify the image method, the assumption is made that the pressure reflection coefficient R is independent of angle of incidence. This is equivalent to saying that the wall impedance is proportional to $\sec(\theta)$, which is different than a common assumption with modal analysis that the boundaries are locally reacting. With this simplification, the pressure reflection coefficient becomes

$$R = \frac{\zeta - 1}{\zeta + 1}. \tag{A.83}$$

Although it is uncertain what this means physically, Allen and Berkley considered it to be a reasonable approximation.

The pressure response at the receiver position for a room with nonrigid boundaries modifies Eq. (A.80) to

$$\hat{p} = -j\rho_0 ck\hat{Q}_s \sum_{m=0}^{1} \sum_{n=-\infty}^{\infty} \frac{A(u,l)}{4\pi d(m,n)} e^{-jkd(p,n)}, \tag{A.84}$$

where $d(m,n)$ represents the distance from the image source to the receiver position and can be written in matrix form as[25]

$$d(m,n) = \left\| \begin{bmatrix} 2m_x - 1 & 0 & 0 \\ 0 & 2m_y - 1 & 0 \\ 0 & 0 & 2m_z - 1 \end{bmatrix} \cdot \begin{bmatrix} x_0 \\ y_0 \\ z_0 \end{bmatrix} - \begin{bmatrix} x \\ y \\ z \end{bmatrix} - \begin{bmatrix} 2n_x & 0 & 0 \\ 0 & 2n_y & 0 \\ 0 & 0 & 2n_z \end{bmatrix} \cdot \begin{bmatrix} L_x \\ L_y \\ L_z \end{bmatrix} \right\|. \tag{A.85}$$

A.6 Similarity of the Models

A.6.1 Similarity of CMA and Image Source Solutions for Rigid Walls

Because the image source method can be derived from normal mode analysis for completely rigid walls, it should ideally converge to the same values. It would be tempting to say that a certain number of image sources correspond exactly to one mode or vice versa. The trouble is that the image source equation was derived from an infinite sum of modes. This infinite sum also became an infinite sum in the image source equation. Without any absorption for either method, the summations must both be infinite in order for these equations to be equal. A truncation results in inequalities between the two models.

The rigid-walled image source and modal analysis methods were simulated in an undamped room with dimensions $(L_x, L_y, L_z) = (5, 6, 7)$. A monopole source was located at $(x_0, y_0, z_0) = (1, 1, 1)$ with a free-field sound power level $L_\Pi = 90$ dB re 10^{-12} W. Figure A.5

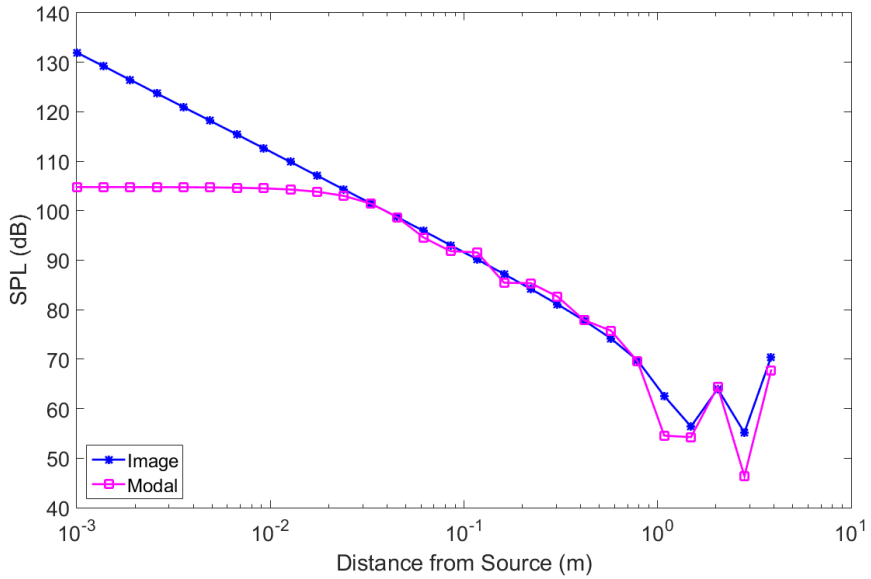

Fig. A.5. Walk-away lines from a point source in a rigid-walled room excited at 100 Hz using both the CMA and the image source method. The dimensions of the room was $(L_x, L_y, L_z) = (5, 6, 7)$ and the source was located at $(x_0, y_0, z_0) = (1, 1, 1)$. The source was a monopole with a free-field sound power level of 90 dB re 10^{-12} W. The walk-away axis was $\theta_0 = 90°$ and $\phi_0 = 0°$.

shows sound pressure levels at points increasing in distance away from the source at an angle $\theta_0 = 90°$ and $\phi_0 = 0°$ (this will be called a "walk-away line") at 100 Hz. Over 81 million image sources and 10 million modal amplitudes were summed for comparison. As was seen earlier, the CMA produces a result that approaches the free-field response of a monopole with an increasing number of modal contributions. In addition, the reverberant field, shows certain discrepancies that would likely be resolved if the summations did not need to be truncated.

For Fig. A.6, the same room parameters were used, but with over 138 million image sources, and 156 million modal amplitudes summed. The source was excited at 66.7 Hz, which corresponded to a natural frequency. The image source method was unable to resolve the amplitude and would again require an infinite summation to match the results of the modal method.

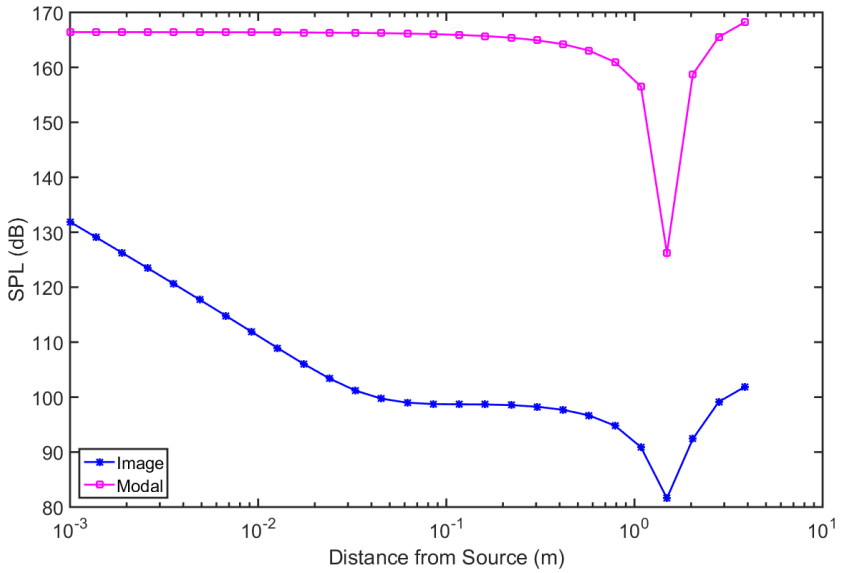

Fig. A.6. A walk-away line from a source excited at 66.7 Hz, which corresponds to a natural frequency for the room. The dimensions of the room are $(L_x, L_y, L_z) = (5, 6, 7)$ and the source was located at $(x_0, y_0, z_0) = (1, 1, 1)$. The source was a monopole with a free-field sound power level of 90 dB re 10^{-12} W. The walkaway axis was $\theta_0 = 90°$ and $\phi_0 = 0°$.

Figure A.7 shows the potential energy at 700 Hz in the same room as a function of the number of image sources and modal amplitudes included in the summation. The potential energy was found by simulating the PED at 700 Hz at 200 points in the room, each with an equal

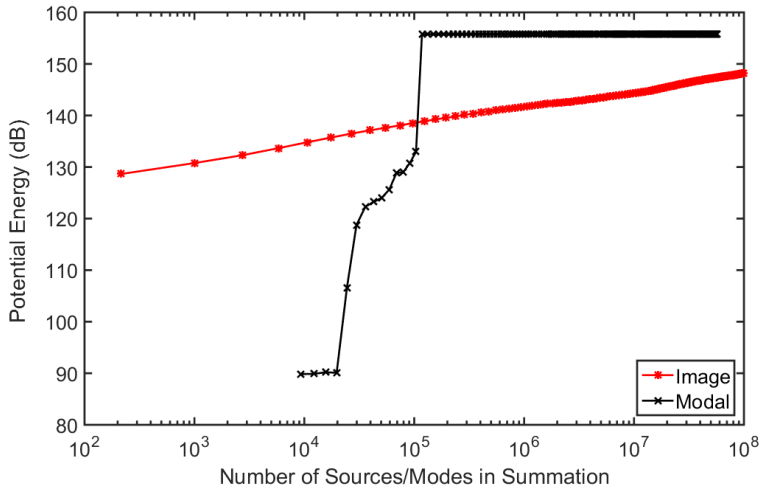

Fig. A.7. The total potential energy in an enclosure as the number of image sources and eigenvalues included in the summation is increased. The dimensions of the room are $(L_x, L_y, L_z) = (5,6,7)$ and the source was located at $(x_0, y_0, z_0) = (1,1,1)$. The source was a monopole with a sound power level of 90 dB re 1 pW. The potential energy was the summation of the PED from 200 points distributed through the room with equal volume.

volume and summing all the points. The image source method gradually approaches the classical modal method and would in theory agree with more image sources.

It is sufficient to say that in theory, with an infinite number of sums, the two models for completely rigid-walled enclosures should be equal. We will now discuss the more practical case with absorption included in the model.

A.6.2 Similarity of the Models for Nonideal Rooms

Introducing absorption into the models gives a more practical view of how similar the methods are. Figure A.8 shows walkaway lines at two different frequencies with very low absorption in the room. The room parameters were the same as those used for Fig. A.5 and A.6, and the absorption was uniform for all walls. Using the complex reflection coefficient, the image source results (blue), very closely match the HMMA (maroon) and CMA (green) except for the divergence of the CMA 5 cm from the source for the 60 Hz and 500 Hz conditions.

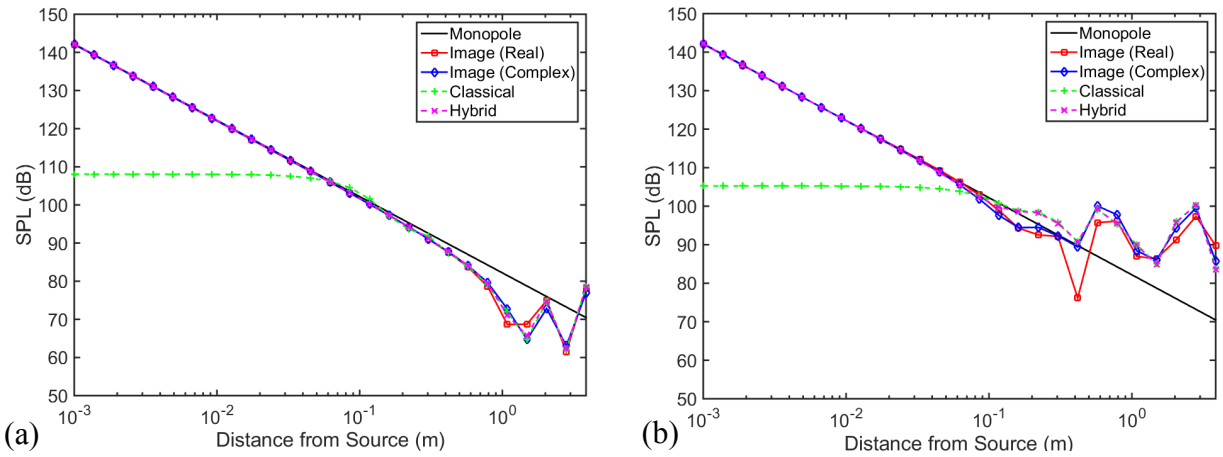

Fig. A.8. A walk-away line for (a) 100 Hz and (b) 500 Hz for a room with $\bar{\alpha} = 0.01$. The dimensions of the room are $(L_x, L_y, L_z) = (5, 6, 7)$ and the source was located at $(x_0, y_0, z_0) = (1, 1, 1)$. The source was a monopole with a free-field sound power level of 90 dB re 10^{-12} W. The walkaway axis was $\theta_0 = 90°$ and $\phi_0 = 0°$.

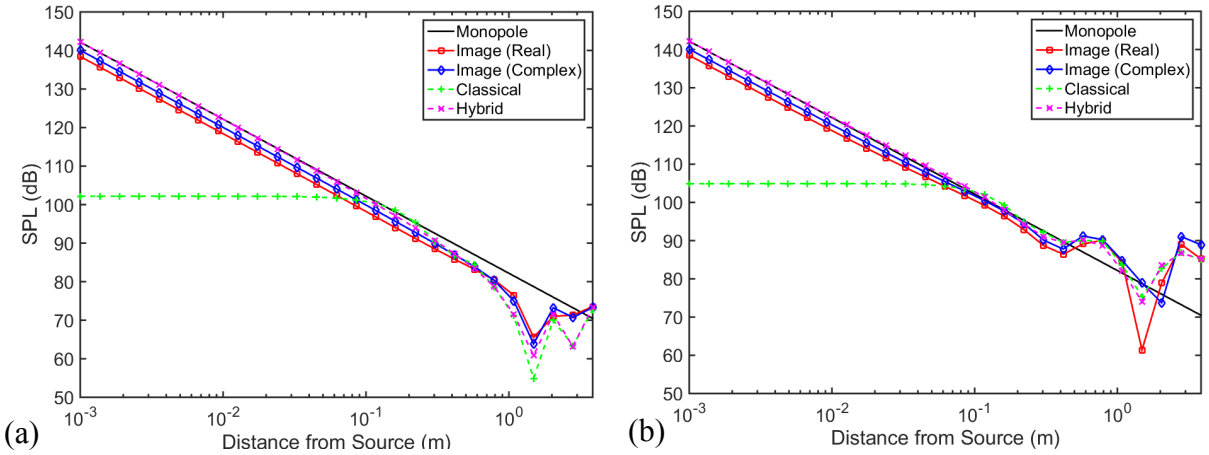

Fig. A.9. A walk-away line for (a) 100 Hz and (b) 500 Hz for a room with $\bar{\alpha} = 0.25$. The dimensions of the room are $(L_x, L_y, L_z) = (5, 6, 7)$ and the source was located at $(x_0, y_0, z_0) = (1, 1, 1)$. The source was a monopole with a free-field sound power level of 90 dB re 10^{-12} W. The walkaway axis was $\theta_0 = 90°$ and $\phi_0 = 0°$.

When more absorption is added (see Fig. A.9), the models follow similar trends, but have more amplitude discrepancies between them. This is due to the differences in boundary conditions. The image source method is based on the assumption that there is no angular dependence in the pressure reflection coefficient R. This is essentially the same as saying the impedance is proportional to $\sec(\theta)$, which means that the boundary is not locally reacting. On the other hand, the HMMA method assumes that the boundary condition for the eigenfunctions uses only the real part of the locally reacting impedance (see Sec. A.3.4).

The image source method could be improved by using an angularly dependent reflection coefficient. The modal analysis method could be improved by using the exact boundary condition rather than the modified solution. However, both of these improvements would significantly increase complexity and computation time of the methods, and are beyond the scope of this thesis.

Appendix B

Hybrid Modified Modal Analysis Validation

B.1 Experimental Setup

In order to generate confidence in the HMMA model, its results were compared with measurements from the BYU VAC mentioned in Ch. 3. This is a plaster-coated and painted concrete room with dimensions (3.4 × 2.9 × 2.6) m. It incorporates the option to add or remove acoustically absorptive panels to the walls and ceiling. The concrete floor is covered with vinyl composite tile. The treatments allow the room to be varied from a nearly hemi-anechoic to a very reverberant condition. By removing all of the absorption panels (see Fig. B.1), it becomes a nearly rectangular room with hard and smooth surfaces. There is a slight recess to the door, so a plug, consisting of 3.8 cm-thick MDF and surrounding 6.35 mm-thick steel plates was installed to cover the recess and make the associated wall much flatter (see Fig. B.2).

A 20.3 cm diameter dodecahedron loudspeaker with 7.6 cm diameter drivers was used to approximate a nominally omnidirectional source up to about 1.5 kHz. Its low-frequency roll-off was at about 100 Hz. It is pictured in the setup in Fig. B.3.

Fig. B.1. The VAC with all absorption panels removed.

The source was placed asymmetrically in the room and 15 sound pressure measurements were taken as shown in Fig. B.4. Table B.1 displays the position of each measurement relative to the lower left corner in Fig. B.4. A swept sinusoidal signal was played and the frequency response function between each position and the source was measured. The measurement bandwidth was 0 to 6.4 kHz with a 1 Hz frequency bin width. Because the reverberation times were measured in 1/3 octave bands, the absorption coefficients were interpolated for each frequency value within the 1/3 octave bands. Below 100 Hz, it was assumed that the absorption coefficient was the same value as the 100 Hz 1/3 octave band.

(a)  (b) 

Fig. B.2. The door recess (a) in the VAC was covered with a massive plug (b) consisting of 3.8 cm-thick MDF and gasketed steel on the edges to seal the plug into the opening.

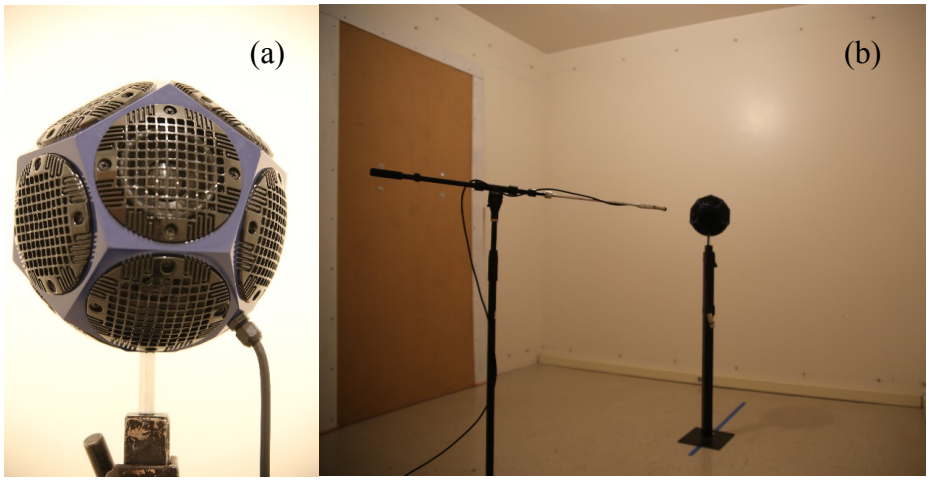

Fig. B.3. The (a) 20.3 cm dodecahedron loudspeaker with 7.6 cm drivers and (b) the experimental setup in the VAC. The ½ in microphone was moved to each position shown in Fig. B.4.

B.1.1 Damping

The boundary conditions in the models require a known wall impedance. As this is a very difficult quantity to obtain exactly, the absorption coefficient was used to estimate an approximate wall impedance. One can solve for the average absorption coefficient using the Eyring-Norris equation:[6]

$$\bar{\alpha} = 1 - e^{-\frac{0.161V}{T_{60}S}}, \tag{B.1}$$

where T_{60} is the reverberation time, S is the total surface area of the room, and V is the volume of the room. Reverberation times for the variable acoustics chamber were measured in 1/3

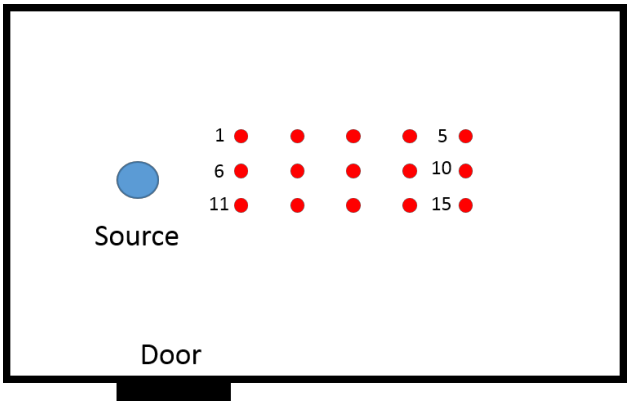

Fig. B.4. Experimental setup for validation of the VAC. The source is represented by the blue dot and the measurement positions are represented by the red dots.

Table B.1. Locations of the 15 microphone positions and source position in the VAC.

Position	x	y	z
1	1.484	2.09	1.077
2	1.776	2.101	1.077
3	2.078	2.096	1.077
4	2.381	2.091	1.077
5	2.683	2.094	1.077
6	1.456	1.807	1.077
7	1.752	1.782	1.077
8	2.131	1.839	1.077
9	2.428	1.817	1.077
10	2.72	1.805	1.077
11	1.452	1.536	1.077
12	1.75	1.536	1.077
13	2.074	1.524	1.077
14	2.377	1.535	1.077
15	2.673	1.53	1.077
Source	0.915	1.82	1.077

octave bands using EASERA™ and an integrated impulse response technique according to ISO 354, as closely as the size of the room allowed.[28,33] The results from several source and microphone positions were averaged, and because the room was small, the T_{60} was extrapolated from the -5 dB to -25 dB decay points (T_{20}). The average absorption coefficient followed from Eq. (B.1) as shown in Fig. B.5. This is based on the assumption that all of the surfaces had the same absorption coefficient. Although this was not strictly true, it was a good approximation for this room. In the models, the absorption due to the air was not accounted for, so it was included in the absorption at the boundaries. This effect is the main cause of the rise in the absorption coefficient at higher frequencies.

As described by Kuttruff,[6] one can use an impedance value to solve for an absorption coefficient of a locally reacting surface at any incident angle (θ_i):

$$\alpha(\theta_i) = \frac{4\,Re\{\zeta\}\cos\theta_i}{|\zeta|^2\cos^2\theta_i + 2Re\{\zeta\}\cos\theta_i + 1}, \tag{B.2}$$

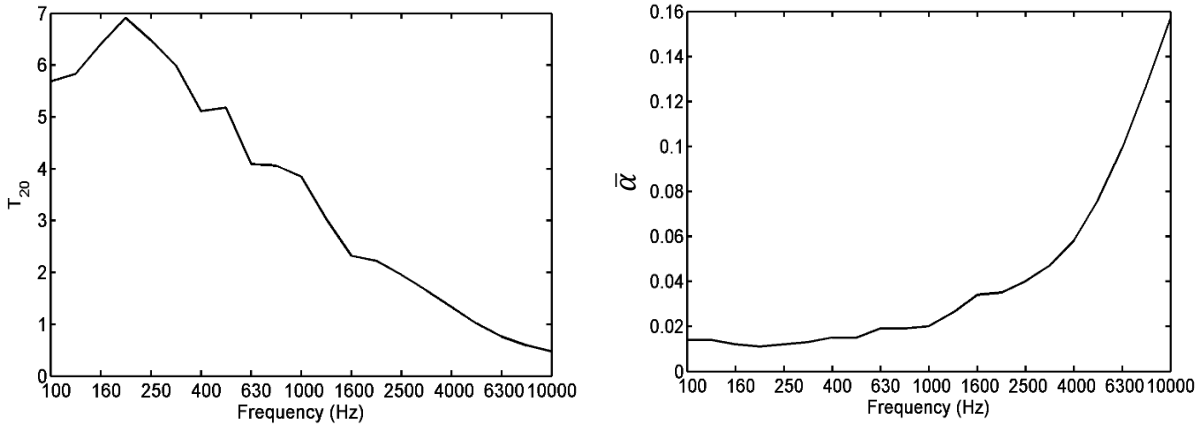

Fig. B.5. The (a) reverberation time and (b) Eyring-Norris absorption coefficient for the VAC with all absorptive panels removed and the door plug installed (including air absorption).

where ζ is the normalized specific acoustic impedance. For random incidence, the absorption coefficient comes from applying the Paris Formula[6]

$$\alpha_{ri} = \int_0^{\frac{\pi}{2}} \alpha(\theta_i) \sin(2\theta_i)\, d\theta_i. \tag{B.3}$$

Using Eqs. (B.2) and (B.3), the random-incidence absorption coefficient for a locally reacting surface is then

$$\alpha_{ri} = \frac{8}{|\zeta|^2}\cos\mu\left[|\zeta| + \frac{\cos(2\mu)}{\sin\mu}\arctan\left(\frac{|\zeta|\sin\mu}{1+|\zeta|\cos\mu}\right) - \cos\mu\ln(1+2|\zeta|\cos\mu+|\zeta|^2)\right], \tag{B.4}$$

where μ is the phase angle of the normalized specific acoustic impedance. As can be seen from Eq. (B.4), there is an infinite number of impedance magnitude and phase combinations that result in the same absorption coefficient. However, one can generate many random real and imaginary impedance values, calculate the absorption coefficient of each using Eq. (B.4), and choose the impedance that most closely matches the absorption coefficient. Xu and Sommerfeldt point out that when using the HMMA method, impedances with a phase angle greater than $\pi/4$ converge

more quickly, so the phase angle in this study was constrained to values larger than $\pi/4$.[22] To illustrate this method, three different random impedances are shown in Fig. B.6 per frequency. Although differences in impedance magnitude and phase are significant, the random-incidence absorption coefficient is nearly identical for all three cases.

B.2 Results

B.2.1 Convergence of the Model

To demonstrate the convergence of the model, as described in App. A, the energetic average of the total sound pressure level is shown in Fig. B.7 for three different impedance values as a function of the number of summed modal bandwidths. By including 100 modal bandwidths, the value had nearly converged to its final value. This number of bandwidths was chosen for computational efficiency, but it still converged with reasonable accuracy.

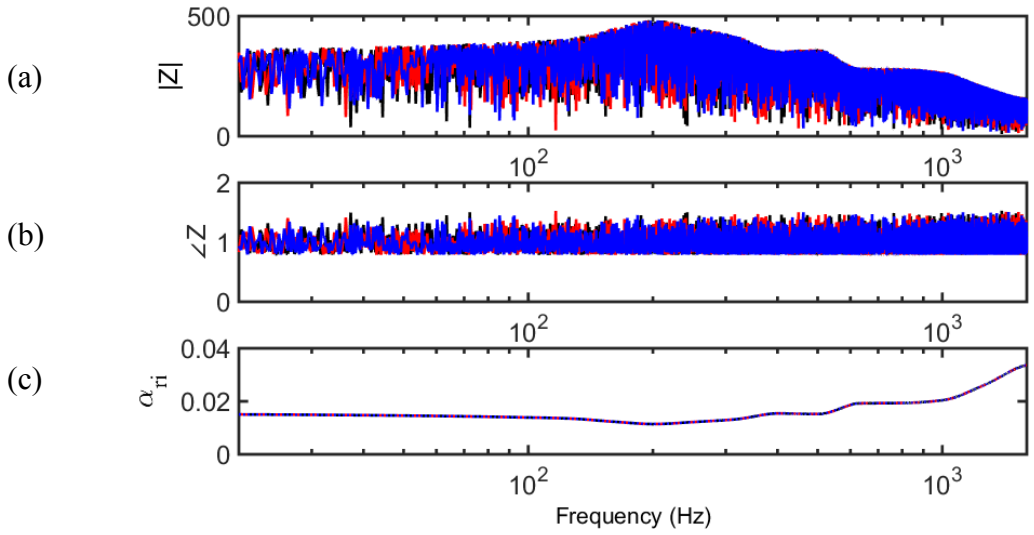

Fig. B.6. (a) The magnitude of the normalized specific acoustic impedance for three different cases per frequency that all have the nearly same random incidence absorption coefficient. (b) The phase angle of the impedance. The phase was restricted from $\pi/4$ to $\pi/2$. (c) The random incidence absorption coefficient calculated for the impedance values using Eq. (B.4).

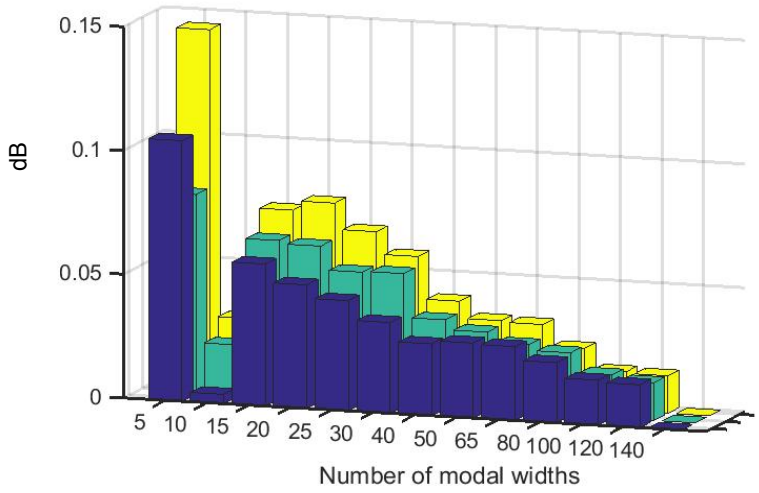

Fig. B.7. The energetic average value of the total sound pressure level for all 15 points relative to the value for 140 modal widths, modeled by the HMMA for the VAC (see Fig. B.4). The results for the three different random impedance sets at each frequency from Fig. B.6 are plotted.

B.2.2 Spectral Validation

To eliminate the effects of differences in source strength in the model and that in the measurements, the transfer function between the acoustic pressure at two different positions was compared. For the measurements, this was done by measuring the frequency response between the input to the source and the microphone output for each position then dividing one frequency response function by the other. In the model, this was accomplished by setting the source strength to a constant value then dividing the pressure spectrum at one position by that at the other. This allowed a look at the isolated room response between the two points.

Figure B.8 shows the transfer function between position 1 and position 9 in Fig. B.4 from 40 Hz to 150 Hz. The noise in the measurement below 100 Hz was due to the fact that the dodecahedron had very low output below about 100 Hz. The signal-to-noise ratio was significantly lower for those frequencies. One can see from the results that the model predicts the transfer function very well for low frequencies. Fig. B.9 illustrates the difference in the

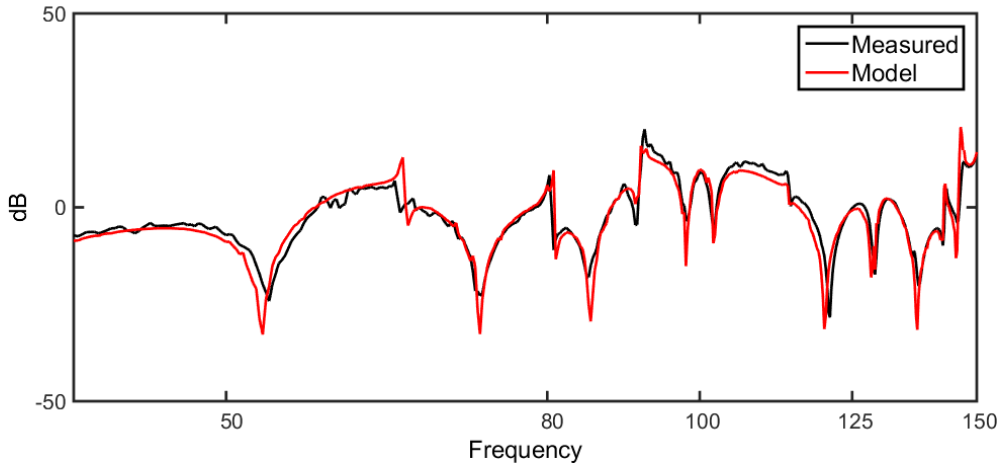

Fig. B.8. Measured and modeled transfer functions between position 1 and position 9 in the VAC (see Fig. B.4).

model for each of the three different impedance cases from Fig. B.6. There is very little difference between the results at each frequency.

With increasing frequency, the modal density of the field increases, causing the field to become more random. Extending the measurement to higher frequencies as shown in Fig. B.10, one can see that the general trends are similar, but the agreement is not as clear. Due to the

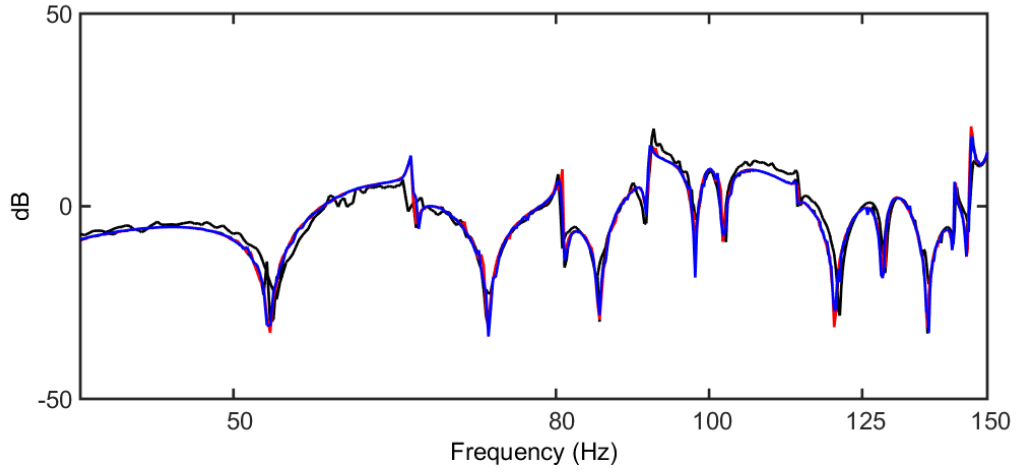

Fig. B.9. The transfer function between position 1 and position 9 in the VAC. The measurement (black) was taken with the 20.3 cm dodecahedron. Three different impedance values with nearly the same random incidence absorption coefficient were used for comparison.

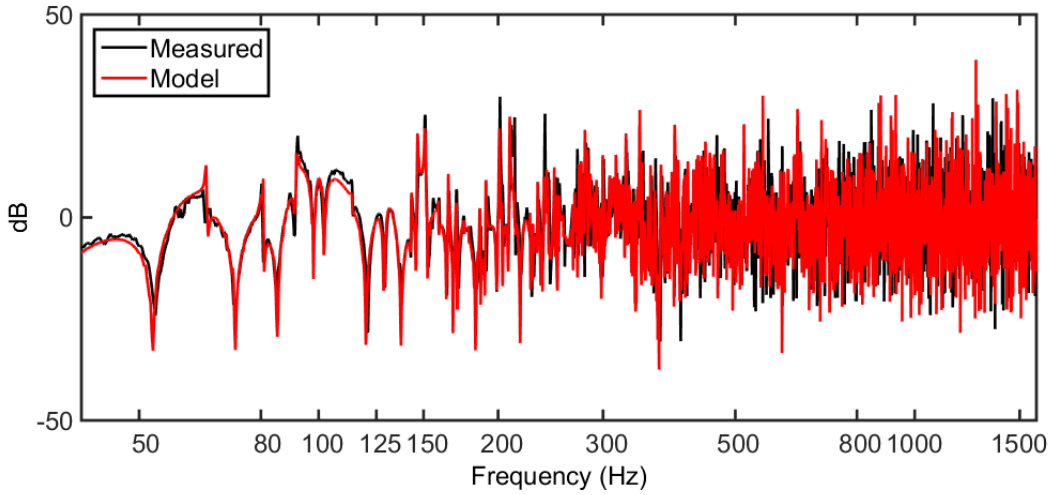

Fig. B.10. The sound pressure transfer function between positions 1 and 9 in the VAC up to 1500 Hz.

random nature of the field and the smaller wavelengths at higher frequencies, errors in the measured room dimensions and microphone loudspeaker positions become more significant.

Because much of the work for the thesis was at frequencies above the Schroeder frequency, where the field is more random, a measure was needed to address how well the model approximated the sound field in this spectral region. It was beneficial then to apply a smoothing algorithm to the data at higher frequencies to see if the model still approximated the measured trend. One can smooth the magnitude of the transfer function using[40]

$$\langle |H(f)| \rangle = \sqrt{\frac{1}{f_2 - f_1} \int_{f_1}^{f_2} |H(f)|^2 df} \,, \tag{B.5}$$

where f_1 and f_2 are the lower and upper bounds of the averaging bandwidth. The interval can be a constant value, such as 100 Hz, or determined by (1/N)th octave bands as was used in this thesis.

Figure B.11 shows the results of the smoothing algorithm for 1/24 octave-band smoothing and how it affects the frequency response. Figure B.12 shows the results of applying this smoothing algorithm to the measurements from 63 Hz to above 4 kHz for several different

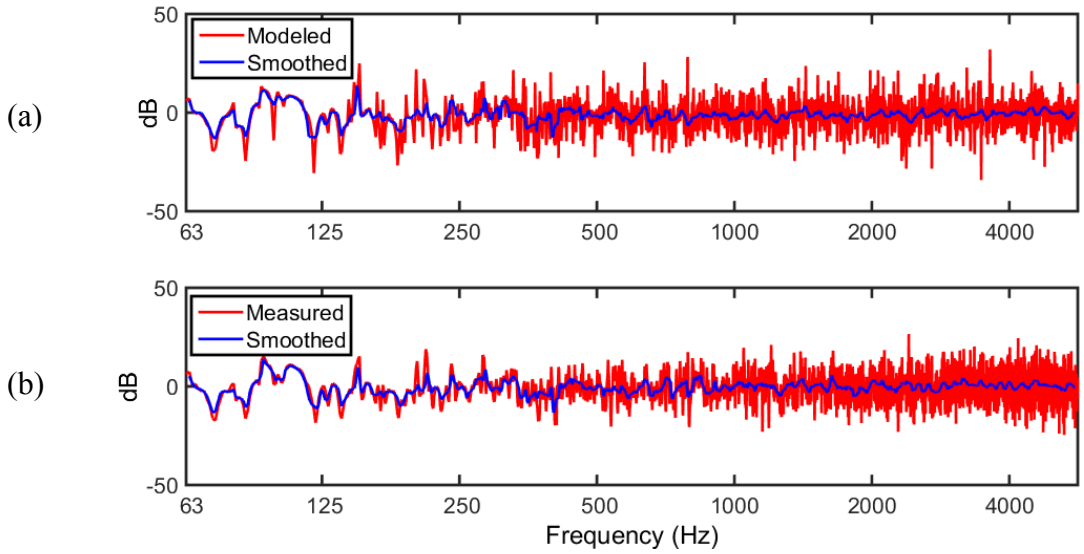

Fig. B.11. Smoothed transfer functions between position 1 and position 9 in the VAC. The transfer functions was smooth by 1/24 octave band, giving an idea of the trends at higher frequencies. The smoothing was done on both (a) the model and (b) the measurement.

$(1/N)^{th}$ octave bands. From these we see that the model is able to predict the trends of the measurement up to high frequencies. Due to the randomness of the field, the larger the average over frequency, the better the model matched the measurement.

To determine how well the model matches experimental data, we used the root-mean-square difference (RMSD) between the model and the measurements:

$$RMSD = \sqrt{\frac{1}{N}\sum_{i=1}^{N}\left(L_{H_{i,meas}} - L_{H_{i,mod}}\right)^2}, \tag{B.6}$$

where $L_{H_{i,meas}}$ is the frequency response function of the measurement for the i^{th} frequency bin on a decibel scale,

$$L_{H_{meas}} = 20\ log(|H_{meas}|), \tag{B.7}$$

and $L_{H_{i,mod}}$ is the frequency response function of the model for the ith frequency on a decibel scale,

$$L_{H_{mod}} = 20\ log(|H_{mod}|). \quad \text{(B.8)}$$

In Fig. B.13, we see that the lowest RMSD is found for the full octave band as expected.

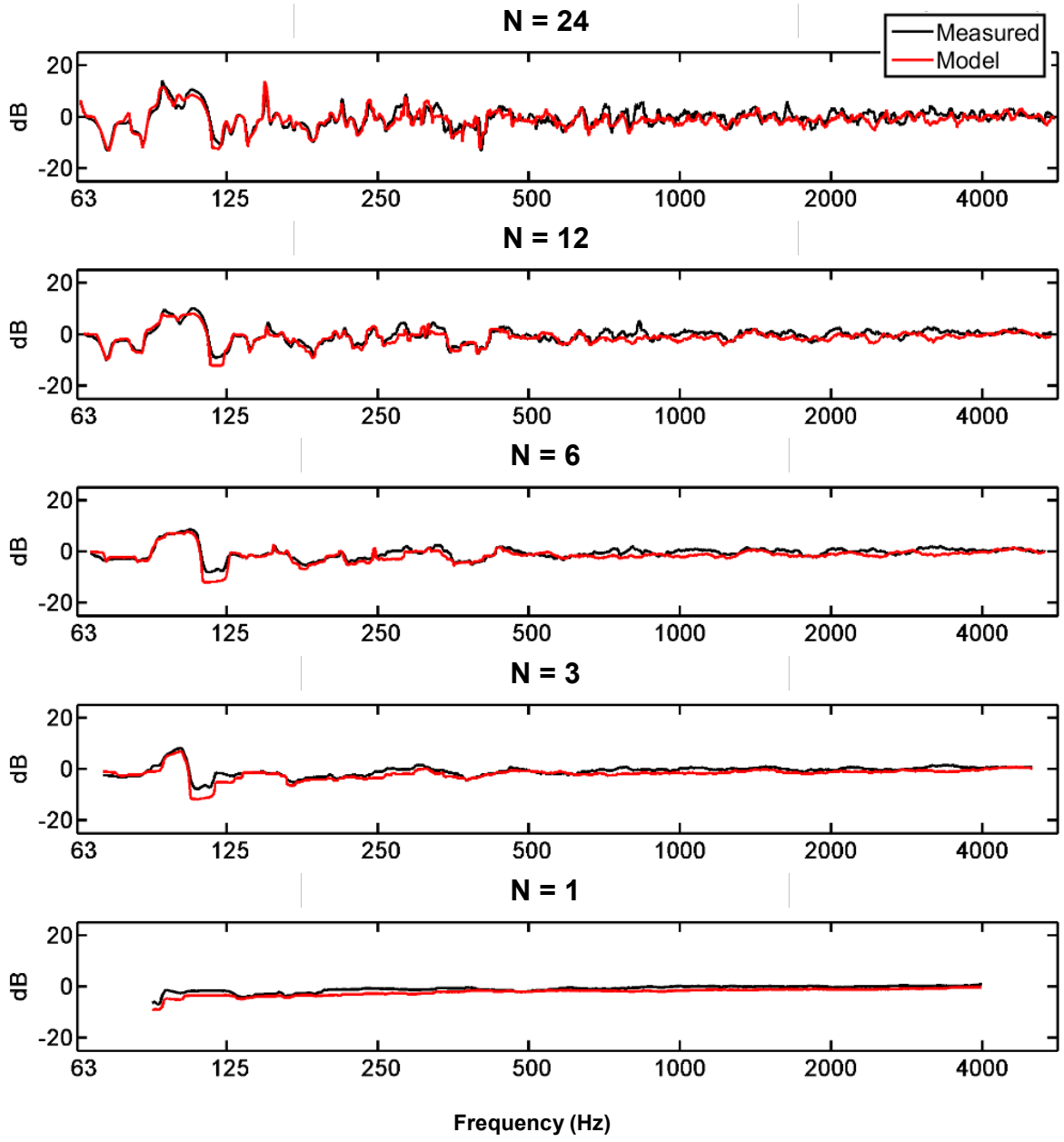

Fig. B.12. Smoothed transfer functions between position 1 and position 9 in the VAC. The transfer functions were smooth by (1/N)th octave band at each frequency.

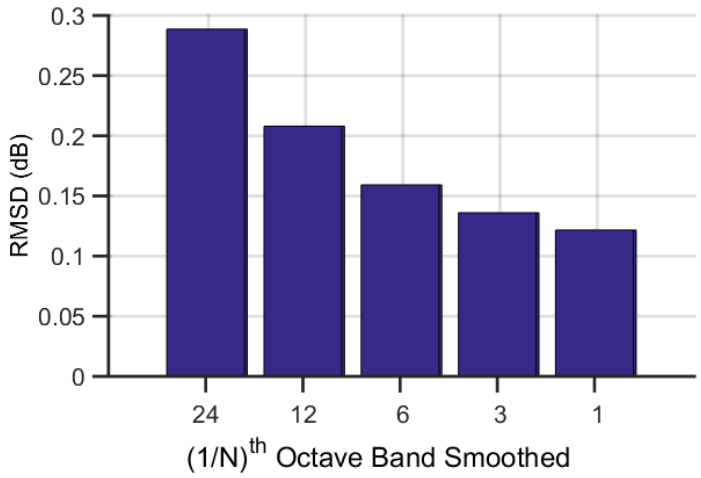

Fig. B.13. The RMSD between the measurement and the model for the transfer function between position 1 and position 9 (see Fig. B.4).

B.2.3 Spatial Validation

Up to this point, we have shown only the results for the measured transfer function from point 1 to point 9. Because we also plan to do spatial averaging to improve room constant measurements, it is important to look at the spatial trends between the model and the measurements. The RMSD for each transfer function in Fig. B.14 varies by position, which can

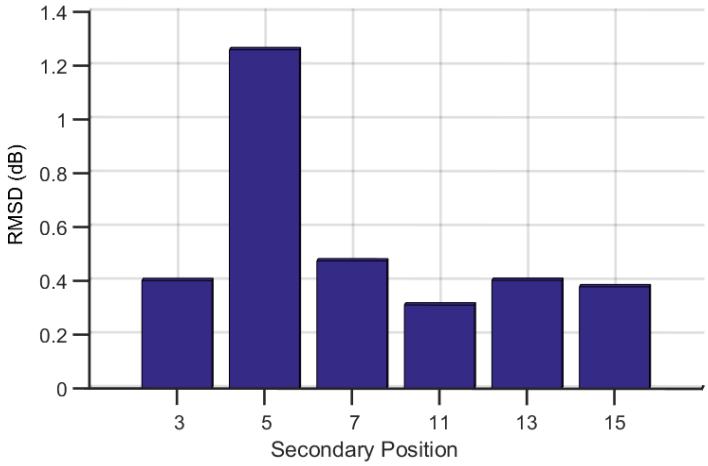

Fig. B.14. The RMSD between the measurement and the model for the transfer function between position 1 and six secondary positions in the VAC (see Fig. B.4) with 1/24 octave band smoothing.

be explained by measurement error. Fig. B.15 shows the 1/24 octave band smoothing for the transfer functions from position 1 to several other positions. The variance is generally at higher frequencies. Again, because the wavelength is smaller at higher frequencies, the precision of the measurement position becomes more crucial.

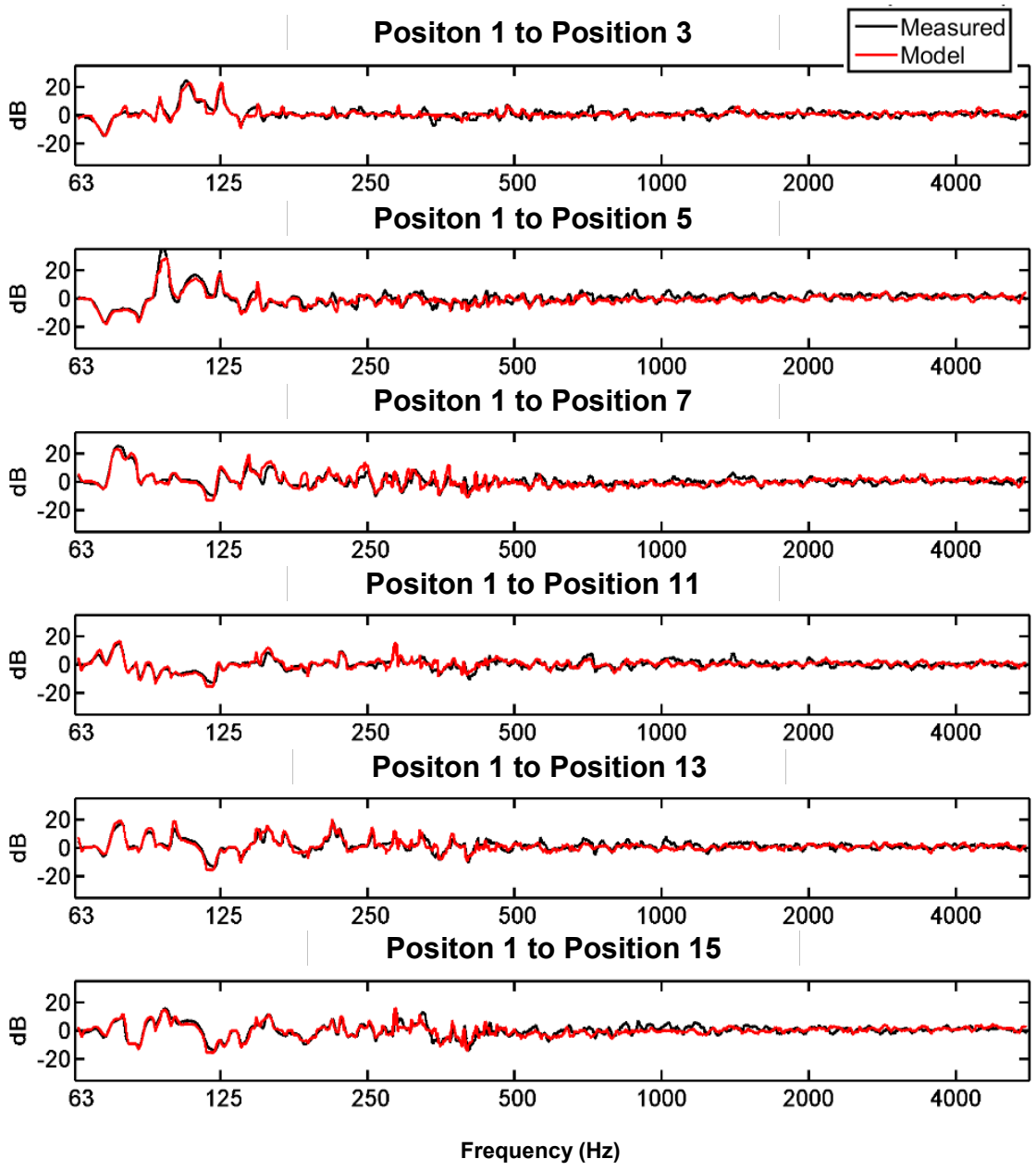

Fig. B.15. Smoothed transfer functions between position 1 and positions 3, 5, 7, 11, 13, and 15 in the VAC. The transfer function was smoothed by 1/24 octave band at each frequency.

Appendix C

ISO 3745 and ISO 3741 Measurements

The sound powers of several sources were measured according to the ISO 3745 and ISO 3741 standards[4,5] as benchmarks for how well the two-point method measured them in semi-reverberant rooms. A brief description of the two standards is given here.

C.1 ISO 3745

ISO 3745 describes a precision method for the measurement of sound power in either a completely anechoic room or a hemi-anechoic room.[5] By measuring the pressure on the surface of a Gaussian sphere surrounding the source and making the assumption that the measurements are in the acoustic far-field, the sound power may be approximated as

$$\langle \Pi(f) \rangle_t \approx \frac{1}{\rho_0 c} \sum_m \sum_n S_{m,n} \langle p_{m,n}^2(f) \rangle_t \,, \tag{C.1}$$

where $S_{m,n}$ represents an area weighting factor for the mth polar angle and the nth azimuthal angle, determined by microphone position. The standard for an anechoic room requires at least 32 microphones placed in specific positions around the device under test (DUT) such that $S_{m,n}$ is

equal for each microphone position. Should one have more measurement positions, as was the case for the research repeated in this thesis, it is simply necessary that $S_{m,n}$ be known.

The microphones in the BYU anechoic chamber were placed on a semi-circular arc surrounding the source in the polar direction, as shown in Fig. C.1. There were 37 microphones in total, spaced in 5° increments, with a microphone at each pole. The source was then rotated in the azimuthal direction in 10° increments. A measurement was captured by each microphone at each azimuthal-angle for a total of 1,262 unique measurement positions. In reality, there are 1,369 total measurements taken because the pole measurements were repeated with each rotation

Fig. C.1. Semicircular arc array in the BYU anechoic chamber with a radius of 1.8 meters from the circular center to the microphones. The source sits on a turntable, which rotates it a full 360° in the azimuthal angle.

and averaged. Before being summed, the mean-square pressure measurements were weighted using the area factors $S_{m,n}$ described by Leishman et al:[34]

$$S_{0,n} = \int_{\phi_n-\frac{\Delta\phi}{2}}^{\phi_n+\frac{\Delta\phi}{2}} \int_{0}^{\frac{\Delta\theta}{2}} r^2 \sin(\theta)\, d\theta d\phi = \frac{4\pi r^2}{N} \sin^2\left(\frac{\Delta\theta}{4}\right), \qquad m = 0 \tag{C.2a}$$

$$S_{36,n} = \int_{\phi_n-\frac{\Delta\phi}{2}}^{\phi_n+\frac{\Delta\phi}{2}} \int_{\pi-\frac{\Delta\theta}{2}}^{\pi} r^2 \sin(\theta)\, d\theta d\phi = \frac{4\pi r^2}{N} \sin^2\left(\frac{\Delta\theta}{4}\right), \qquad m = 36 \tag{C.2b}$$

$$\begin{aligned} S_{m,n} &= \int_{\phi_n-\frac{\Delta\phi}{2}}^{\phi_n+\frac{\Delta\phi}{2}} \int_{\theta_m-\frac{\Delta\theta}{2}}^{\theta_m+\frac{\Delta\theta}{2}} r^2 \sin(\theta)\, d\theta d\phi \\ &= 2r^2 \Delta\phi \sin(\theta_m) \sin\left(\frac{\Delta\theta}{2}\right), \qquad m = 1,2 \ldots,35 \end{aligned} \tag{C.2c}$$

where r is the distance from the circular center to the microphones, θ is the polar angle, ϕ is the azimuthal angle, N is the total number of azimuthal measurements, m is the index for the polar angle, n is the index for azimuthal angle, $\Delta\phi$ is the difference between each azimuthal angle, and $\Delta\theta$ is the difference between each polar angle.[34] This method has a much higher spatial resolution than the 32 microphone positions required by ISO 3745 and is thus considered a more accurate measurement.

The definition of the directivity factor is the time-averaged intensity measured on a given axis in the far-field divided by the time-averaged intensity radiated by an omnidirectional source with the same power. A directivity factor of unity along an axis means that an omnidirectional source producing the same sound power would radiate the same intensity along that axis. Although commonly defined the principal axis, the directivity factor may be calculated at any angle.[16] The method for measuring it for a given microphone position is described in ISO 3745 as

$$\gamma_{m,n}(f) = 10^{\frac{L_{p(m,n)} - \overline{L_p}}{10}}, \tag{C.3}$$

where $L_{p(m,n)}$ represents the sound pressure level along the mth polar angle and nth azimuthal angle, and $\overline{L_p}$ is the area-weighted average sound pressure level. Another method of measuring the directivity factor is by using frequency response functions between a reference signal and the measurement positions. The formula for the directivity factor is then[15]

$$\gamma_{m,n}(f) = \frac{\langle I_{m,n}(f)\rangle_t}{\langle I_{omni}(f)\rangle_t} = \frac{4\pi r^2 \left|H_{m,n}(f)\right|^2}{\sum_m \sum_n S_{m,n} \left|H_{m,n}(f)\right|^2}, \tag{C.4}$$

where $H_{m,n}$ represents the frequency response for the mth polar angle and the nth azimuthal angle.

C.2 ISO 3741

ISO 3741 describes a precision method for measuring the sound power of a source in a qualified reverberation chamber.[4] The standard requires at least 6 microphones, separated randomly throughout the room as shown in Fig. C.2. The microphones must be positioned a minimum of 1 meter from reflecting surfaces, 1.5 meters from the source, and $\lambda/2$ away from each other (1.7 meters at 100 Hz). The reverberation chamber at BYU has diffusion panels hanging from the ceiling to encourage random reflections throughout the room. The sound power calculation also requires the total absorption in the room, which is measured from the reverberation time. The reverberation time was measured according to ISO 354, with six microphone positions and two source positions.[28]

Fig. C.2. A setup in the reverberation chamber for ISO 3741, including six microphones. Several clear diffusers in the reverberation chamber are also pictured hanging from the ceiling.

Appendix D

Engine Source

The sources in this study have been relatively small, especially compared to the room they are measured in. When the size of the source becomes large, some of the assumptions of the Hopkins-Stryker equation begin to break down. To see if the two-point method could accurately measure the sound power of a large source, the following test was performed on an internal-combustion engine in an industrial test cell. The approximate room and engine dimensions are shown in Table D.1. The frequency-dependent reverberation times of similar test cells were measured previously and used to approximate that of this specific cell. The others had roughly the same dimensions and wall materials, and were found to have an average absorption

Table D.1 – Dimensions of the room and the internal combustion engine.

	Room	Engine
L_x	5.5	0.8
L_y	7.9	1.3
L_z	3.6	1.1
V	157.7	1.1
S	184.1	6.5

coefficient of roughly $\bar{\alpha} = 0.3$ between using their reverberation times and the Eyring-Norris formula.

D.1 ISO 3747

The sound power measurements for the engine were measured according to ISO 3747:2010, which incorporates the reference sound power source method.[41] Twelve microphones were randomly placed around the engine in the test cell with all of the equipment still in the room. A Brüel and Kjær type 4224 sound power reference source was then sequentially placed at six different locations around the room and the sound pressure levels were measured. Ideally, the reference source would be placed on the floor near the engine, but the hardware and instrumentation required to run the engine made that proximity impossible. ISO 3747 Sec. 7.4.2 indicates that if a microphone is in the line-of-sight of the engine and not the reference source, the sound power level will be strongly overestimated. The standard also states that if the distances between the microphones and the source under test are less than those to the reference sound source, the results will be overestimated. To account for some of these overestimations, several outliers were removed from the reference source sound power measurement data to obtain a more representative average.

The reference source measurements were used to measure the room constant in situ, in similarity to the two-point method. The engine was then turned on and several sound power measurements were taken at different engine speeds and loads using all twelve microphones. While as indicated earlier, an effort was made to rmove the dominant outliers from the reference source power measurements, the final ISO 3747 results could still overestimate the sound power of the engine.

D.2 Two-Point Method

D.2.1 Room Constant Measurements

Figure D.1 shows a diagram of the experimental setup in the test cell for the two-point method. As shown in Fig. D.1, there were various different obstructions in the room required to run the engine. To assess the room constant, the sound power level of the reference directivity source was measured first, before the engine was turned on. There was significant background noise in the room below about 300 Hz, which complicated the measurement. Although the reference directivity source was effective in low-noise situations, it did not produce a sufficient signal-to-noise ratio in this room at lower frequencies.

One way to test the results of the two-point room constant measurement was to measure the sound power level of the reference source in the room, since it was already known. In this case, the two-point method measured the A-weighted broadband sound power level of the reference source to within 0.6 dB of the ISO 3741 and ISO 3745 results (see Fig. D.2). The 3-D intensity probe was positioned 0.27 meters and 1.5 meters from the reference directivity source at a 90^{o} polar angle and a 35^{o} azimuthal angle. The resulting two-point logarithmic room constant measurement is shown in Fig. D.3 and compared to estimated room constant calculations. The latter were calculated from the reverberation times of two similar test cells, and the volume and surface areas of the walls for this cell.

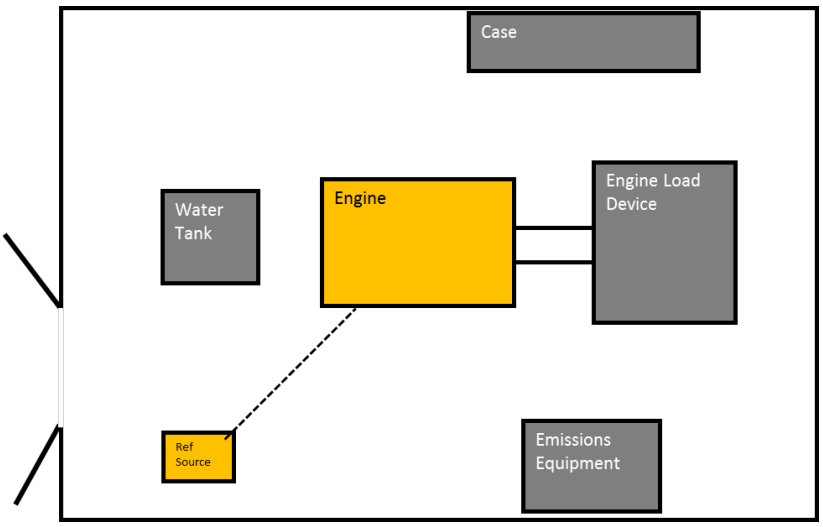

(a)

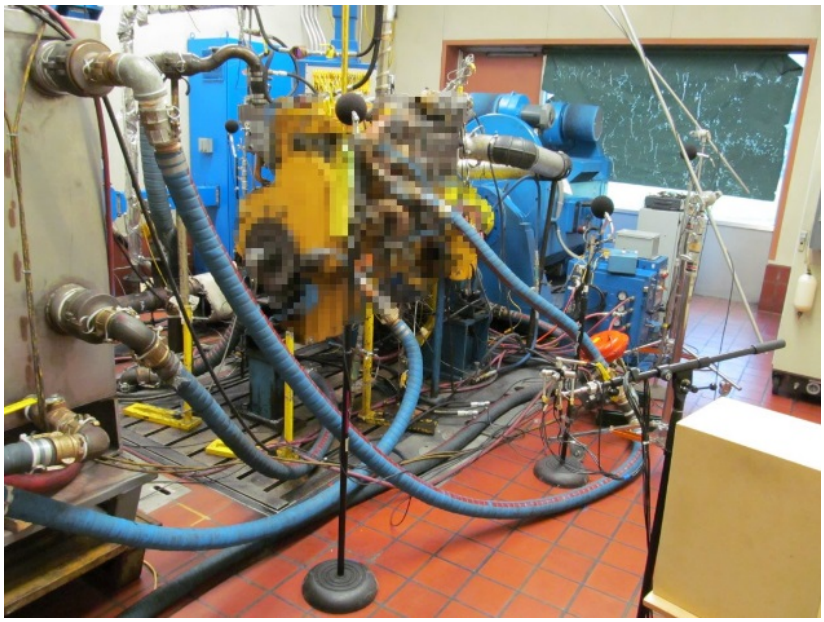

(b)

Fig. D.1. A (a) block diagram of the test cell, where the dashed line represents the axis of the two-point measurement positions. (b) A photograph of the test setup. Microphones with windscreens were used for the ISO 3747 measurement and the G.R.A.S. 50VI-1 3-D vector intensity probe was used for the two-point method measurements.

Because of the obstructive objects in the room, a simple volume estimation is overestimated and the surface area is underestimated. With this in mind, the dimensions of the objects of significant size in the room were roughly measured and the room volume and surface area were accordingly adjusted. The adjusted sound power level and room constant are also shown in Figs. D.2 and D.3. As can be seen from the figures, even with the volume and surface area adjustments, neither quantity is affected greatly on a logarithmic scale.

From Fig. D.2, one can also see that the in situ measurement of the room constant gives much better sound power results than the estimated room constant, even with adjustment. This could mean that the estimated room constant is a poor representation of the actual room constant, or at least at the measurement positions. On the other hand, because the A-weighted sound power level of the reference directivity source was measured within about 0.6 dB using the in-situ room constant, one may have some confidence that this is a reasonable estimation of the actual room constant at the measurement positions.

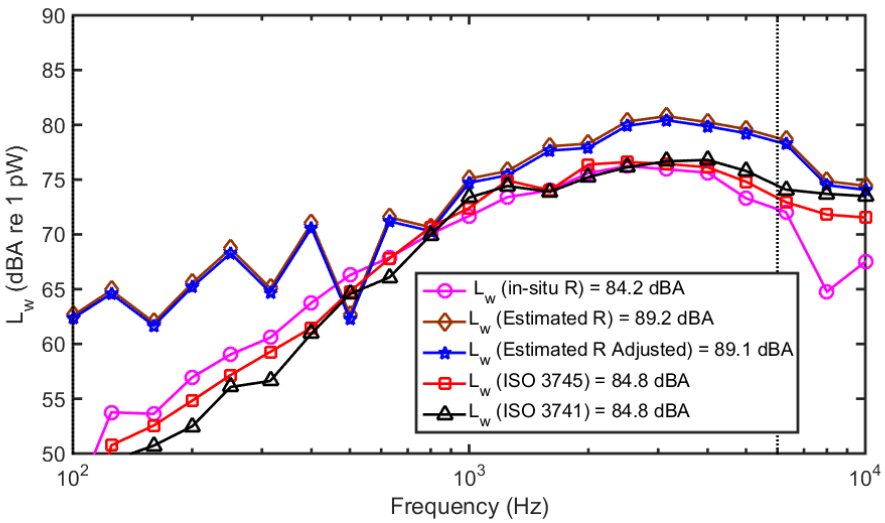

Fig. D.2. The sound power level of the reference directivity source measured using the in-situ room constant from the two-point measurement (magenta), the estimated room constant from the reverberation times of other test cells (brown), and the estimated room constant with an adjustment in volume and surface area to account for the engine (blue). All sound power measurements are compared to the ISO 3745 (red) and ISO 3741 (black) measurements.

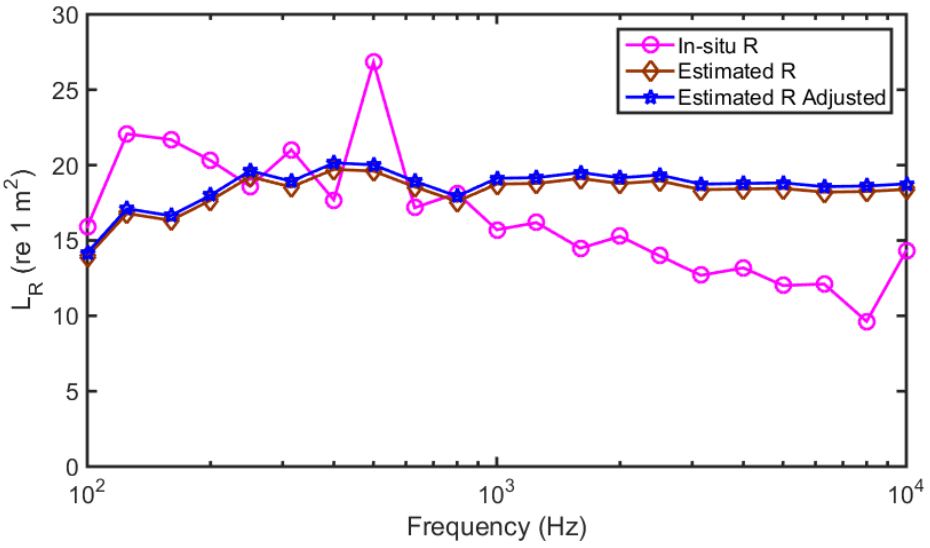

Fig. D.3. The room constant measured by the two-point in situ method, compared with the estimated room constant from reverberation times, and adjusted for the estimated volume and surface area of objects within the room.

D.2.2 Sound Power Measurements

Two different sets of engine sound power measurements were taken: one using r_1 = 1 m and r_2 = 2.4 m from its approximate geometric center, (assumed to be the acoustic center), and the other with r_1 = 0.5 m and r_2 = 2.1 m from the center. These were along the same axis as the previous measurements for the reference directivity source, although in hindsight, it might have been better to take the measurements along two different axes. If better results had been found along one axis than another, the results could have given insights into ways the method might have been better implemented with such a large source. In total, three engine speed and load combinations were measured. The results from the two-point in situ method were compared with measurements previously taken according to ISO 3747 (with the exceptions mentioned in Sec. D.1). The two-point method measurements and the ISO 3747 measurements were both taken in the same test cell with all the same equipment present. Another comparison was made by using the estimated room constant mentioned previously.

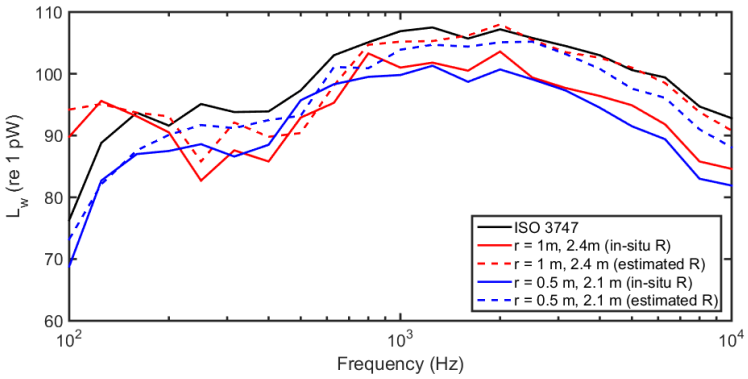

(a)

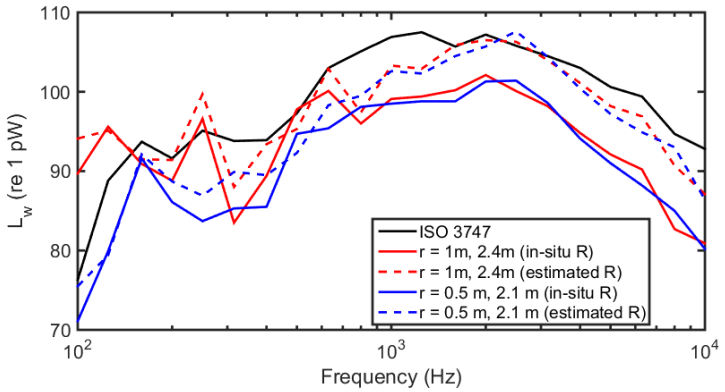

(b)

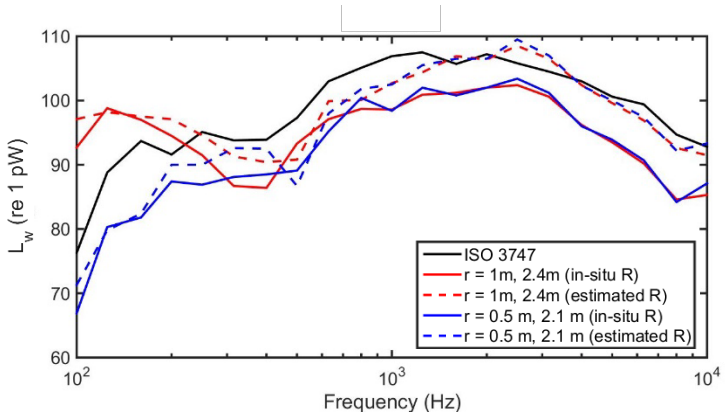

(c)

Fig. D.4. The sound power level of the engine at (a) 2309 rpm and 10 N·m, (b) 2000 rpm and 550 N·m, and (c) 1500 rpm and 2522 N·m. The ISO 3747 measurement is compared to two different sets of measurement positions. The first used $r_1 = 1$ m and $r_2 = 2.4$ m from the source, while the second was $r_1 = 0.5$ m and $r_2 = 2.1$ m from the source. The two-point method in-situ method (solid) compared to the two-point method with the estimated room constant (dashed).

The two-point in situ method appears to underestimate the ISO 3747 sound power level by about 5 to 6 dB for each test condition. Table D.2 shows a summary of the total A-weighted sound power levels for the various cases. Using the estimated room constant, the total sound power level is closer to that measured by ISO 3747, although the spectral shape does not seem to match the spectral shape of ISO 3747 as well as the two-point method with the measured in situ room constant.

D.3 Numerical Simulation

Because of the discrepancies, a numerical simulation was conducted using HMMA and the typical reverberation times of tests cells. To test the effects of having a distributed source, a very simple case was modeled. Two monopoles of the same source strength were separated by 1.25 meters. A third monopole was modeled as the reference directivity source. The source and measurement positions for the numerical simulation are depicted in Fig. D.5 and given specifically in Table D.3. In the figure, the reference source is represented as a blue square, the acoustic center of the distributed source is the blue circle, and each individual monopole is a blue x. The red points represent the measurement positions. The measurements were point measurements rather than spatial averages, as were those of the engine measurements. The circles around the sources represent the critical distance for an omnidirectional source. The 1/3 octave absorption coefficients of the room are given in Table D.4. The frequency of the simulation is the same as in Ch. 3, 1/24 octave spaced frequencies for every 1/3 octave.

Table D.2. The total sound power level for the second set of measurements (r = 0.5 m and 2.1 m) compared to the ISO 3747 measurements. The measurement quantity for the two-point method is GED.

L_w (A)	2309 rpm	2000 rpm	1500 rpm
ISO 3747	115.8	115.1	115.9
In Situ R	109.2	108.9	110.5
Estimated R	113.5	113.6	115.4

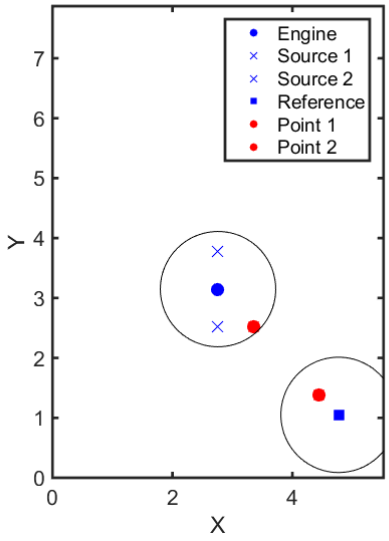

Fig. D.5. The numerical simulation of the engine measurement. The circles represent the critical distance of an omnidirectional source. The room dimensions are the same as those given in Table D.1 for the test cell.

The room constant and the sound power of the reference directivity source (a single monopole) were simulated first. As shown in Fig. D.6, they appear to approach the actual values at higher frequencies. Using the measured room constant from this simulation, the sound power level of the two-monopole distributed source was measured and is shown in Fig. D.7.

The errors are much greater for this sound power level than for that of a single monopole source. The greater errors are likely due to the directivity effects of the distributed source. At least one measurement position was in the near field of the source, where the configuration has a complicated radially dependent directivity factor that was not being accounted for in the two-point method equation. Near-field directivity effects were not accounted for in the engine measurements either.

Table D.3. Three source positions and two measurement positions used to simulate a single distributed source in a typical test cell.

	x	y	z
Source 1	2.76	2.52	1.05
Source 2	2.76	3.77	1.05
Reference Source	4.77	1.05	1.05
Point 1	3.35	2.53	1.05
Point 2	4.45	1.39	1.05

Table D.4. The absorption coefficients used in the numerical model. They are calculated from the reverberation time measurements of two typical test cells.

Frequency	Absorption Coefficient
63	0.10
80	0.11
100	0.13
125	0.22
160	0.20
200	0.26
250	0.33
315	0.30
400	0.36
500	0.36
630	0.30
800	0.25
1000	0.31
1250	0.31
1600	0.33
2000	0.31
2500	0.32
3150	0.29
4000	0.29

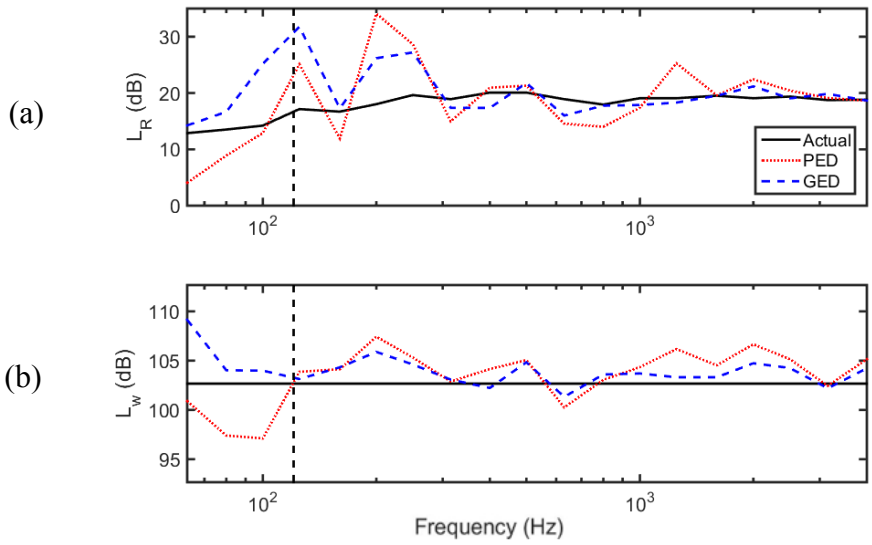

Fig. D.6. Results for the reference directivity source. The (a) logarithmic room constant and (b) the sound power level of the reference source as measurement by the two-point method in the simulated test cell. The vertical dashed lines represent the Schroeder frequency of the room.

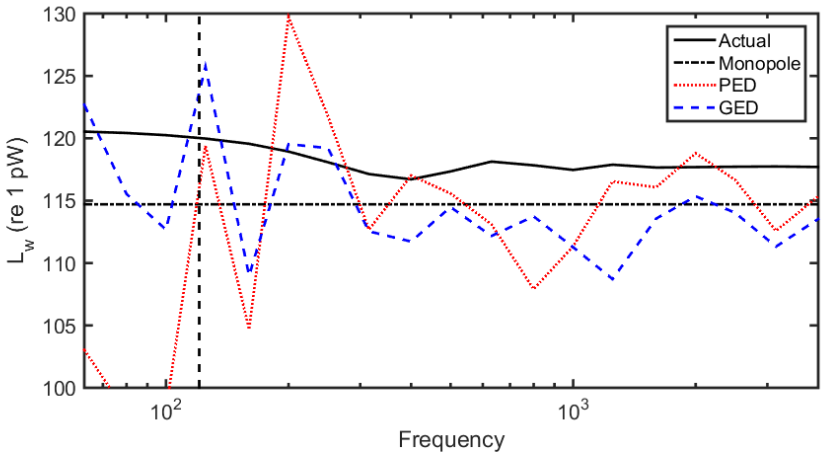

Fig. D.7. The sound power level of the simulated distributed source (two monopoles) compared to the actual (solid) and that of a monopole with the same source strength as each of the two monopoles in the pair (dashed-dotted). The vertical dashed line represents the Schroeder frequency in the room.

D.4 Discussion

There are a few reasons for the apparent sound power errors. The Hopkins-Stryker equation relies on several assumptions discussed in Sec. 2. One issue could be the size of the engine and its distributed nature. Another could be the lack of diffuse field at the measurement positions.

Because the engine is such a large source at least one of the two-point measurement positions was not in the direct geometric or acoustic far field. ISO 3745 suggests that the direct far field is at least twice the characteristic dimension of the source.[5] For this engine, that would be about 1.8 meters away. Although we have built in a near-field correction for a source with spherical spreading that attempts to correct for the amplitude of the GED, the near-field behavior of a larger source is more complicated than that of a monopole and needs to be accounted for. The large errors shown in the sound power measurements in Fig. D.6 are also likely due to this behavior.

Another source of error could be that the measurement positions were based on a rough geometric center. Although this was relatively simple to find, the true acoustic center is much more difficult to locate and is frequency dependent. This discrepancy could influence the results of the two-point method strongly.

Yet another issue could be the amount of absorption in the room. From numerical and experimental results shown in Chs. 3 and 4 of this thesis, the largest errors are seen in rooms with high amounts of damping due to the diffuse field assumption not being well met in more damped rooms. This test cell was more heavily damped than most of the rooms tested for this thesis, so one might expect greater errors. The diffuse field assumption was also influenced by the obstructive objects in the room and where they were located relative to the measurement positions. In this case, the lack of diffusivity likely exacerbated the distributed-source problems discussed previously.

From a practical standpoint, the amount of background noise and turbulence present in the test cell became an issue. This made both the measurement of the room constant and the sound power level difficult. For the measurement of the room constant, the reference directivity source was not powerful enough to overcome some of the background noise at lower frequencies. For engine sound power level measurements, the difficulty came from the turbulence produced by the ventilation system in the room. The strength of the turbulence was position dependent with some of the effects seen in Fig. D.4. The sound power level for the measurement with a position at 1 meter increases greatly at low frequencies due to this problem. A wind screen for the energy density probe might have helped with this issue.

Another possible source of error was that the reference directivity source measurements were taken before the engine measurements. Once the engine was turned on, the ventilation

system also turned on and the background noise due to the ventilation system was louder than the reference directivity source. As a result, the two points for the engine measurement were not in the exact same position as for the reference directivity source measurements. Based on previous experience, making both the two-point measurement for the reference source and the DUT at the same positions has not been crucial, but it can lead to small errors. Figure D.4 shows results from two different sets of measurement positions. Although both seem to converge at higher frequencies, the set with a point at 0.5 m from the engine is less erratic at low frequencies than that with a point at 1 m, which is near the average critical distance for the room.

A method of checking for errors within measurements would have been to measure the sound power of the reference directivity source using the ISO 3747 method, and to measure the sound power of the B&K reference source using the two-point method. This would have been able to show discrepancies, if any, between the two methods for more controlled sources in the test cell.

D.5 Conclusion

The two-point method was unable to match the ISO 3747 sound power level measurement in the industrial test cell for the internal combustion engine. It seemed to underestimate the sound power by about 5 or 6 dB. It is believed that the issue has more to do with the size and nature of the engine source than the room. The two-point method measured the total sound power level of the reference directivity source in the room to within 0.6 dBA of those measured using ISO 3741 and ISO 3745 and the 1/3 octave band curves matched well. The ISO 3747 method could have been validated by measuring the sound power of the reference directivity source with the method.

Future research could investigate the effects of large, distributed sources, with some theoretical corrections or usage guidelines to improve the two-point method. A more robust reference directivity source that can overcome high levels of background noise and a wind screen for the energy density probe would also yield improvements.